Design, Integration, and Deployment of UAS borne HF/VHF Depth Sounding Radar and Antenna System

By

Ali Mahmood

Submitted to the graduate degree program in Electrical Engineering & Computer Science and the Graduate Faculty of the University of Kansas School of Engineering in partial fulfillment of the requirements for the degree of Master of Science.

Chair: Dr. Carl Leuschen

Co-Chair: Dr. Fernando Rodriguez-Morales

Dr. Chris Allen

Date Defended: May 23, 2017

The thesis committee for Ali Mahmood
certifies that this is the approved version of the following thesis:

Design, Integration, and Deployment of UAS borne HF/VHF Depth Sounding Radar and Antenna System

Chair: Dr. Carl Leuschen

Co-Chair: Dr. Fernando Rodriguez-Morales

Date Defended: May 23, 2017

ABSTRACT

The dynamic thinning of fast-flowing glaciers is so poorly understood that its potential impact on sea level rise remains unpredictable. Therefore, there is a dire need to predict the behavior of these ice bodies by understanding their bed topography and basal conditions, particularly near their grounding lines (the limit between grounded ice and floating ice). The ability to detect previous VHF radar returns in some key glacier regions is limited by strong clutter caused by severe ice surface roughness, volume scatter, and increased attenuation induced by water inclusions and debris.

The work completed in the context of this thesis encompasses the design, integration, and field testing of a new compact light-weight radar and antenna system suitable for low-frequency operation onboard Uninhabited Aerial Systems (UASs). Specifically, this thesis presents the development of two tapered dipole antennas compatible with a 4-meter wingspan UAS. The bow-tie shaped antenna resonates at 35 MHz, and the meandering and resistively loaded element radiates at 14 MHz. Also discussed are the methods and tools used to achieve the necessary bandwidth while mitigating the electromagnetic coupling between the antennas and on-board avionics in a fully populated UAS. The influence of EM coupling on the 14 MHz antenna was nominal due to relatively longer wavelength. However, its input impedance had to be modified by resistive loading in order to avoid high power reflections back to the transmitter. The antenna bandwidths were further enhanced by employing impedance matching networks that resulted in 17.3% and 7.1% bandwidths at 35 MHz and 14 MHz, respectively.

Finally, a compact 4 lbs. system was validated during the 2013-2014 Antarctic deployment, which led to echo sounding of more challenging temperate ice in the Arctic Circle. The thesis provides results obtained from data collected during a field test campaign over the Russell glacier

in Greenland compared with previous data obtained with a VHF depth sounder system operated onboard a manned aircraft.

ACKNOWLEDGEMENTS

First of all, I want to thank my late parents for their incredible upbringing that instilled in me resilience, dedication, and confidence. Although they did not live long enough to see me achieve my major milestones but I owe all my success and accomplishments to them. Then, I would like to thank my lovely wife, Eman, for her tremendous support and patience though out my stay in graduate school. I also want to thank my sister, Dr. Iram Mahmood, my brother, Lt. Col. Faisal Mahmood, and my uncle, Dr. M.Y. Siraj, for their moral support and professional guidance that always kept me on the right track.

I would like to thank my M.S. advisor, Dr. Carlton Leuschen, for giving me the opportunity to work on such an amazing project. His permissive leadership style allowed me to think independently and also gave me a considerable degree of autonomy in successfully carrying out my tasks. I greatly appreciate Dr. Fernando Rodriguez-Morales for always encouraging me and for his exceptionally positive attitude especially under the most unfavorable circumstances.

This project would have not been successful without Dr. Richard Hale, as he played an instrumental role in proactively facilitating the interdisciplinary aspects of this project in a timely fashion, whenever needed. I would like to thank Dr. Shawn Keshmiri for looking out for us and keeping the team focused during the deployment. A special thanks to Dr. John Paden for his tremendous amount of support in the field and afterwards.

I appreciate Dr. Stephen Yan's initial mentorship, as he taught me various antenna related tools and techniques that helped me in finishing my project. I would like to thank Dr. Prasad Gogineni for his guidance. His passion for remote sensing inspired me to pursue a career in microwave engineering and radar technology.

Last but not the least, I want to thank Jennifer Laverentz, Bryan Townley, Paulette Place, Aaron Paden and fellow CReSIS students especially Akhilesh, Daniel and Jonathan for making my stay at CReSIS a joyful experience.

TABLE OF CONTENTS

1 INTRODUCTION 1

1.1 MOTIVATION 1

1.2 FREQUENCY SELECTION 1

1.3 PLATFORM SELECTION 2

1.4 PREVIOUS WORK 2

1.5 THIS WORK 4

1.6 THESIS OUTLINE 5

2 BACKGROUND 7

2.1 ANTENNA BASICS 7

2.1.1 Half Wavelength Dipole Antenna 7

2.1.2 Antenna Parameters 8

2.1.3 Mutual Coupling 11

2.1.4 Mutual Impedance 14

2.2 RADAR SYSTEM OVERVIEW 16

2.2.1 Receiver Sensitivity and Loopback Test 20

2.3 UAS SYSTEM OVERVIEW 28

3 ANTENNA DESIGN and INTEGRATION CHALLENGES 30

3.1 ANTENNA DESIGN REQUIREMENTS 30

3.1.1 Constraints Driven by the Sensor 30

3.1.2 Constraints Driven by the Platform 31

3.2 FEASIBILITY STUDY 32

3.3 ANTENNA SYSTEM INTEGRATION CHALLENGES 41

3.3.1 Unpopulated UAS: Mutual Coupling between HF and VHF Antennas 41

3.3.1.1 Antenna Configuration A *42*

3.3.1.2 Antenna Configuration B *47*

3.3.2 Populated UAS: Effects of Avionics on Antenna System 52

3.3.2.1 Populated UAS Configuration 1 ..... *52*

3.3.2.2 Populated UAS Configuration 2 ..... *54*

4 IMPEDANCE MATCHING NETWORK and EMI MANAGEMENT 65

4.1 IMPEDANCE MATCHING NETWORK 65

4.1.1 Co-simulation of 35 MHz Impedance Matching Network 65

4.1.2 Impedance Matching Network for 14 MHz antenna 69

4.2 ELECTROMAGNETIC INTERFERENCE (EMI) MANAGEMENT 73

4.2.1 EMI Characterization and Mitigation of UAS's Power Supply 74

4.2.1.1 Tests Setup for RFI Measurements *74*

4.2.2 EMI Measurements and Mitigation of Servo Wires 79

5 FIELD EXPERIMENT 87

5.1 FLIGHT LINES and SAMPLE RESULTS 89

6 FUTURE WORK 95

6.1 UAS AUTOPILOT 95

6.2 WEIGHT REDUCTION 95

6.3 ELECTROMAGNETIC COMPATIBILITY 96

6.4 MUTUAL COUPLING 96

6.5 ANTENNA SYSTEM 96

7 BIBLIOGRAPHY 98

8 APPENDIX A: LOOP BACK TEST MATLAB SCRIPT 101

LIST OF FIGURES

Figure 2-1: Charge distribution on a simple λ/2 dipole antenna 7

Figure 2-2: Geometry of a typical Yagi-Uda antenna 12

Figure 2-3: High level system block diagram of the radar system 16

Figure 2-4: Physical dimensions of the radar box 19

Figure 2-5: Setup for loopback test 23

Figure 2-6: Hanning windowed 35 MHz RF pulse captured by a digital oscilloscope 24

Figure 2-7: Uncompressed 35MHz return from loopback test 25

Figure 2-8: Measured Impulse Response of 35 MHz channel 26

Figure 2-9: Half power width of 35 MHz channel 26

Figure 2-10: Measured Impulse Response of 14 MHz channel 27

Figure 2-11: Half power width of 14 MHz channel 27

Figure 3-1: Dimensions of stock 40% Yak 54 UAS 31

Figure 3-2: 35 MHz antenna placement 34

Figure 3-3: 14 MHz antenna placement 34

Figure 3-4: S11 of 35 MHz antenna in free space 35

Figure 3-5: S11 of 14 MHz antenna in free space 36

Figure 3-6: Input impedance of HF antenna in free-space 37

Figure 3-7: Total antenna efficiency 38

Figure 3-8: Real part of input impedance with and without resistive loading 38

Figure 3-9: S11 of 14 MHz antenna with and without resistive loading 39

Figure 3-10: Measured vs simulated results of 35 MHz antenna 40

Figure 3-11: Antenna configuration A 42

Figure 3-12: S11 of HF antenna for configuration A 43

Figure 3-13: S11 of VHF antenna for configuration A 44

Figure 3-14: Input impedance of VHF antenna for configuration A 45

Figure 3-15: Directivity of VHF antenna for configuration A 45

Figure 3-16: Gain of VHF antenna in E-plane ($\varphi = 90^0$) for configuration A 46

Figure 3-17: Gain in nadir for antenna configuration A 47

Figure 3-18: Antenna configuration B 48

Figure 3-19: Directivity of VHF antenna for configuration B 48

Figure 3-20: Gain of VHF antenna in E-plane ($\varphi = 90^0$) for configuration B 49

Figure 3-21: Gain in nadir for antenna configuration B 50

Figure 3-22: Input impedance of VHF antenna for configuration B 51

Figure 3-23: S11 of VHF antenna for configuration B 52

Figure 3-24: Populated UAS configuration 1 53

Figure 3-25: S11 comparison between unpopulated and populated UAS 54

Figure 3-26: Populated UAS configuration 2 55

Figure 3-27: Real input impedance comparison between populated UAS configuration 1 and 2 56

Figure 3-28: S11 comparison between populated UAS configuration 1 and 2 57

Figure 3-29: Gain at nadir for 35 MHz antenna 58

Figure 3-30: S11 of 14 MHz antenna 59

Figure 3-31: Gain at Nadir for 14 MHz antenna 60

Figure 3-32: Integrated VHF antenna before Monokoting the wings 61

Figure 3-33: Integrated HF antenna's 16 AWG wires exposed during flight 61

Figure 3-34: Measured vs Simulated S11 of 14 MHz antenna after integration 62

Figure 3-35: Measured vs Simulated S11 of 35 MHz antenna after integration 63

Figure 3-36: 35 MHz antenna performance at each integration stage 64

Figure 4-1: Co-simulation Setup 66

Figure 4-2: Matching network board for VHF antenna 67

Figure 4-3: Comparison Ideal VS Realized response after co-simulation VS Measured 68

Figure 4-4: VHF Matching Network's Insertion Loss Comparison 69

Figure 4-5: Matching network board for HF antenna 70

Figure 4-6: S11 of HF antenna with and without matching network 70

Figure 4-7: HF Matching Network's Insertion Loss Comparison 71

Figure 4-9: HF Matching Network detuned to match the measured response 72

Figure 4-10: Test setup for EMI measurements 74

Figure 4-11: SREG 500U power supply EMI measurement results 75

Figure 4-12: SREG 550U vs SynQor based power supply in HF band 77

Figure 4-13: SREG 550U vs SynQor based power supply in VHF band 78

Figure 4-14: Cable shielding configuration for DUT 1 80

Figure 4-15: Measured RFI for HiTec HS-7940th servos based on DUT 1 80

Figure 4-16: Cable shielding configuration for DUT 2 81

Figure 4-17: Measured RFI for Volz DA 22-06-2605 servos based on DUT 2 82

Figure 4-18: Cable shielding configuration for DUT 3 83

Figure 4-19: Measured RFI for DUT3 84

Figure 5-1: Ariel photo of Campsite and Runway 88

Figure 5-2: Geographic Information of flight lines 88

Figure 5-3: Comparison between MCORDs and HF sounder data over "good lines" 91

Figure 5-4: Comparison between MCORDs and HF sounder data over "medium lines" 92

Figure 5-5: Comparison between MCORDs and HF sounder data over "bad lines" 93

LIST OF TABLES

Table 2-1: HF Sounder Radar Specifications 20

Table 2-2: Cascaded Noise Figure and Gain of each Receiver Component 21

Table 4-1: G1X's RFI Characterization Test Matrix 73

Table 4-2: Comparison between Volz and HiTec servos 85

Table 5-1: Operating Parameters for MCORDS and HF Sounder [24] 94

1 INTRODUCTION

1.1 MOTIVATION

The thinning of the Greenland and Antarctic ice sheets, along with terrestrial glaciers, have the potential to raise global sea level by several meters. Studies have shown, they have been melting at an alarming speed for the last decade, about twice the rate of the past several decades [2] [3]. A combination of observations derived from a range of geodetic techniques in Shepherd et al. [4] estimated that between 1992 and 2011, the Antarctic and Greenland ice sheets lost 1350 ± 1010 and 2700 ± 930 Gt of ice, respectively. This equates to an increase in the global mean sea level of 11.2 ± 3.8 mm. If the upper bound of global sea level rise predicted by IPCC is correct, low land island countries like Maldives (which is only about 2-4 meters above sea) may completely sink before the end of this century. The dynamic thinning of most fast-flowing glaciers containing significant amount of ice reservoirs into the ocean is so poorly understood that it's potential contribution to sea level rise remains unpredictable [1].

Radar sounding of ice in fast-flowing glaciers and around ice-sheet margins poses major challenges such as surface clutter and volume scattering. These issues are present due to rough surfaces and composition, attenuation, and backscattering from the ice profile and they become more prominent as the frequency of operations increases.

1.2 FREQUENCY SELECTION

As noted by Smith and Evans [5] , the most serious effect of scatterers is not the attenuation of the signal, but rather masking of the bottom return by the diffuse return from a multitude of scatterers. The attenuation problem can be attacked by increasing transmitter power and receiver sensitivity but the scatter-return issue can only be solved by radiating at lower frequency bands

[5]. The Rayleigh-scattering theory further explains that scattering losses can be decreased significantly if the wavelength of radar's operating frequency is greater than the scatterers [6]. Therefore, the operating frequencies in HF and VHF bands were selected to reduce propagation loss through temperate ice, which also helps in improving the signal-to-noise ratio (SNR).

The successful sounding of temperate ice in Patagonia at 30 MHz, as reported by Blindow (ICGPR, 2012), led to the selection of 35 MHz. To utilize the greater penetration power of HF band 14 MHz was selected to fill the gaps where the VHF band fails due to high volume scattering.

1.3 PLATFORM SELECTION

The tradeoff of operating at lower frequencies is that as the frequency decreases the antenna size increases making it difficult to implement a physical antenna array on an aerial platform. Therefore, it becomes necessary to synthesize a large 2D aperture in both the along-track and cross-track directions, as proposed by Dr. Prasad Gogineni (private conversations and meetings). Synthetic aperture in the along-track direction leads to finer resolution; the across-track synthesizes an array, which results in more gain and greater SNR. In order to achieve 2-D synthetic aperture, the radar needs to be flown along adjacent lines with $\lambda/2$ spacing of respective frequencies to create a 2D sampling grid.

Such flight missions require high maneuverability that can easily be achieved by a small UAS platform like the 40% YAK-54, rather than a large manned aircraft. Moreover, deploying an unmanned platform in Polar Regions is not only cost effective but it also reduces human factor.

1.4 PREVIOUS WORK

The selection of operating frequencies to address these issues became more obvious by analyzing previous attempts made by various depth sounding radar systems.

The Multi-channel Coherent Radar Depth Sounder (MCoRDS) with an operating bandwidth of 150- 210 MHz is designed, developed and deployed by the Center for Remote Sensing of Ice Sheets (CReSIS) at University of Kansas as part of NASA Operation IceBridge (OIB) program. It has been used extensively to survey the entire region surrounding North Pole and has been instrumental in producing ice-thickness map of Greenland [7][9].

The full capability of the system has been utilize in collecting data around the northern and southern west coast of Greenland where narrow fast flowing outlet glaciers were previously not surveyed. The collected data significantly improved coverage in these regions. However, substantial gaps exist, particularly at the coastline and along deep channels occupied by outlet glaciers. These gaps are attributed to high volume scattering and surface roughness due to depth sounder's operating frequency. Therefore, the only limiting factor of such a highly sensitive radar system is its operating frequency.

Warm Ice Sounding Explorer (WISE), is an airborne sounder designed to measure the nadir ice thickness of warmer glaciers. It was designed by NASA's Jet Propulsion Lab (JPL) in an attempt to operate in HF band. The antenna design was based on the Mars Advanced Radar for Subsurface and Ionosphere Sounding (MARSIS) antenna, which enabled scientists to discover layered water-ice deposits near Mars poles. Antenna with a center frequency of 2.5 MHz and 2 MHz of bandwidth is a monopole with the aircraft being its ground plane and the pole floating freely in the air. In this system the discrepancies in GPS location and lack of snow/firm correction resulted in inaccurate measurement of ice thickness. Besides WISE's complex design, costly field operation, and risky antenna integration solution, the data relies heavily on lengthy crossover analysis such as comparison to a mass-conservation approach. These attributes contribute to this

system's inefficiency to obtain credible data and lower its effectiveness in fully utilizing the favorable characteristics of HF band in temperate ice [7].

Blindow's work showed that the lower parts of Nef and Colonia glaciers were investigated using the 30 MHz airborne mono-pulse baseband radar BGR-P30. This system was capable of penetrating up to 800 meters of temperate ice as demonstrated in northern Patagonian ice field [8].

Surveying with a bulking antenna hanging 20 meters off a Euro-copter AS350 B3 helicopter poses flight safety concerns. Besides that the accuracy of GPS is questionable due to complex antenna design and integration solution. However, quality data was produced at the expense of less precise GPS locations, making it a less sustainable solution. A new, cost-effective, lower frequency and highly sensitive depth sounder solution is needed to address the issues mentioned above.

1.5 THIS WORK

The primary aspect of this work was the development of a dual-frequency (14 MHz and 35 MHz) antenna system compatible with a UAS with 4 meter wing span. In this application, the design and performance of the antenna system relies heavily on how it is integrated into the platform. The limited available real estate posed major integration challenges such as electromagnetic interaction between radiating elements, nearby avionics systems. These challenges were addressed by systematically dividing the integration process into several stages. Full-wave EM simulation, characterization and optimization of the antennas were completed at each stage to ensure minimal impact on the aerodynamic performance of the vehicle. Results from this effort are presented and discussed.

The second aspect of this work was the documentation of the radar system design and its performance. Relevant design considerations, such as calibration and mitigation of avionics-induced radio frequency interference, are described. Finally, this thesis document provides a summary of sample results obtained from data collected during a field test campaign over Russell glacier in Greenland. The results are compared with data obtained with a VHF depth sounder system previously operated onboard manned aircraft.

1.6 THESIS OUTLINE

Chapter 2: Background

The overview and theoretical background of three major sub-systems of the sensor's hardware is explained in this chapter. This chapter will define key parameters for antenna design and theory to help explain integration challenges. An overview of the UAS and characterization of radar system is also included in this chapter.

Chapter 3: Antenna Design and Integration Challenges

This chapter describes the antenna design requirements and constraints driven by the UAS and radar system. Based on that, a feasibility study was conducted, followed by preliminary antenna designs and measurements. To finalize the optimal integration solution a thorough study of antenna performance at each stage of integration phase is discussed in order to reduce the effects of mutual coupling between antennas and on-board avionics.

Chapter 4: Matching Networks and Electromagnetic Interference (EMI) Management

Measured results are used to design impedance matching networks to enhance antennas' performance. The last part of this chapter discusses EMI issues and suggested solutions.

Chapter 5: Field Data and Conclusion

Field operation and processing of collected data are discussed in this chapter. A comparison between data from High Frequency (HF) Sounder and MCoRDS over same flight paths is presented to demonstrate the penetration efficiency at lower frequencies.

Chapter 6: Future Work

Recommendations to further improve the current system are proposed. Suggestions for future work comprises of improvements in all subsystems: antenna designs, radar system, and EMI reduction.

2 BACKGROUND

2.1 ANTENNA BASICS

Antennas are the eyes and ears of any radar system. In technical terms an antenna act as an impedance transformer, as it transmit and receive signals between 50Ω radar system and 377Ω free-space. This section covers a brief background of the dipole radiator, along with antenna terminology and relevant parameters used in this report.

2.1.1 Half Wavelength Dipole Antenna

As the name suggests the total length of a half wavelength (λ/2) dipole antenna is approximately equal to half of a wavelength at the frequency of operation. Structurally a simple half wavelength dipole consist of a pair of wires each λ/4 long and separated by 180^0 apex angle, as shown in Figure 2-1.

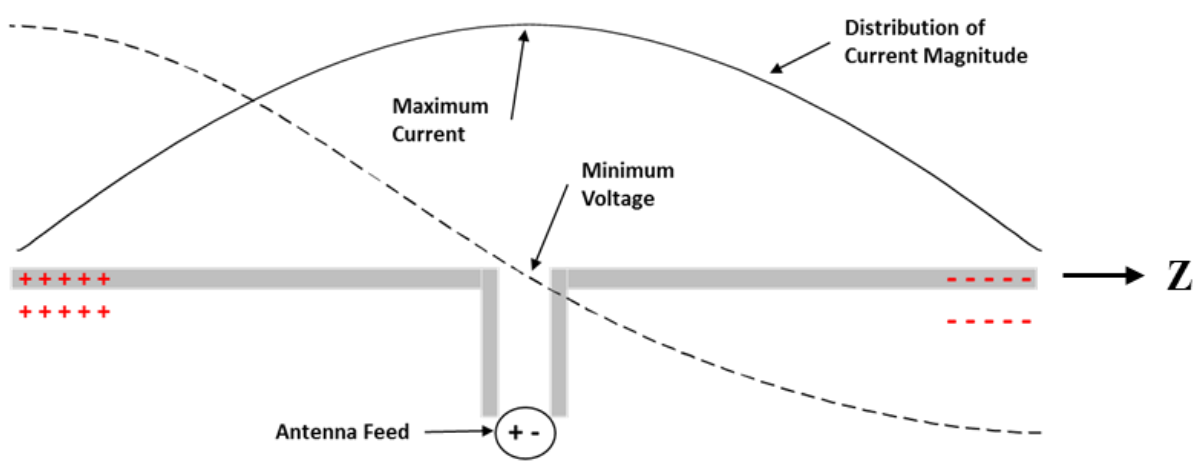

Figure 2-1: Charge distribution on a simple λ/2 dipole antenna

The orientation, feed, and dimensions of the conductors defines its input impedance and radiation pattern. Whenever a potential difference is applied across the input terminals opposite charge starts to accumulate on the tips of the legs causing current, I_e, to flow.

The buildup of opposite electric charge on both ends of the poles is where "Dipole" (the second part of the name) comes from. Voltage and current magnitude lines in Figure 2-1 explains that at the feed point, the current is maximum (I_m) whereas voltage is minimum. Current distribution along the length, l = λ/2 of dipole has sinusoidal form and is represented as [10]:

$$I_e(z) = I_m \sin\left|\beta\left(\frac{l}{2} - |z|\right)\right| \quad for \quad |z| < \frac{l}{2} \tag{2-1}$$

Practical dipole antennas have nonzero radius and finite feed gap spacing, which contribute to the non-ideal behavior of equation 2-1. Moreover, the EM fields generated due to current flow disturb the sinusoidal current distribution on an actual wire antenna. Since accurate current distribution is crucial in finding the dipole's input impedance and radiation characteristics. Therefore, a more reliable and convenient approach is to implement numerical computational tools such as the Integral Equation-Moment Method.

2.1.2 Antenna Parameters

Input impedance is one of the most fundamental and useful features of any standing wave antenna. Most antenna parameters can be quantified once their input impedance is known. The feed point connects the transmitter to the antenna and the ratio of voltage to current at that point defines the input impedance of the antenna. Mathematically, input impedance is expressed as [11].

$$Z_{in} = R_{in} + jX_{in} \ \ [\Omega] \tag{2-2}$$

Where,

Z_{in} = Impedance at input terminals of antenna

R_{in} = Antenna's input resistance.

X_{in} = Reactance at the input terminals of antenna

The "Real" part of input impedance is the sum of radiation resistance R_{in} and loss resistance R_L. The power radiated by the antenna is equal to the power absorbed by radiation resistance, loss resistance expresses the amount of power converted in to heat. Ideally, the power accepted by the antenna is radiated; however, since radiators with finite conductivity exhibit ohmic losses, a small portion of power is always converted in to heat. Amount of power accepted by the antenna depends on how well the impedances are matched. The quality of the impedance match between the transmitter and the antenna is represented by the reflection co-efficient as:

$$|\Gamma_{in}| = \frac{Z_{in} - Z_0}{Z_{in} + Z_0} \tag{2-3}$$

Another way of looking at it is to consider the antenna as a one-port device where S_{11} is the ratio of voltage reflected V^- to voltage incident V^+ on antenna's input terminal.

$$|\Gamma_{in}| = S_{11} = \frac{V^-}{V^+} \tag{2-4}$$

The value of impedance at the feed point describes how well the antenna input impedance Z_{in} is matched to the transmission line's characteristic impedance Z_o, which is generally:

$$Z_0 = 50 + j0 \quad [\Omega] \tag{2-5}$$

A good impedance match is achieved when the input reactance of the antenna is zero i.e. Z_{in} is purely resistive and close to 50 Ω or the characteristic impedance of the transmitter. Since the input impedance of a dipole is a function of frequency, a limited range of frequencies can be matched to the transmitter for efficient power transfers. The performance of resonant antennas over concerned frequencies is usually discussed in terms of return loss, which is the ratio of the reflected power to the incident power.

$$RL\ (dB) = -\ 20 * log_{10}\left(\frac{P^-}{P^+}\right) = -\ 20 * log_{10}(|\Gamma_{in}|) \tag{2-6}$$

The antenna's radiation resistance can be maximized by minimizing losses along the power transfer path from the generator to free space. This phenomenon is described as total antenna efficiency, which is a product of impedance mismatch loss and radiation efficiency.

$$e_a = M_L\ e_r \tag{2-7}$$

Where,

$$\text{Mismatch loss,} \qquad M_L = 1 - |\Gamma_{in}|^2 = \frac{P_{acc}}{P_{inc}} \tag{2-9}$$

Mismatch loss is the amount of power that is lost due to impedance mismatch.

$$\text{Radiation Efficiency,} \qquad e_r = \frac{P_{rad}}{P_{acc}} \tag{2-10}$$

Radiation efficiency describes how efficiently the power accepted by the antenna radiates. The total antenna efficiency can also be expressed in terms of power as.

$$e_a = \left(\frac{P_{acc}}{P_{inc}}\right)\left(\frac{P_{rad}}{P_{acc}}\right) = \frac{P_{rad}}{P_{inc}} \tag{2-11}$$

Where,

P_{inc} = Power Incident on the antenna through the power amplifier.

P_{acc} = Power accepted by the antenna after going through the feed point.

P_{rad} = Power radiated by the antenna.

The directivity of an antenna is equal to the ratio of its radiation intensity in a given direction over that of an isotropic source [11].

$$D(\theta,\varphi) = \frac{U(\theta,\varphi)}{U_o} = \frac{radiation\ intensity\ of the\ antenna}{radiation\ intensity\ of isotropic\ radiator} \tag{2-12}$$

Where, radiation intensity *U (θ φ)* is a description of how an antenna distributes energy across different directions in space whereas isotropic radiator is direction independent and radiates equally in all directions. A typical dipole antenna along the z-axis has an omnidirectional radiation pattern that radiates equally in all azimuth directions φ with maximum directivity at elevation angle, $\theta = 90^0$. Nulls occur at the tip of each pole i.e. only in the elevation plane specifically at $\theta = 0^0, 180^0$ for this particular orientation.

Antenna gain is essential the same as directivity, except that it accounts for antenna's ohmic losses. It is a product of radiation efficiency and directivity [11]:

$$G = e_r D \tag{2-13}$$

Absolute gain or peak realized gain takes in to account the total antenna efficiency. It can be expressed as:

$$G_r = M_L e_r D \tag{2-14}$$

2.1.3 Mutual Coupling

Two antennas in close proximity interact in a complicated manner causing changes in their currents' phases, magnitudes and distributions. This interaction is called mutual coupling. The

effects of mutual coupling between the antennas for the proposed configuration in the following sections can be explained by examining the principals involved in a Yagi-Uda antenna.

The Yagi-Uda antenna is one the most brilliant and simplest antenna designs that offer high gain and narrow bandwidth. Professor H. Yagi described the operation of this antenna in a classic paper published in Proceedings of Institute of Radio Engineers (IRE) in1926 [13]. The Yagi–Uda antenna generated interest to this day as a source of ideas for new types of antenna designs as useful lesson for today's antenna engineers. This antenna design is discussed to explain the impact of parasitic elements on antenna performance in the context of our application.

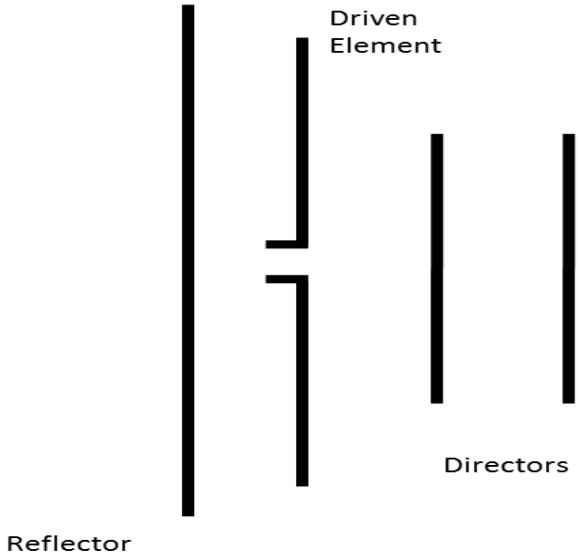

Figure 2-2: Geometry of a typical Yagi-Uda antenna

A typical Yagi-Uda antenna, as shown in Figure 2-2, consists of a driven element sandwiched between a set of non-driven parallel metallic structures/rods of unequal lengths. The length of each structure is defined by the resonant frequency of the driven element usually a simple half wavelength dipole or a folded dipole antenna [14]. The most interesting feature of Yagi antenna system is that it controls the radiation pattern and enhances the directivity and gain of a simple dipole antenna by utilizing the effects of mutual coupling between the excited and parasitic

elements. The current is excited due to the incident field from the driven element on to the parasitic element and converts it in to a radiator. This re-radiates the signal in a slightly different phase from the driven element, reinforcing the signal in some directions and cancelling it out in others. The phases of the current in the parasitic element depends upon the length and the distance between the elements. Parasitic elements in close proximity to the radiator are used either to reflect or to direct the radiated energy so that a compact directional system is obtained.

The reflector element is typically slightly longer than the resonant length of the feed element. The impedance of the reflector becomes inductive due to which the current excited on the reflector lags in phase from the driven element current. Similarly, the director element is shorter than resonant length, making it more capacitive and causing the current to lead in the phase.

The current on each element can be approximated by a finite series of odd-ordered even modes. Thus, the current on the nth element can be written as a Fourier series expansion of the form:

$$I_n(z') = \sum_{m=1}^{M} I_{nm} \cos\left[(2m-1)\frac{\pi z'}{l_n}\right] \tag{2-15}$$

Where I_{nm} represents the complex current coefficient of mode m on element n and I_n represents the corresponding length of the n element [11]. Therefore, the Yagi-Uda array may be regarded as a structure supporting a traveling wave whose performance is a function of current distribution on each element and the phase velocity of the traveling wave.

In a traditional Yagi-Uda design the lengths of directors, reflectors, and driven elements are based on the first resonance. However, higher resonances are available near lengths of λ, 3λ/2, and so forth but are seldom used [11].

2.1.4 Mutual Impedance

Mutual coupling between the antennas and nearby metallic objects can have considerable effects on antenna's input impedance. To elaborate the discussion in section 2.1.3, let's consider two closely spaced identical dipole antennas with only one antenna excited at a time. Radiation from the unexcited antenna # 2 due to incident electric fields alters the input impedance of antenna # 1. The resulting impedance depends not only on its own current but also on the currents of neighboring metals, referred to as driving-point impedance or active impedance. Such antenna configurations can be represented mathematically by two-port network. The relationship between currents and voltages is given by:

$$V_1 = Z_{11}I_1 + Z_{12}I_2 \tag{2-56}$$

$$V_2 = Z_{21}I_1 + Z_{22}I_2 \tag{2-17}$$

The above equations suggest that driving one antenna always induces the current on the other. When antenna #1 is excited ($I_1 \neq 0$) and antenna #2 is open circuited ($I_2 = 0$). Z_{11} is self-impedance of antenna #1 and Z_{21} is mutual-impedance at antenna #2 due to I_1.

$$Z_{11} = \left.\frac{V_1}{I_1}\right|_{I_2=0} \quad \& \quad Z_{21} = \left.\frac{V_2}{I_1}\right|_{I_2=0} \tag{2-18}$$

Similarly, when antenna #2 is excited ($I_2 \neq 0$) and antenna #1 is open circuited ($I_1 = 0$). Z_{22} is self-impedance of antenna #2 and Z_{12} is mutual-impedance at antenna #1 due to I_2.

$$Z_{22} = \left.\frac{V_2}{I_2}\right|_{I_1=0} \quad \& \quad Z_{12} = \left.\frac{V_1}{I_2}\right|_{I_1=0} \tag{2-19}$$

Equation 2-16 can be rewritten as the driving-point impedance of antenna #1

$$Z_{dp1} = Z_{11} + Z_{12}\left(\frac{I_2}{I_1}\right) \tag{2-20}$$

Similarly, equation 2-17 can be rewritten as the driving-point impedance of antenna #2

$$Z_{dp2} = Z_{22} + Z_{21}\left(\frac{I_1}{I_2}\right) \tag{2-21}$$

According to equations 2-20 and 2-21, the driving-point impedance is a function of current ratio of both antennas, their mutual impedance, and self-input impedance [11]. This explains the basic physics of the energy coupled from one antenna to the other and is useful in understanding the effects of coupling caused by any other nearby metallic obstruction. However, due to the complex boundary conditions of practical antenna environment it is best to use numerical tools for such analysis.

A major consequence of mutual couple is degradation of antenna's bandwidth. Depending on how the impedance is altered it can be rectified by implementing an impedance matching network that matches the antenna's input impedance to that of the transmitter over the required frequency sweep. Since the design of an impedance matching network dependents on driving point impedance, it becomes critical to characterize the effects of mutual coupling on the antenna's

impedance. However the extent and nature of the effects depends upon the antenna type, the dimensions of the metallic structure and the relative distance between them. Therefore, basing the impedance matching network design on measured driving point impedance is suggested.

2.2 RADAR SYSTEM OVERVIEW

The HF sounder radar box consist of three sections, as illustrated by high level system block diagram in Figure 2-3.

1. Digital section.
2. Radio Frequency (RF) section.
3. Power Management and Distribution section.

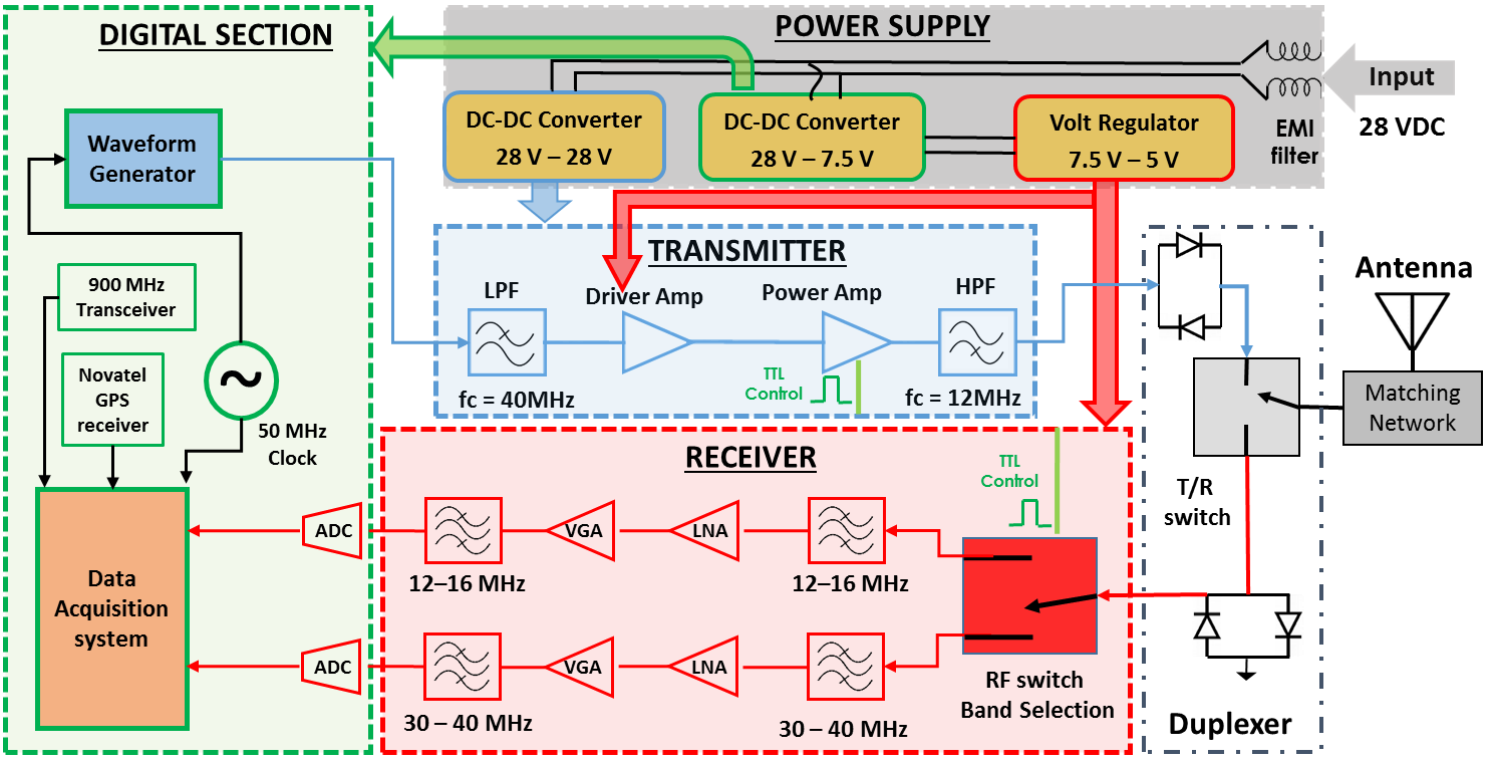

Figure 2-3: High level system block diagram of the radar system

The core of the system is the digital section, which is equipped with a field programmable gate array (FPGA) development kit and Analog-to-Digital/Digital-to-Analog (AD/DA) cards. The

on-board 50 MHz clock sequentially controls the entire radar operation from generating the waveform to properly synchronizing the power amplifier and storing the return signal. The FPGA firmware, developed in-house, allows the user to modify various radar parameters shown in Table 2-1, in the field using an RS-232 serial interface in Matlab. The radar box can also be configured to work as a vector network analyzer (VNA) for in-flight antenna characterization especially for 14 MHz antenna that can only be measured in-flight due to far-field requirements. Consequently, the frequency and envelope of the transmit waveform along with the pulse repetition frequency (PRF) can be modified based on antenna characteristics.

To ensure pulse amplification only during the transmit event, the negative logic 100 W pulsed power amplifier (PA) is driven by 3.3 V TTL signal provided by one of the I/O pins on the development kit. Another 3.3 V TTL signal from the FPGA is used to toggle a single pole double throw (SPDT) RF switch for receiver channel selection between the two frequency bands. In-flight radar status and quick look data can be remotely controlled and retrieved through a 900 MHz transceiver link interfaced with the FPGA development board via the RS-232 serial port of the on-board unit and with the PC on ground station.

The Novatel GPS receiver unit outputs 1 pulse per second (PPS) signal synchronized with Coordinated Universal Time (UTC) to timestamp the location of raw radar data recorded on the SD card. The raw GPS data is also stored in a separate microSD card. The accuracy of the GPS data is enhanced by implementing differential GPS post-processing method. This is done by using the raw data from a stationary second GPS receiver at the base station along with atmospheric data from nearby observatories. It precisely positions the base station and computes the errors for each measurement from the position of base station and subtracts from the GPS data of the UAS. The

resulting differential GPS solution greatly improves the positioning data corresponding to each radar record.

The Radio Frequency (RF) section is subdivided into a high power RF section and a low power RF section. In the low power RF section the transmit pulse out of the waveform generator is filtered and amplified by the driver amplifier before it reaches the final power amplifier stage. The high power RF section handles the rest of the transmit chain between the pulsed PA and antenna feed. In order to eliminate low-frequency transients from PA switching, the driver circuitry for the power amplifier is followed by a high pass filter, capable of handling power greater than maximum PA output. The RF signal is then delivered to the antenna feed or matching network through a duplexer circuit designed for transmit/receive (T/R) operations. The low power RF section in each receiver channel is a cascade of a low-noise amplifier with a variable-gain amplifier and an anti-aliasing filter. The received signal from the antenna is routed to the received side of the T/R switch and then through the selected frequency channel all the way to the A/D converter. Finally the raw data streams to the SD card.

The power supply section manages and distributes clean DC power to all sections of the radar box. In order to make the radar system less susceptible to conductive as well as radiated electromagnetic interference (EMI), the power supply is equipped with a well damped multi-stage differential-mode and common-mode passive EMI filter. The filter serves as an interface between the power source and multiple DC-DC converters and one voltage regulator. The main power source could either be the output of engine's alternator or batteries ranging from 16 to 40 Volts. The supply consists of two 28 V DC-DC converters: one to power up the PA and high power RF section and the other one is a spare which can also be used in series to deliver up to 56 V_{DC} to accommodate higher power amplifiers in future. The digital section and Novatel receiver board

runs on one 7.5 V DC-DC converter whereas 5 V voltage regulator powers up the low power RF section. The entire system draws about 1.10 A at 28 V when the PA is driven at its full capacity setting the maximum power consumption to 30.8 W. The entire radar system weights about 4 lbs. and fits in to an 8”x 6”x 5.5” chassis as shown in Figure 2-4.

Figure 2-4: Physical dimensions of the radar box

Radar System Parameters	Values
Operating Frequencies (HF/VHF)	14 MHz / 35 MHz
Bandwidth (HF/VHF)	0.7 – 1.1 MHz / 3.3 – 5.5 MHz
Range Resolution (HF/VHF) in Ice	173 - 110 meters / 37 - 22 meters
Peak Transmit Power	100 W (max.)
Power transmitted by antennas (HF/VHF)	33 W / 92 W
DC Power Consumption	30.8 W (max.)
Pulse Repetition Frequency	10 - 20 kHz (adjustable)
Pulse Duration	1 µs (adjustable)
Hardware Presumes	1023 (adjustable)
Sampling Rate	50 MSPS
Radar Box Dimensions (L x W x H)	8”x 6”x 5.5”
Radar Box Weight	4 lbs.

Table 2-1: HF Sounder Radar Specifications

2.2.1 Receiver Sensitivity and Loopback Test

The receiver SNR can be determined by evaluating the noise factor contribution of each RF stage from the input of the receiver all the way to the ADC. The total noise figure of the RF section of the receiver can be calculated as follows.

$$F_n = F_1 + \frac{F_1 - 1}{G_1} + \frac{F_2 - 1}{G_1 G_2} + \cdots + \frac{F_N - 1}{G_1 G_2 G_{N-1}} \tag{2-6}$$

F represents the noise factor and G represents the gain of corresponding RF stage. Table 2-2 includes the list of components in the receiver chain and their respective gains.

	Duplexer	Limiter	BPF	LNA/VGA
Noise Figure (dB)	0.20	0.50	0.50	2.50
Gain (dB)	-2.50	-0.50	-0.50	7.50

Table 2-2: Cascaded Noise Figure and Gain of each Receiver Component

Using the information in Table 2-2 and Eq. 2-20, the calculated internal noise figure of the receiver as it cascades down the chain turns out to be 3.94 dB for 35 MHz and 5.83 dB for 14 MHz. Along with the contribution of noise from the RF front end the antenna itself is a significant source of noise picked up by the antenna from the surrounding environment. Ionization and recombination phenomena in the ionosphere adds to the atmospheric noise which varies with frequency and is more pronounced in HF than VHF band. Atmospheric noise figure at 14 MHz and 35 MHz are 29dB and 19dB, respectively [15]. Thermal noise for a 50 Ω system is calculated as:

$$Thermal\ Noise = 10log_{10}(kT_o) = -174\frac{dBm}{Hz} \tag{2-21}$$

Where,

$T_o = 20^0C = 293\ K$

Boltzmann constant, $k = 1.38\ x\ 10^{-23}\frac{J}{K}$

Therefore,

$$\text{Normalized Thermal Noise at 14 MHz} = -173.93 + 29 = -144.93\ \frac{dBm}{Hz}$$

$$\text{Normalized Thermal Noise at 35 MHz} = -173.93 + 19 = -154.93\ \frac{dBm}{Hz}$$

The receiver noise floor is a sum of receiver noise figure, bandwidth and normalized thermal noise at each frequency as shown below.

$$Noise\ floor = Normalized\ Thermal\ Noise + 10log_{10}(BW) + F_n(\text{dB}) \qquad (2\text{-}22)$$

Using Eq. 2-24 and the measured bandwidth from previous section the noise floor at 14 MHz is -76.88 dBm and -86 dBm at 35MHz. Moreover, the quantization SNR depends on ADC's effective number of bits (ENOB). For ENOB = 11.5 bits with a maximum A/D level of 10 dBm ($2V_{pp}$), the quantization noise floor is give as [16]:

$$SNR_{ADC} = 10\ dBm - 6 * 11.5 = -59\ dBm \qquad (2\text{-}23)$$

Using Eq. 2-23 and 2-24, receiver sensitivity turns out to be 135 dBm at 14 MHz and 145 dBm at 35MHz. Additional SNR of 30 dB can be achieved with maximum coherent averaging (1023 pre-sums) before storing the raw data.

To verify these number a loopback test was conducted. The test setup shown in Figure 2-5 includes a 10 us delay line that was used to simulate the return time of the transmitted pulse based on air-ice interface and approximated altitude of the UAS. 110 dB attenuation was added between the transmitter and the receiver with 6 dB additional attenuation associated with the delay line.

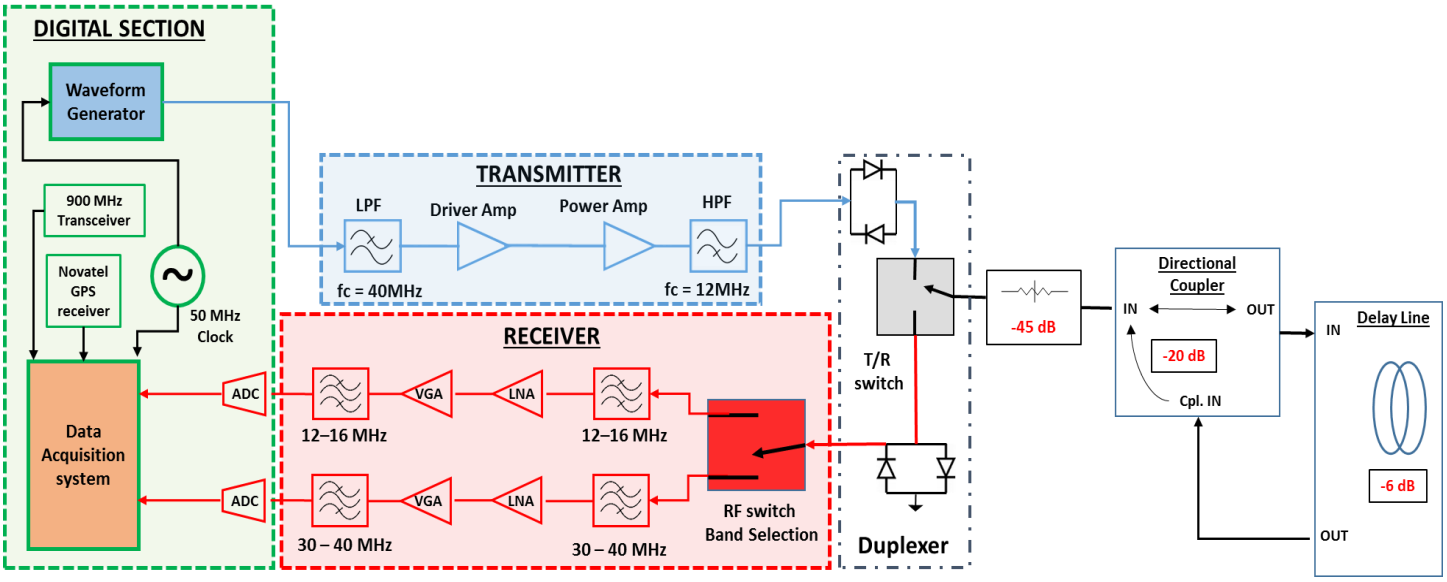

Figure 2-5: Setup for loopback test

Transmit pulses at both frequency bands are weighted by a Hanning window to achieve narrow main lobe, lower side-lobe level and higher side lobe roll-off rate. Figure 2-6 shows the Hanning windowed 35 MHz transmit waveform digitized by an oscilloscope after 10 dB attenuation. The side-lobe level performance of the HF sounder was analyzed as a part of loopback test at both frequencies.

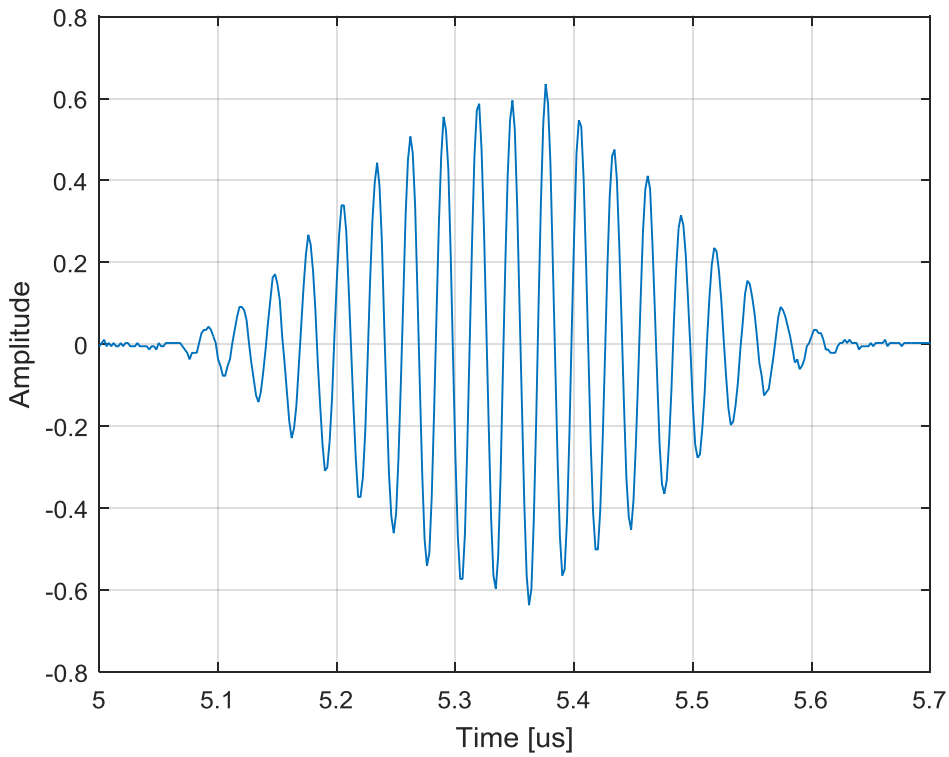

Figure 2-6: Hanning windowed 35 MHz RF pulse captured by a digital oscilloscope

The unprocessed return after the loop back test in Figure 2-7 shows the feed-through and the return signal stored in the SD card.

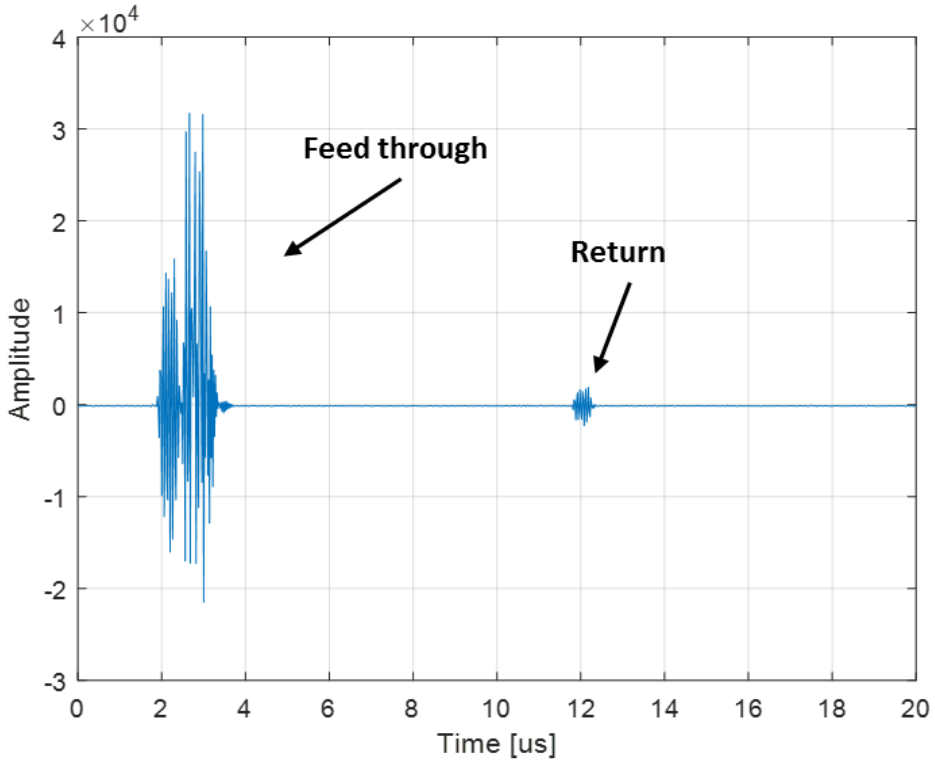

Figure 2-7: Uncompressed 35MHz return from loopback test

The measured response of the 35 MHz channel after pulse compression with a Hanning window is shown in Figure 2-8. As expected the side lobe levels are around 37 dB below the main lobe due to Hanning smoothing function. Signal-to-noise ratio (SNR) of 40 dB was achieved after 1023 coherent integrations. The loop sensitivity of this setup is the sum of SNR and total attenuation (116 dB) placed between the transmitter and receiver, which turns out to be 156 dB.

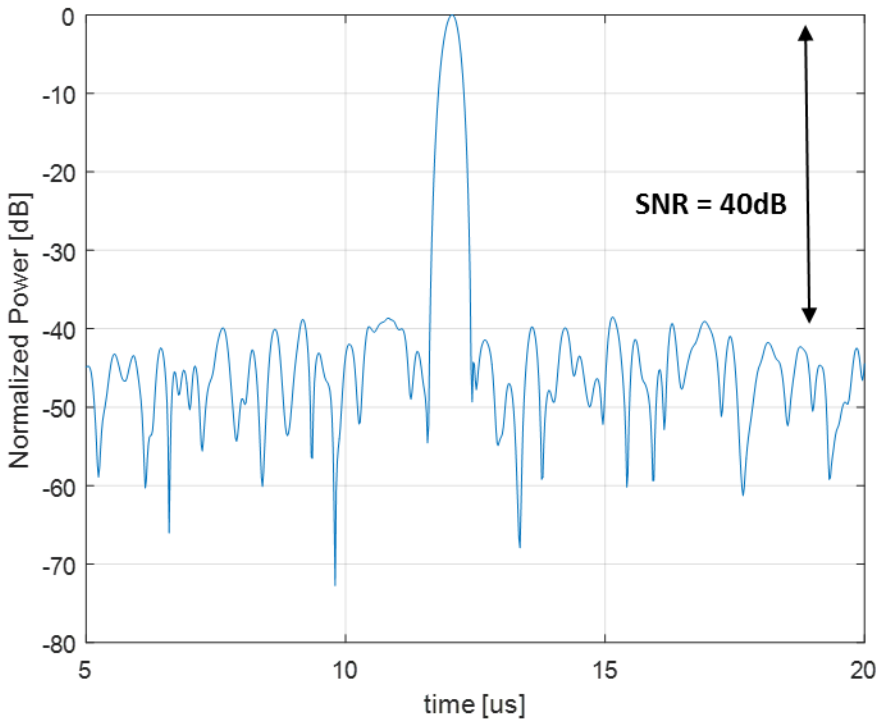

Figure 2-8: Measured Impulse Response of 35 MHz channel

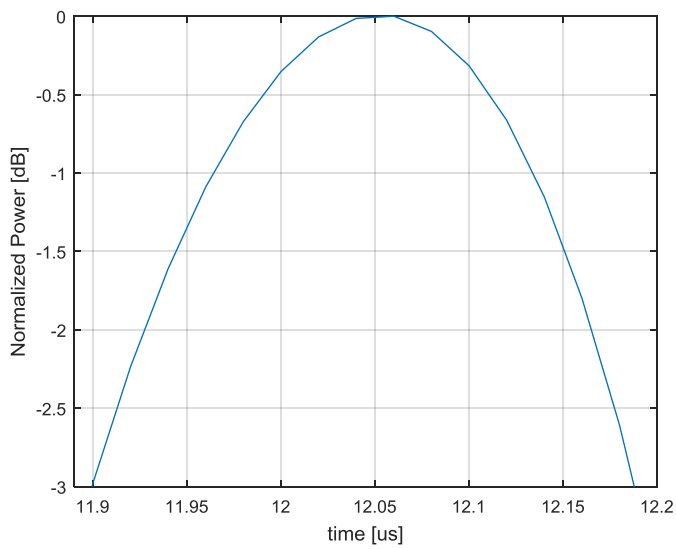

Figure 2-9: Half power width of 35 MHz channel

A zoomed view of the main peak at around -3dB in Figure 2-9 indicates a half power width of 0.28 us, which corresponds to approximately 42 meters of resolution in air.

Similarly, for the 14 MHz channel the receiver sensitivity is 156 dB with 40 dB SNR, as shown in Figure 2-10. However the half power width noted in Figure 2-11 is 0.82 us, reducing the resolution down to 123 meters in air.

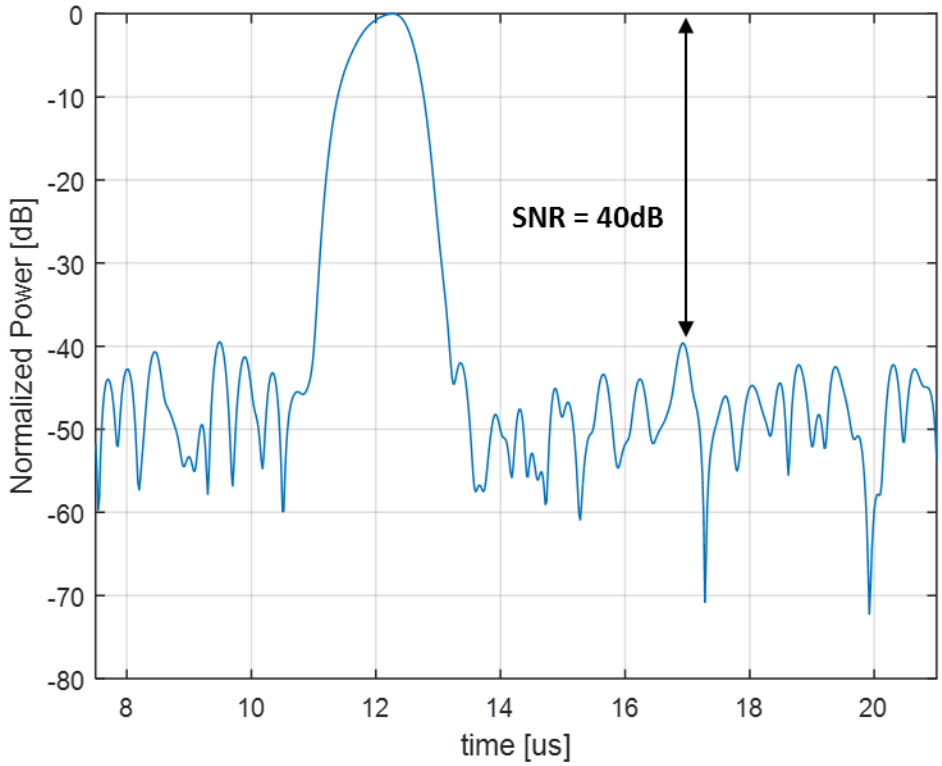

Figure 2-10: Measured Impulse Response of 14 MHz channel

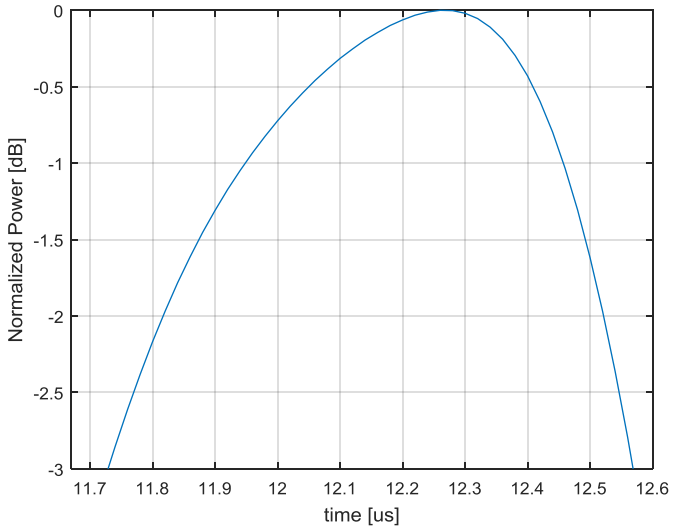

Figure 2-11: Half power width of 14 MHz channel

The anomalies in the measurements above such as squinted main lobe and asymmetric side-lobe levels are due to the non-ideal behaviors of delay line at our frequencies of interest [17].

Coarse resolution at HF band is attributed to the limitation on the physical size and volume of the 14 MHz antenna resulting in narrower bandwidth. The difference in bandwidths between HF and VHF channels is a trade-off between range resolution and penetration depth. HF antenna is capable of greater penetration but at the expense of narrower bandwidth. On the other hand the wider bandwidth of VHF can produce finer resolution but lack in penetration depth. Therefore, the radar operation at the HF band is intended to fill the gaps where the VHF system fails due to high volume scattering.

2.3 UAS SYSTEM OVERVIEW

The UAS used as a platform in this project is a 40% scaled version of Yak 54. The high maneuverability of this soviet aerobatic aircraft equipped with precise auto pilot system is ideal to fly closely spaced parallel lines to synthesize a large two dimensional (2D) synthetic.

The structure of the UAS consists of three major building materials. The inner skeleton and ribs are made out of light weight balsa wood. Ribs in the wing structure are covered by an aerodynamic thin layer of fiberglass skin. To reduce air drag and increase aircraft visibility especially in snow covered backdrop the surface of the fuselage and wings are coated with a multi-color smooth sheet of Monokote. Flight loads and the weight of the wings are carried by a high strength low weight carbon fiber spar developed by CReSIS's composite materials laboratory.

The UAS is capable of operating in two different modes. In radio-controlled mode the pilot has full control of the vehicle for takeoff and landing. Once the aircraft is airborne it can be switched to fully autonomous flight mode controlled by an on-board off the shelf autopilot unit

called We-pilot. A line-of-sight S-band communication link between the aircraft and ground station is used to switch between flight modes. It also provides vital flight information from the on-board sensors to the ground station, which is monitored by the flight engineer during the entire length of the mission. In case of emergencies, the UAS is equipped with Automated Flight Follower (AFF) that automatically tracks the location and velocity of the aircraft and transmits the data via satellite to a ground-based flight-monitoring system in near-real-time. The main power is delivered either from batteries or the engine's alternator to a power distribution box that powers up all on-boards avionics and actuators for control surfaces.

3 ANTENNA DESIGN and INTEGRATION CHALLENGES

3.1 ANTENNA DESIGN REQUIREMENTS

Antenna performance parameters are usually defined by the sensor's application but its physical design is primarily a function of constraints driven by the platform. The main focus of this chapter is to evaluate antenna performance in regards to the trade-offs associated with the integration challenges leading up to the final antenna configuration and integration solution.

3.1.1 Constraints Driven by the Sensor

The radar's operational bandwidth is an important parameter in determining its performance in resolving targets located at different ranges, known as range resolution. It is the measure of its ability to determine whether only one or more than one different targets are observed and is expressed as:

$$\rho = \frac{c}{2B \times \sqrt{\varepsilon_r}} \quad [meters] \tag{3-1}$$

Where,

Speed of light, $c = 3 \times 10^8$ m/s

Relative permittivity of solid ice, $\varepsilon_r = 3.15$

Radar bandwidth, $B = 1/\tau$

τ = Pulse duration

According to Eq. 3-1, the range resolution is inversely proportional to radar bandwidth therefore wider antenna bandwidth translates to finer resolution. However, range accuracy is related to both the range resolution and signal-to-noise ratio as:

$$\rho_r = \frac{\rho}{\sqrt{2\,SNR}} \qquad [meters] \tag{3-2}$$

Eq. 3-2 illustrates that higher SNR is desirable for better range measurement uncertainty. SNR can be improved by maximizing the power delivered to the antenna. Bandwidth is a range of frequencies over which critical performance parameters are acceptable. For this application 10 dB return loss is set as the benchmark for indicating radar's operational bandwidth that is to ensure that 90% of the available power is delivered to the antenna. As bandwidth depends on radiator's volume, limitation on its dimensions set by the platform still needs to be addressed [10].

3.1.2 Constraints Driven by the Platform

Successful integration of antennas onto UAS platforms pose many challenges especially antennas in HF and VHF bands. They claim major real estate on the limited UAS airframe, due to large wavelengths at low frequencies.

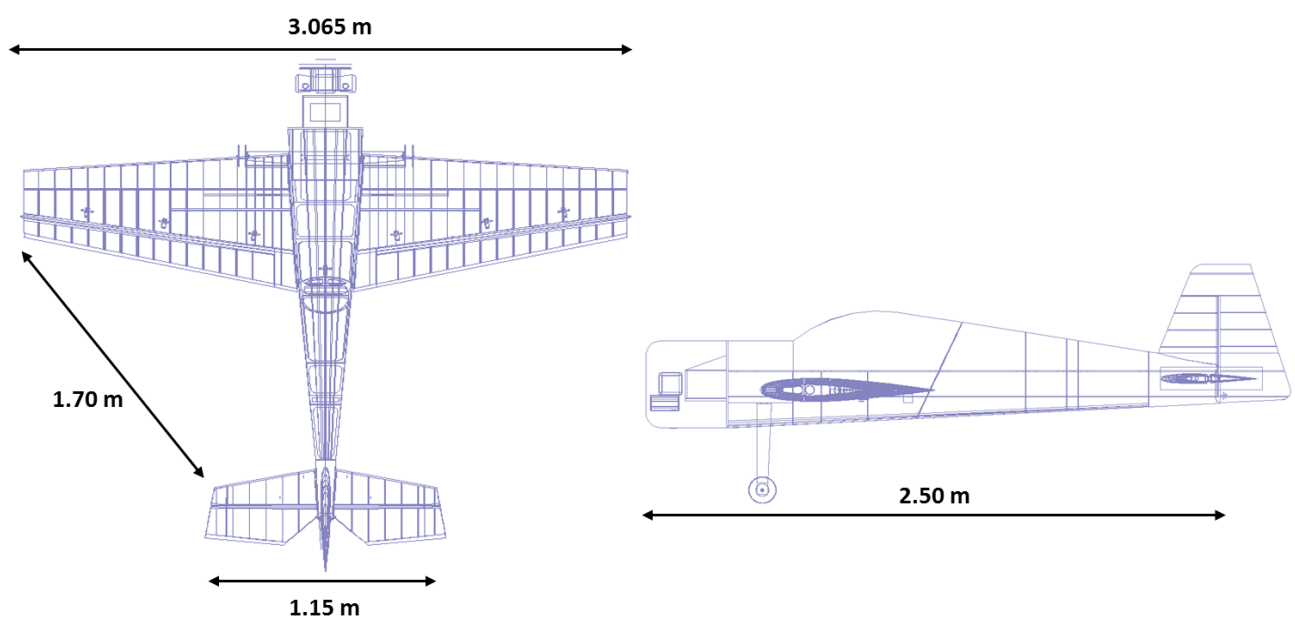

Figure 3-1: Dimensions of stock 40% Yak 54 UAS

The novelty of the proposed antenna design lies in taking a dipole antenna geometry as the starting point and developing it within the real estate available on a fully realizable UAS. As shown in Figure 3-1**,** the longest dimension of stocked 40% Yak 54 is the wingspan at only about 3.065 meters, which in terms of electrical length is approximately λ/7 at 14MHz and λ/3 at 35MHz according to:

$$\lambda = \frac{c_0}{f} \tag{3-3}$$

Where,

f = Antenna's natural resonance frequency.
λ = Wavelength.

Other limitations such as aerodynamic constraints and weight needs to be considered in order to achieve dual frequency antenna design. Therefore, the conformal antenna approach was set as a starting point, as they are key to not only optimally utilizing the UAS's real estate but also help in weight reduction as well as minimizing unnecessary air drag.

3.2 FEASIBILITY STUDY

Ansys's High Frequency Structure Simulator (HFSS) was used to conduct a feasibility study of various antenna designs. The following factors were evaluated in selecting and designing the most efficient antenna system:

- Aerodynamic constraints require antennas to be conformal to all aerodynamic surfaces.
- The UAS's structure and control surfaces dictates the available real estate for antennas.
- The UAS's endurance requires a light weight design.

The most notable designs that were considered during the feasibility study included monopole, patch and Landstofer antennas but they came short in meeting the requirements for both the radar system and the UAS. For example, monopole and patch antennas require a ground plane at least 1λ long, which is equal to seven times greater than the largest platform dimension and thus impossible to integrate. A dual frequency Landstofer design was a serious candidate but did not qualify due to poor performance at both frequency bands. Due to the high density of metallic structures inside the fuselage every location was considered even those that were avoided in the past due to aerodynamic constraints. Eventually, the decision was made in favor of a two antenna solution with each antenna dedicated to one frequency band. Wings were selected for the most suitable location to place bow-tie shaped dipole antenna for 35 MHz. For a partially folded and meandered HF dipole radiator the wings had to be extended to accommodate a major portion of the 14 MHz antenna that extend from the feed to the out-board edge of the wings. The remaining part of the dipole is a removable free floating 16 AWG wire that connects between the metallic structures on the wing edge and a tiny extension on the tail, as shown in Figure 3-3.

To ensure 180^0 out of phase current flow on each dipole leg the antennas were feed through baluns developed in-house using a twisted pair of magnetic wires wrapped around a ferrite core. One end of the twisted pair connects to the inner and outer conductors of the coax cable via SMA connector, and the other ends are soldered to each leg of the dipole. Figure 3-3 shows the feed for 14MHz antenna mounted on top of the cowling covering the engine, whereas feed for the other radiator sits on a wooden sheet inside the fuselage. The feed is reached through a small hole through the Monokote covering the fuselage, as shown in Figure 3-2.

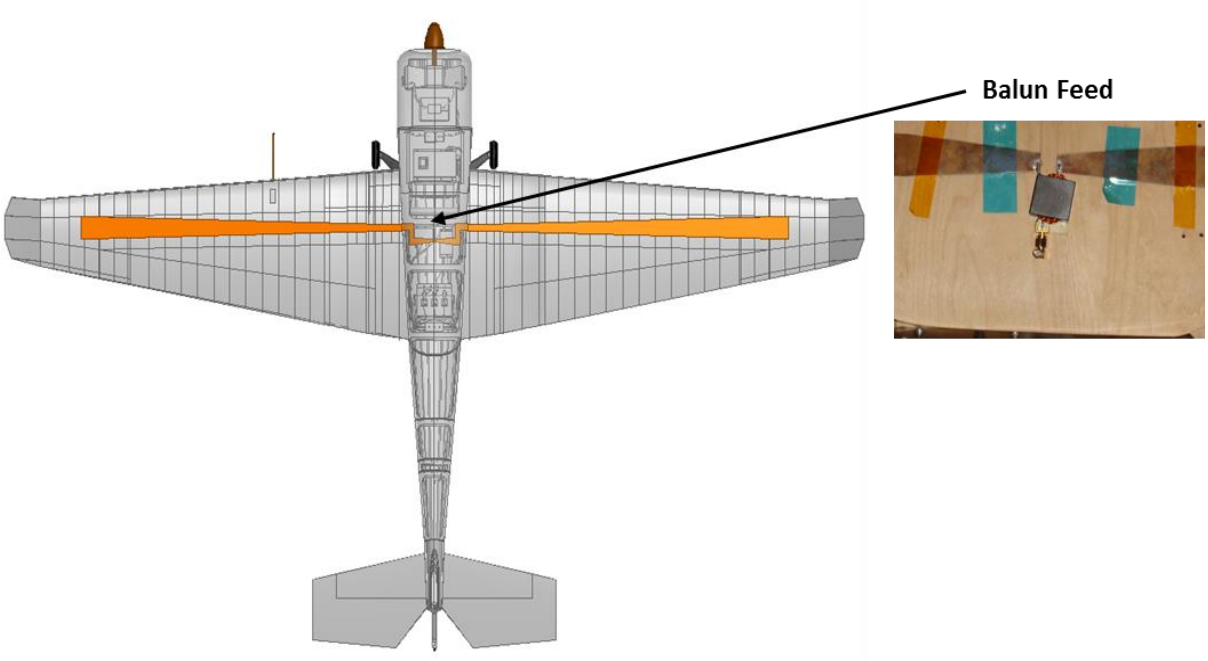

Figure 3-2: 35 MHz antenna placement

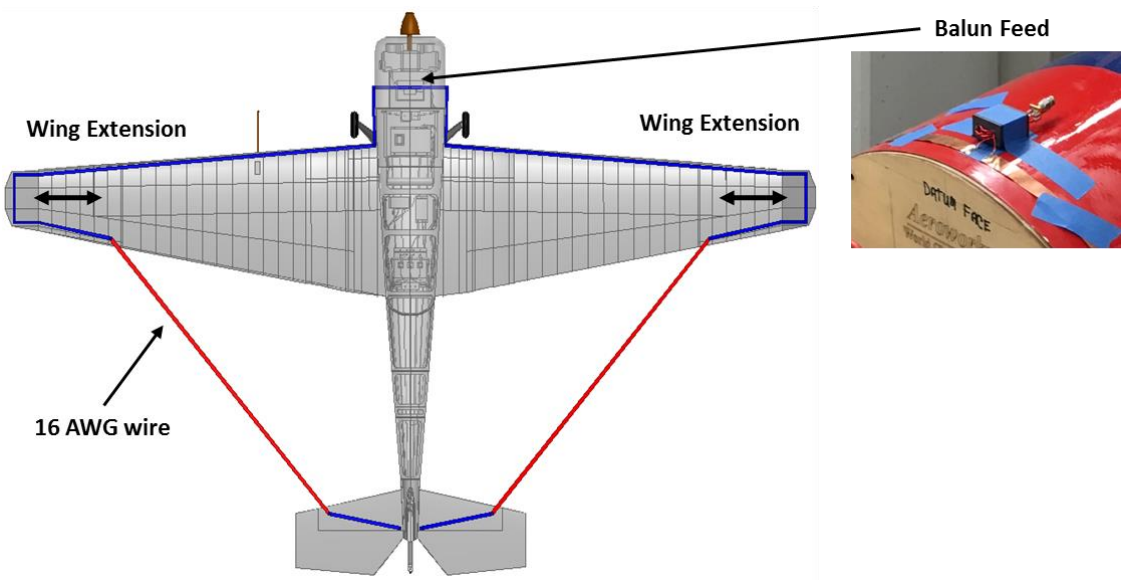

Figure 3-3: 14 MHz antenna placement

With the exception of 16 AWG wires of 14MHz dipole both antennas were fabricated entirely with thin copper tape making them conformal to the UAS structure. Their conformal structure allow them to be protected and hermetically sealed by a layer of Monokote.

After meeting aerospace constraints the antenna system was simulated to determine the performance of each element. In order to validate the basic geometry of the proposed antenna system the UAS was set as an electrically transparent empty shell in HFSS simulations. The simulated results of each dipole in free-space are shown below in Figure 3-4 and Figure 3-5**.**

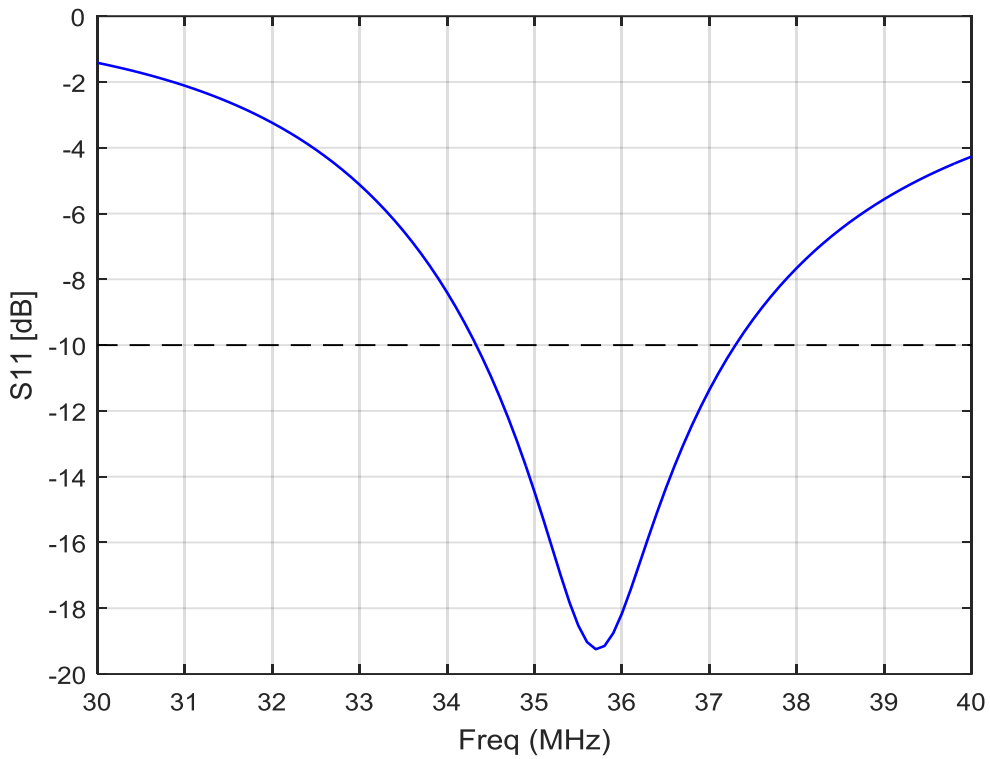

Figure 3-4: S11 of 35 MHz antenna in free space

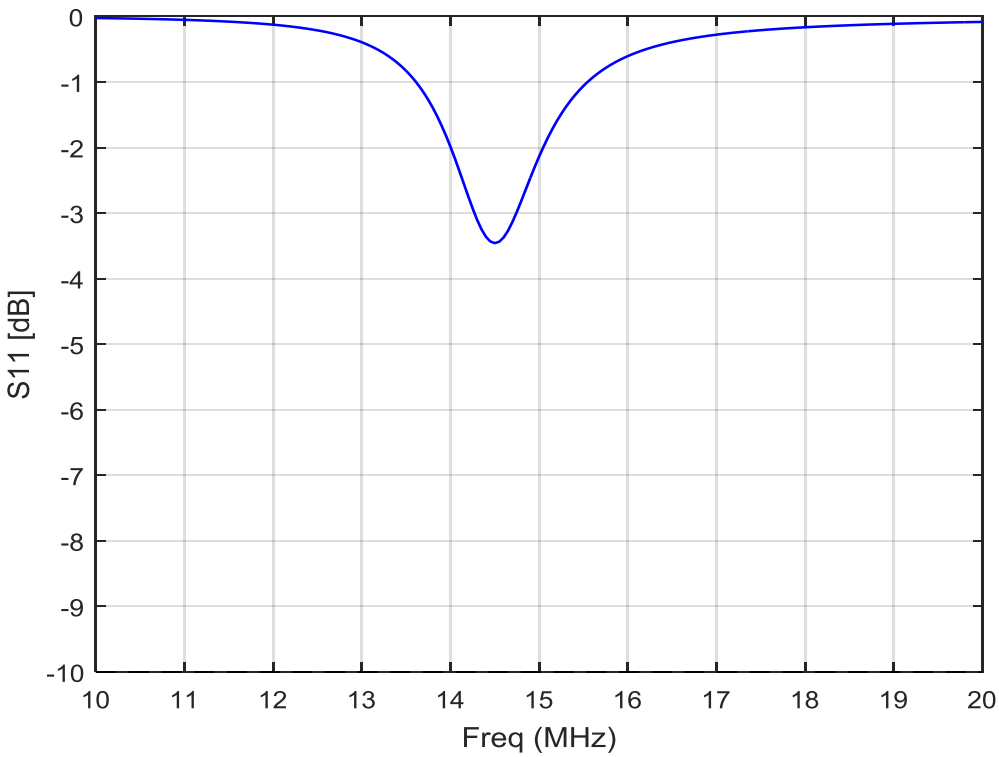

Figure 3-5: S11 of 14 MHz antenna in free space

As antenna volume increases more radiation modes are introduced on its structure, which leads to higher bandwidth [10]. It is noticeable in the case of bow-tie antenna, as results in Figure 3-4 indicate a bandwidth of approximately 3.25 MHz at -10 dB. On the other hand it is hard to define the bandwidth of 14 MHz antenna from results in Figure 3-5, which is attributed to sharp variations in the reactance component of input impedance around resonance frequency, as shown in Figure 3-6. The degradation in the input impedance is due to the meandered part of the dipole antenna, as it causes the current to cancel and introduce capacitance, which leads to lower bandwidth and efficiency.

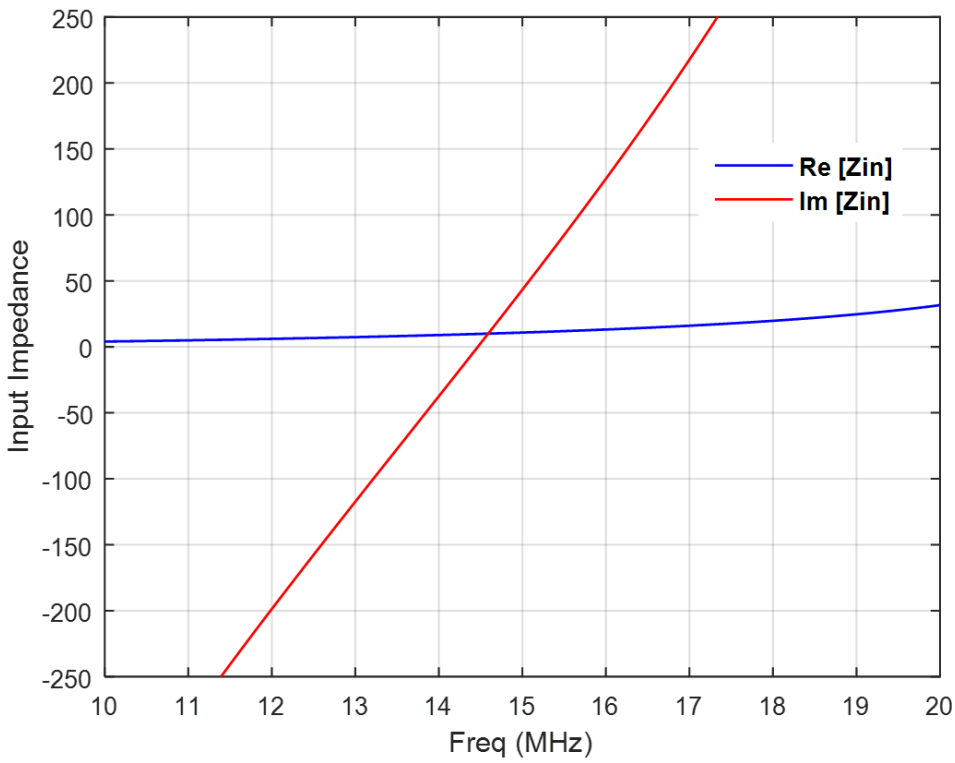

Figure 3-6: Input impedance of HF antenna in free-space

Generally, an impedance matching network between the transmitter and the antenna is used to increase the bandwidth but in this case the resistive part of the input impedance is too low, approximately 10Ω, to match it to 50Ω transmitter. One approach to increase the resistance is to load the antenna with resistors at the expanse of radiation efficiency. Comparison in Figure 3-7 indicates a 10% loss in total antenna efficiency by adding 10Ω resistor on each leg of the dipole. However, the improvement in the real part of impedance, shown in Figure 3-8, outweighs the efficiency loss.

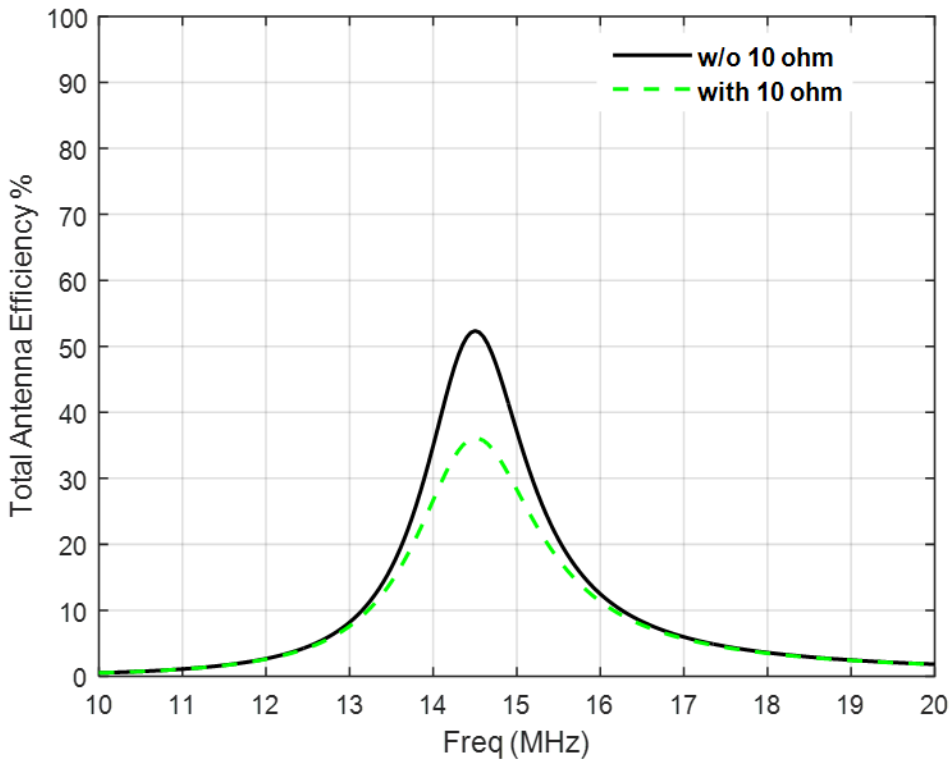

Figure 3-7: Total antenna efficiency

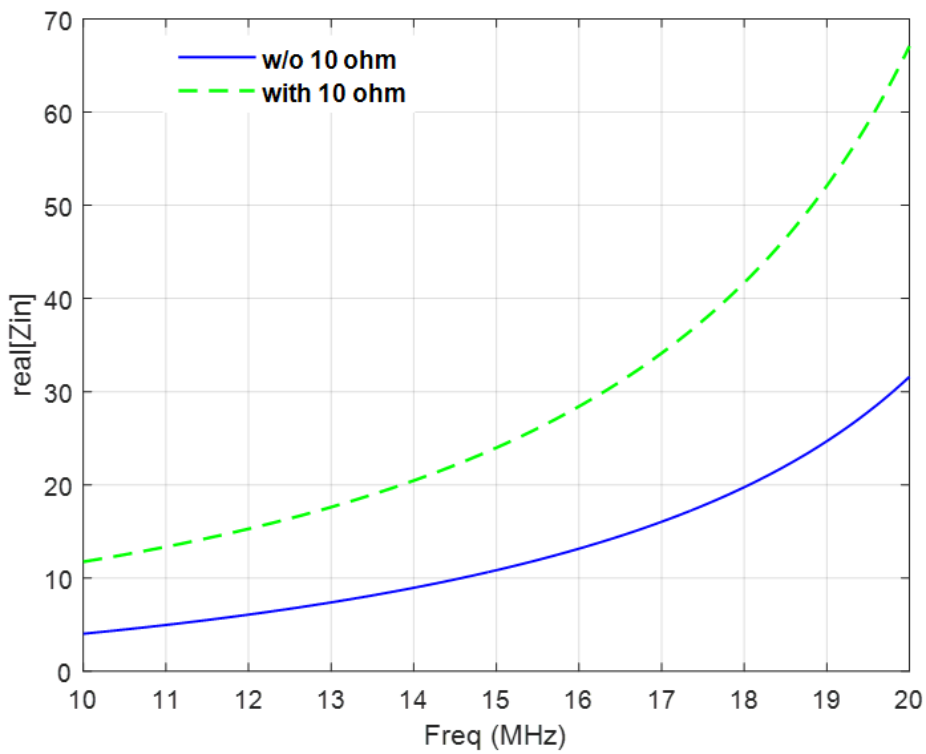

Figure 3-8: Real part of input impedance with and without resistive loading

The addition of resistors improves the return loss, as shown in Figure 3-9, by bringing the real part of input impedance closer to the 50Ω. It also prevents any potential damage to the power amplifier caused by high power reflections from the antenna due to impedance mismatch between the two.

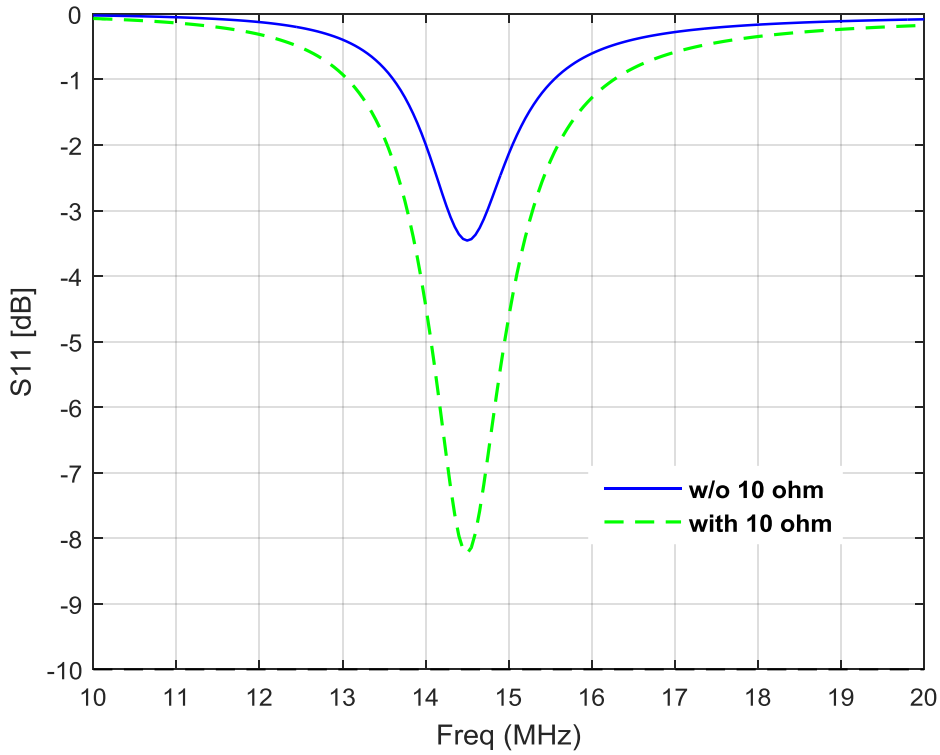

Figure 3-9: S11 of 14 MHz antenna with and without resistive loading

The frequency rating of the absorber in CReSIS's anechoic chamber and its inner dimensions do not meet the far field criteria at the HF band, but that is not the case at VHF band. In order to validate HFSS simulation results a bow-tie antenna was quickly fabricated and measured inside the chamber.

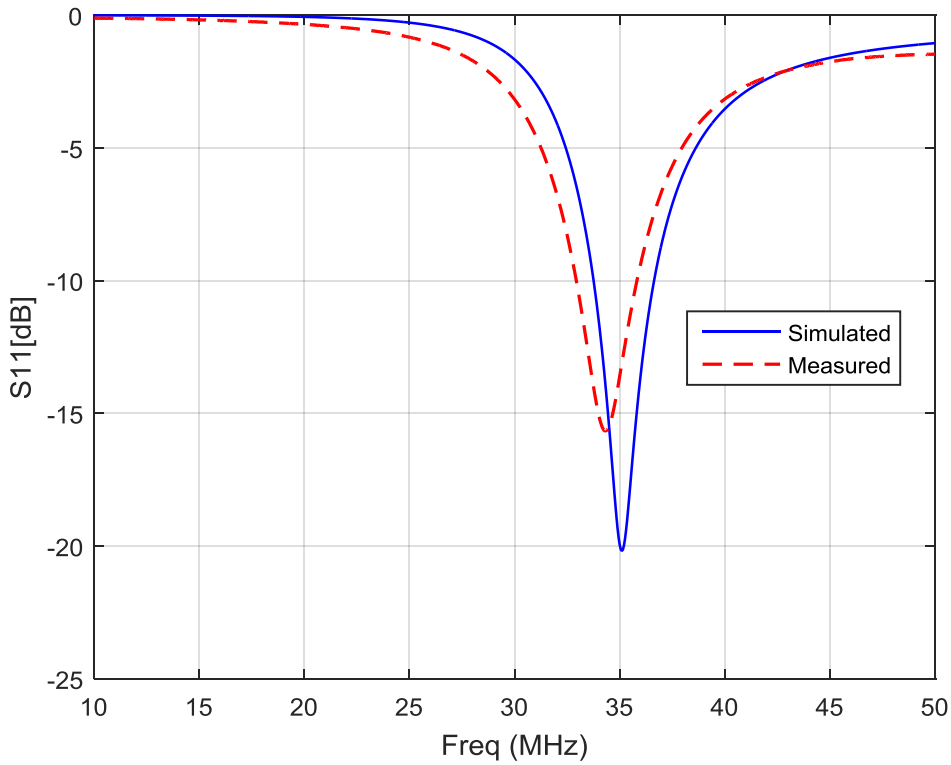

Figure 3-10: Measured vs simulated results of 35 MHz antenna

A slight frequency shift between the simulated and measured S11, as shown in Figure 3-10, is due to dielectric loading of Styrofoam used as a support structure under the antenna. The relative dielectric constant of Styrofoam at our frequency of interest is around 1.1 but since one side of the antenna is exposed to open air and the other side sits on the Styrofoam the effective permittivity ε_{eff} is calculated to be around 1.05 [19] [20]. Dielectric loading reduces the propagation speed of the wave, which increases the electrical length of the antenna of same physical dimension causing it to resonate at a lower frequency [20]. It can be calculated as:

$$f_m = \frac{f_0}{\sqrt{\varepsilon_{eff}}} = 34.26\ MHz$$

$$\lambda_m = \frac{\lambda_0}{\sqrt{\varepsilon_{eff}}} = 8.33\ meters \tag{3-4}$$

Where,

f_m = frequency after dielectric loading.

Frequency shift from 35.10 MHz down to 34.26 MHz calculated in Eq. 3-4 is consistent with the results in Figure 3-10. The accuracy of these results ensures the reliability of HFSS simulations, making it a very useful tool for antenna tuning and optimization especially for 14 MHz antenna that can only be measured during flight tests.

3.3 ANTENNA SYSTEM INTEGRATION CHALLENGES

Integration of multiple antennas on an airborne platform comes with many trade-offs and challenges. For example, vehicle's metallic features and adjacent antenna can impact the performance of the radiating element by reflecting or re-radiating energy. This section discusses the effects of mutual coupling on antenna performance at two major stages of integration. The first stage deals with the mutual coupling between the antennas on an unpopulated UAS and the second stage highlights the interaction between the antenna system and on-board avionics on a populated UAS.

3.3.1 Unpopulated UAS: Mutual Coupling between HF and VHF Antennas

It is best to investigate the interaction between the antennas before populating the UAS with avionics in order to address any mutual coupling effects within the antenna system. Since the radar system is design to operate at one frequency at a time, the HFSS simulations were set up in a way that each antenna was excited individually while terminating the other with 50 Ω. That way any "parasitic" effects due to the unexcited antenna could be monitored and mitigated. The first set of simulation were based on antenna configuration in Figure 3-11.

3.3.1.1 Antenna Configuration A

Simulation results in Figure 3-12 shows a slight shift in frequency from 14.45 MHz to 14.3 MHz. The shift is minor as the electrical length of 14 MHz antenna is relatively longer as compared to that of the parasitic antenna. By the same token the frequency shift is more pronounced in case of bow-tie antenna as noted in Figure 3-13.

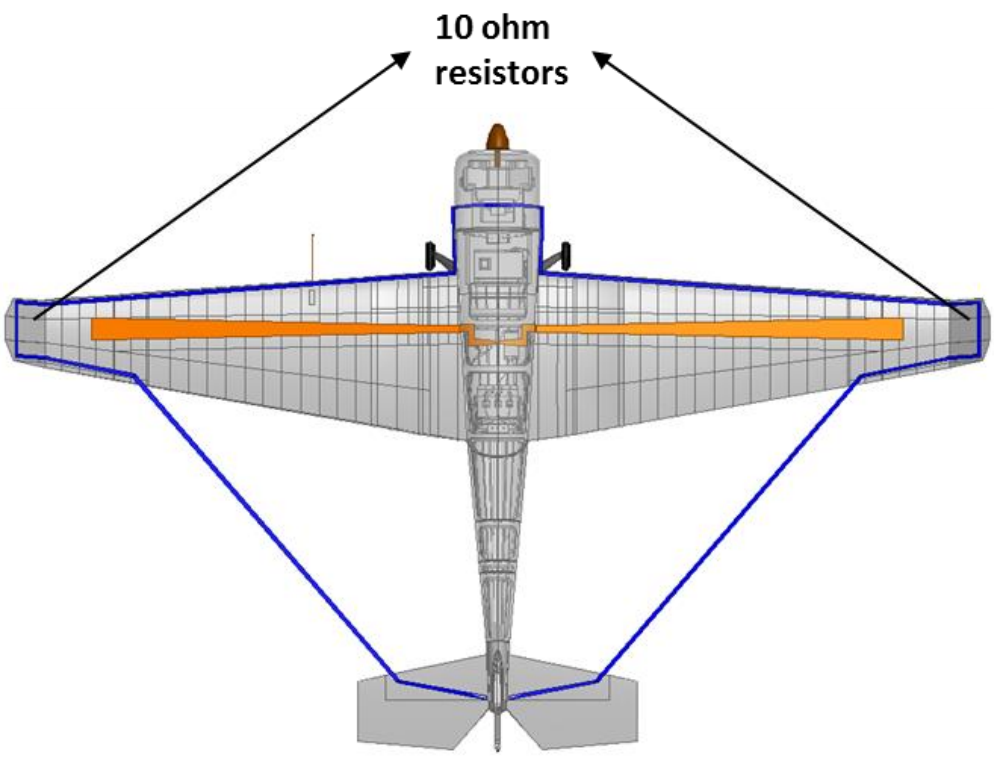

Figure 3-11: Antenna configuration A

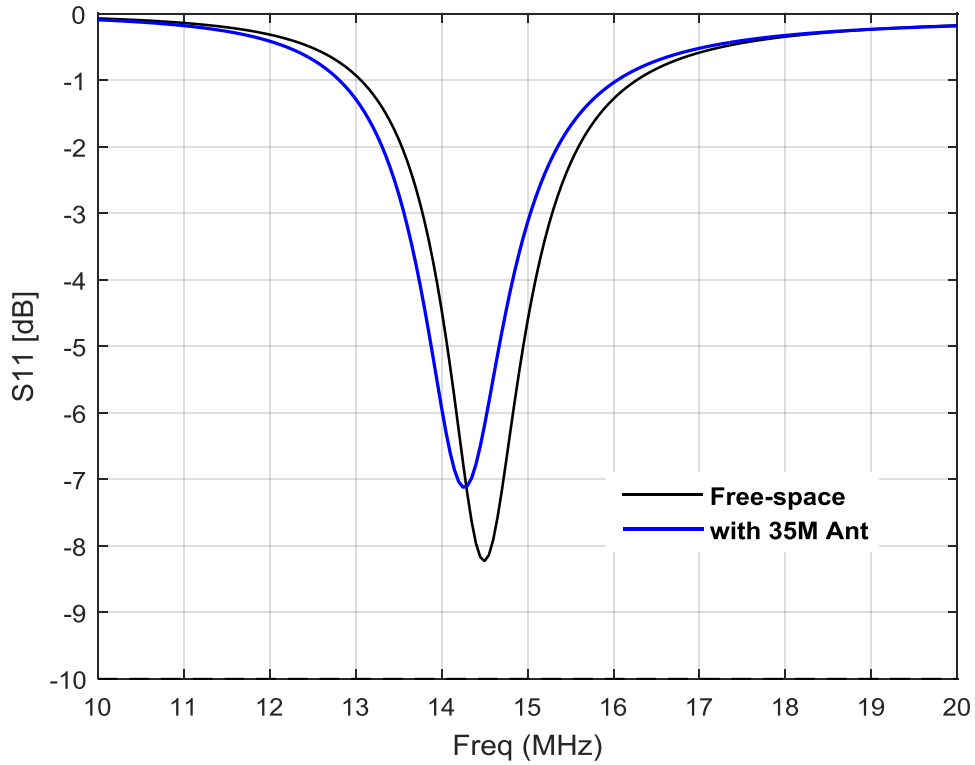

Figure 3-12: S11 of HF antenna for configuration A

The current induced by the radiating bow-tie antenna on to the terminated 14 MHz element cause it to re-radiate and alter the current distribution on the excited element. Consequently, the modified input impedance, in Figure 3-14, depends not only on the excitation current but also the current induced by the parasitic structure, as described by Eq. 2-15 and 2-16 in section 2.1.4.

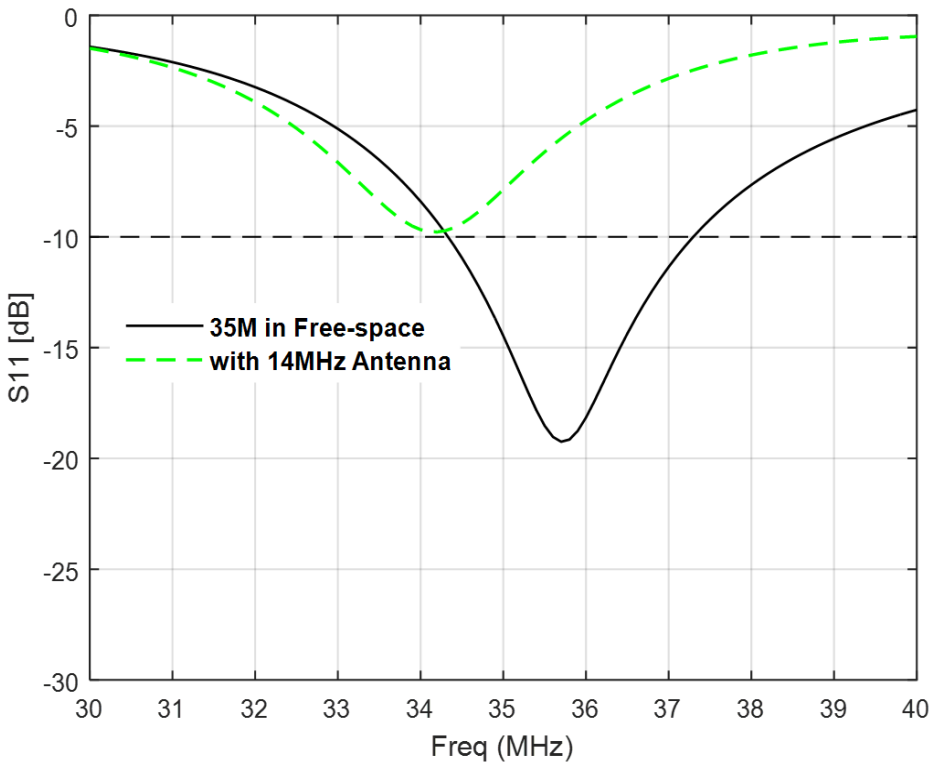

Figure 3-13: S11 of VHF antenna for configuration A

According to Eq. 2-3, reflection co-efficient is a function of antenna's input impedance Z_{in}, which means that deviation of Z_{in} from the characteristic impedance of the transmitter would result in impedance mismatch loss. As noted in Figure 3-14 the change in real part of Z_{in} from approximately 50Ω to 25Ω resulted in degradation in the reflection co-efficient from -18dB to -10dB.

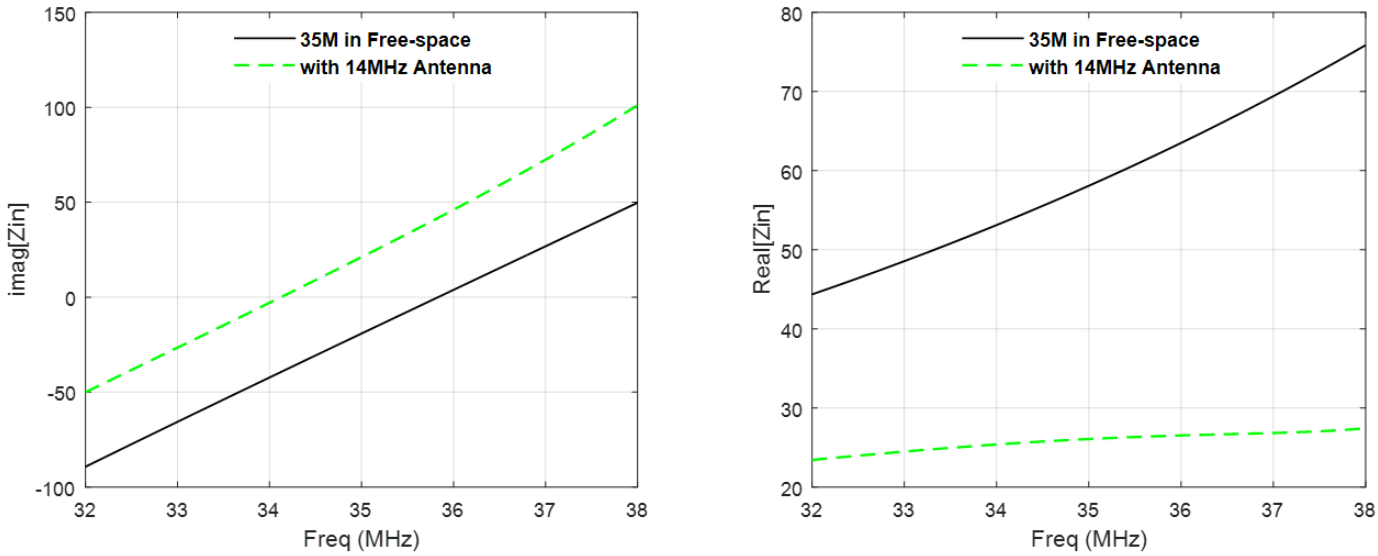

Figure 3-14: Input impedance of VHF antenna for configuration A

The shift in resonance frequency from 35.8 MHz to 34 MHz is due to the shift in the zero crossing of the reactive part of mutual impedance, which dominates the self-impedance of the antenna as noted in Figure 3-14. Moreover, the effects of mutual coupling are not limited to the antenna's input impedance but also the radiation pattern, which is clearly visible in Figure 3-15.

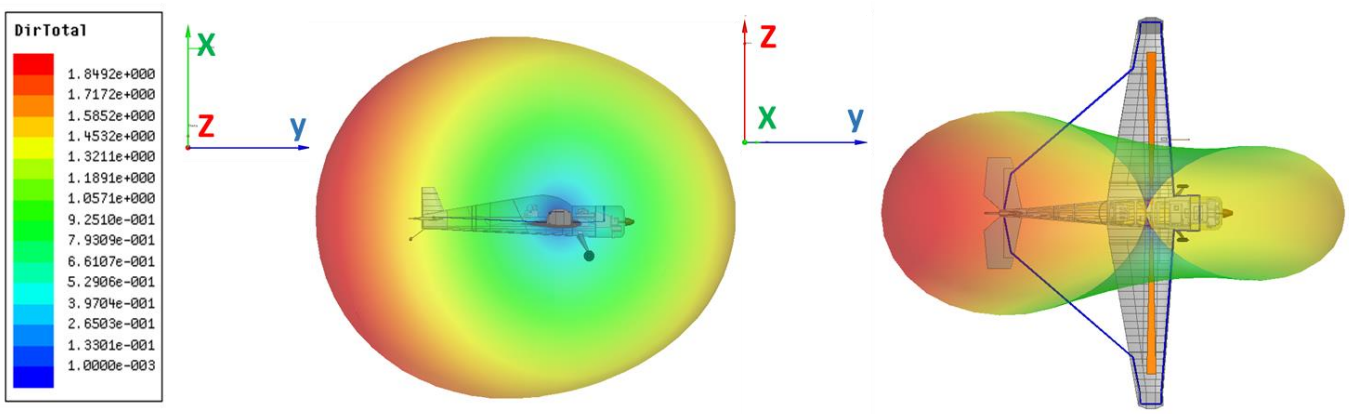

Figure 3-15: Directivity of VHF antenna for configuration A

In order to understand the squinted radiation pattern in Figure 3-15 it is important to evaluate the physical features of HF antenna in terms of electrical length of bow-tie antenna. As shown in Figure 3-11, the portion of 14 MHz antenna along the leading edges of the wings parallel

to the bow-tie antenna all the way to the 10Ω resistors on wing tips is approximately a little over one λ at 35 MHz. The remaining part after the resistors including a small porting on the trailing edges and 16 AWG wires is under one λ at 35 MHz. Based on the discussions in section 2.1.3, such a setup essentially constitutes a Yagi-Uda radiator. The electrically longer portion, the reflector, and shorter portion, the director, turns the antenna system in to a broadside array with increased directivity towards the tail of the aircraft. As noted in Figure 3-16, the front to back ratio of gain in E-plane is 1.178 dB higher than that of an ideal omnidirectional antenna, i.e. 0 dB.

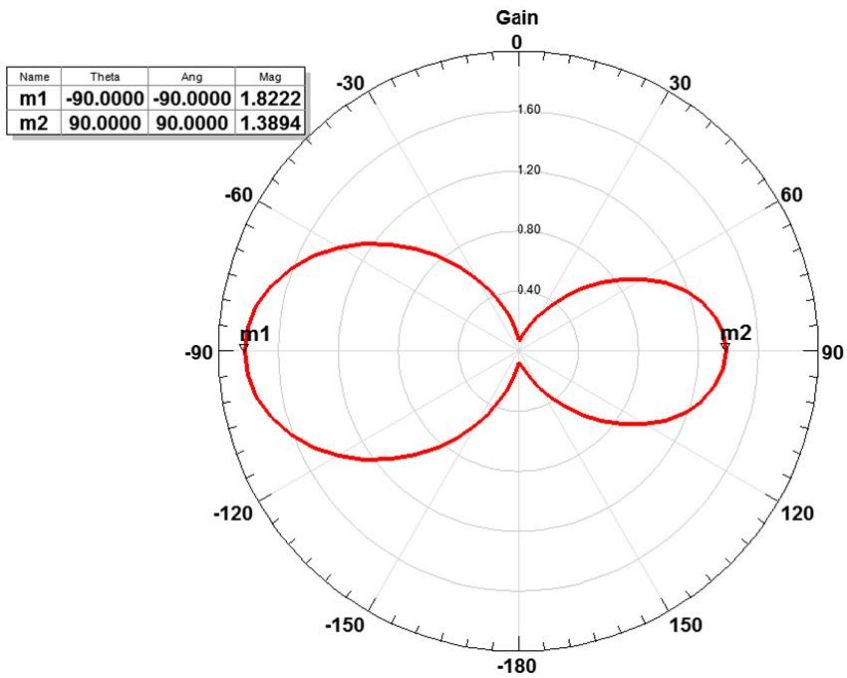

Figure 3-16: Gain of VHF antenna in E-plane ($\varphi = 90^0$) for configuration A

Gain in nadir has also reduced to 1.36 dB from 2.06 dB in free-space, as represented by the plots in Figure 3-17**.**

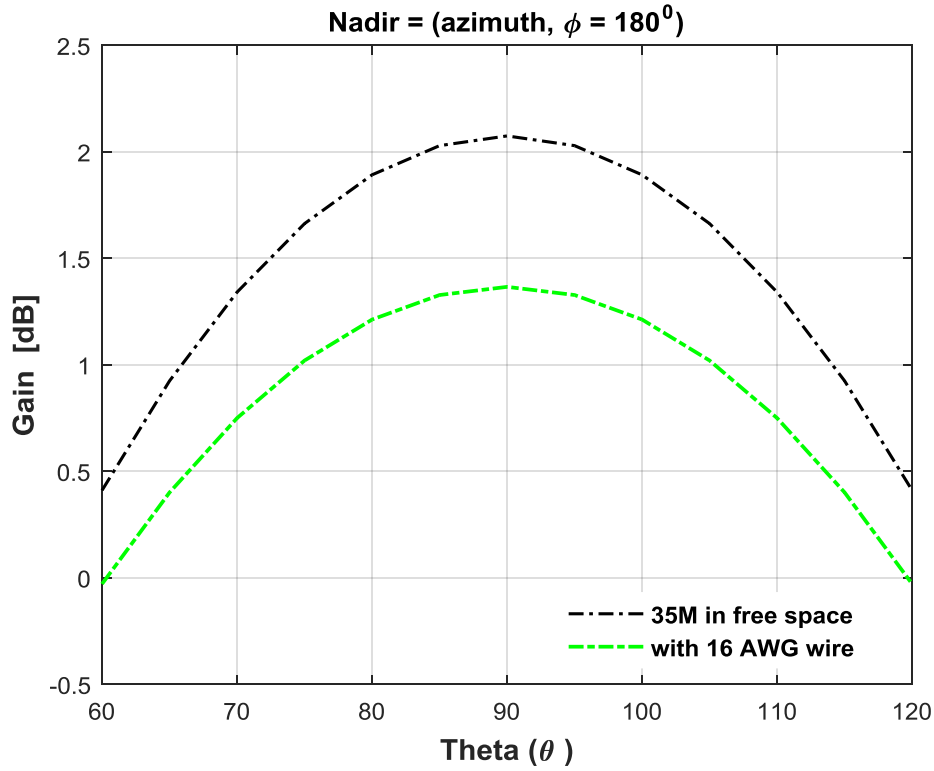

Figure 3-17: Gain in nadir for antenna configuration A

3.3.1.2 Antenna Configuration B

This problem was approached by investigating methods that would help tune the antenna system in to an ineffective array. Various numerical and experimental studies suggest that the reflector spacing and size has negligible effects on the forward gain as compare to that of the director [11]. This important consideration was instrumental in tuning the antenna system, which led to a new antenna configuration implemented by removing the 16 AWG wires as shown in Figure 3-18**.**

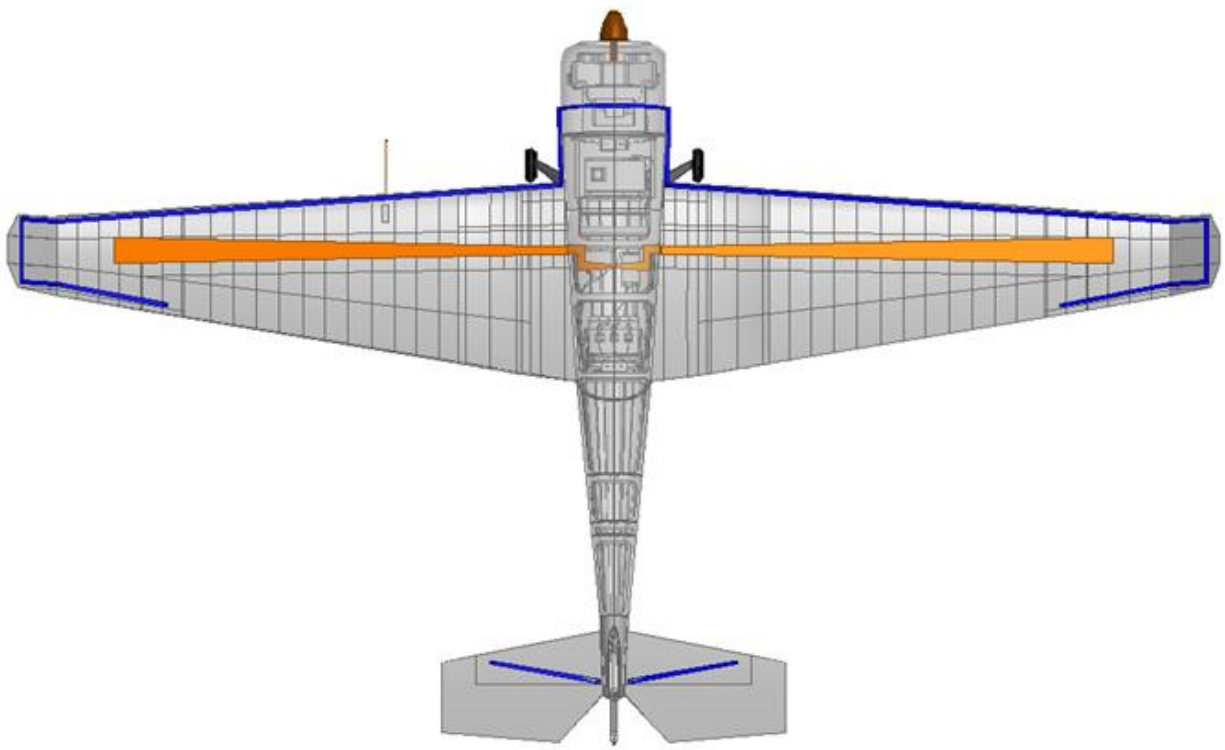

Figure 3-18: Antenna configuration B

Simulated 3D radiation pattern and gain plot in Figure 3-19 and Figure 3-20**,** respectively demonstrate the effectiveness of antenna configuration B.

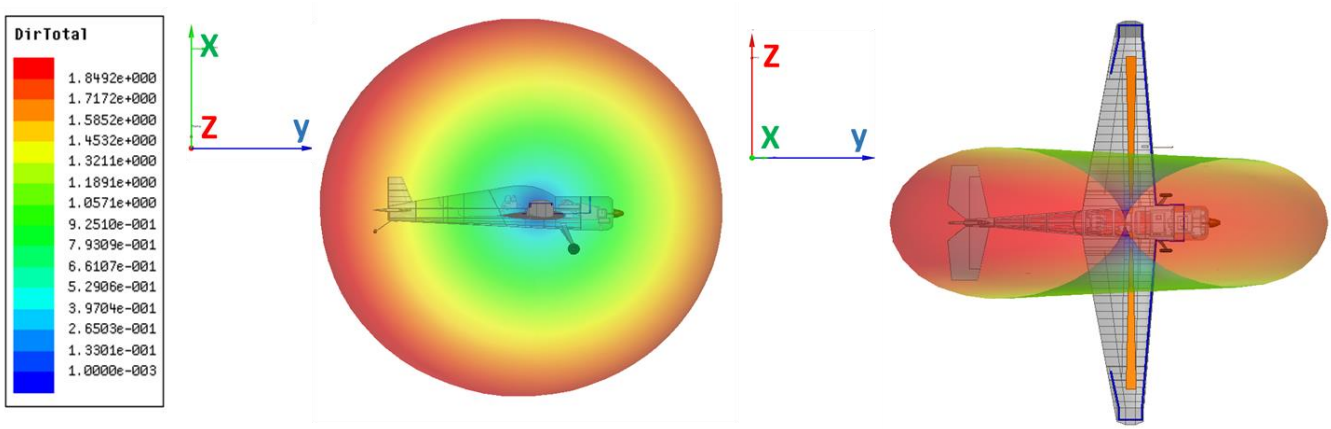

Figure 3-19: Directivity of VHF antenna for configuration B

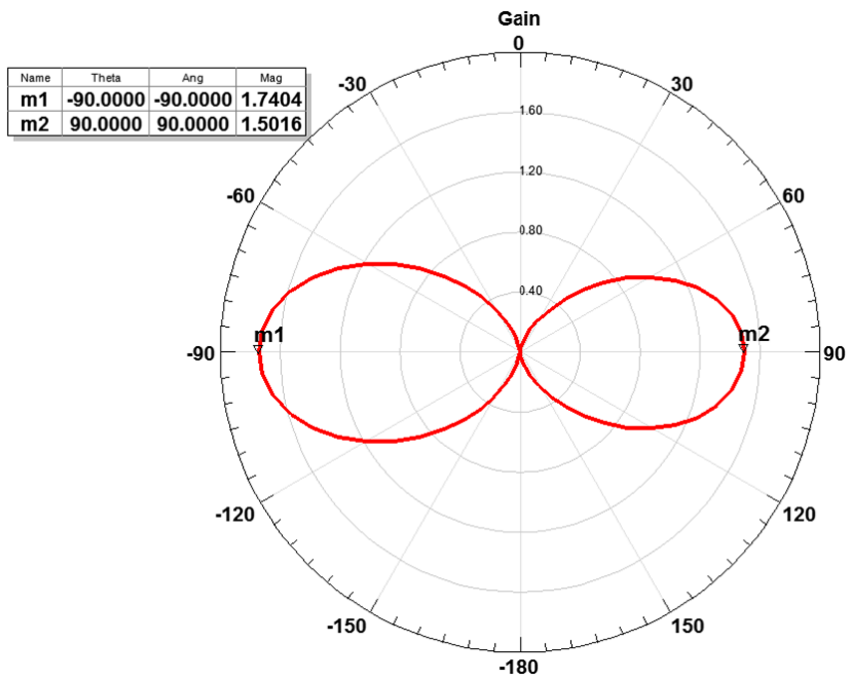

Figure 3-20: Gain of VHF antenna in E-plane ($\varphi = 90^0$) for configuration B

The radiation is closer to omnidirectional pattern making it less directive as compares to the previous configuration. The front to back ratio is down to 0.64 dB and consequently the gain in nadir is back to normal, as shown in Figure 3-21.

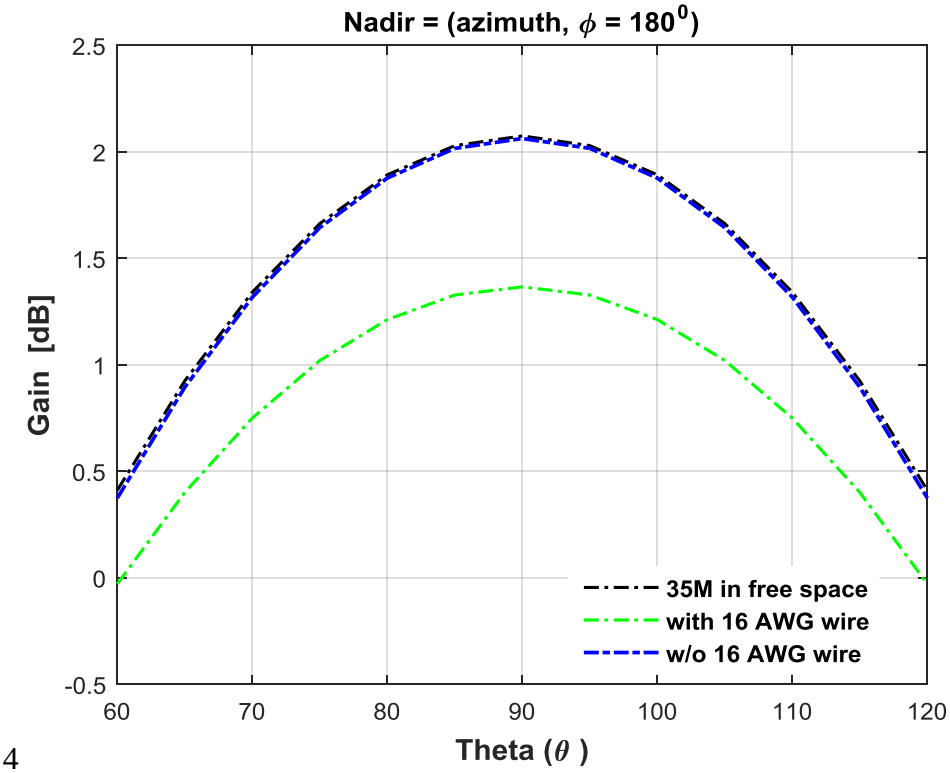

4

Figure 3-21: Gain in nadir for antenna configuration B

Impedance plots in Figure 3-22 illustrate that the influence of mutual impedance has also decreased considerably.

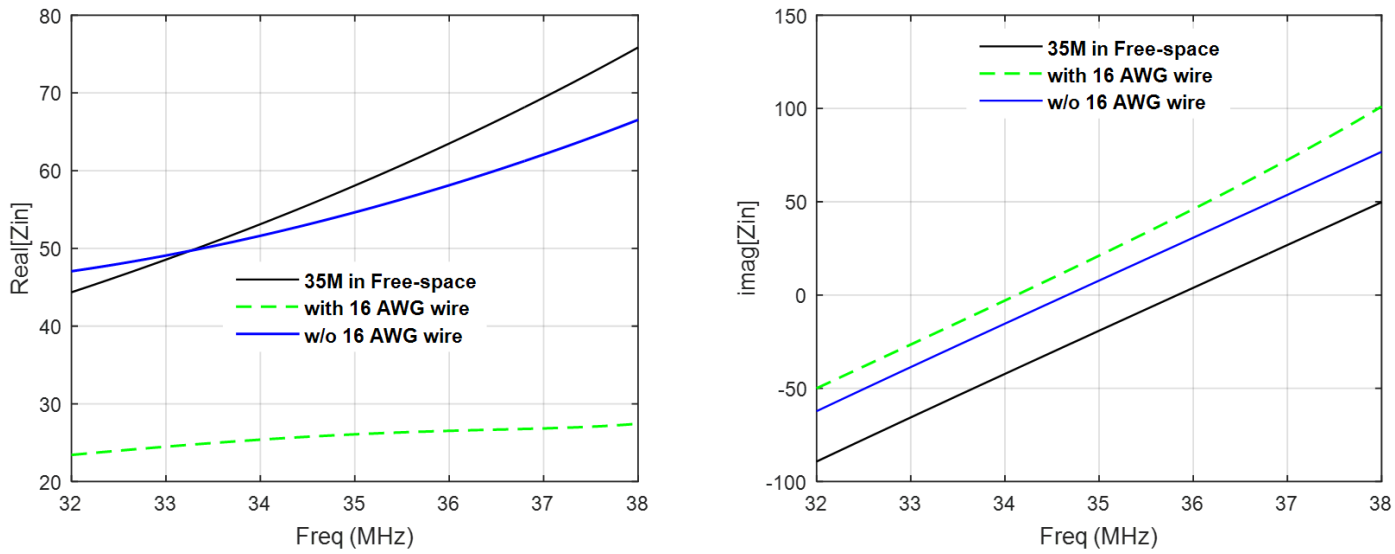

Figure 3-22: Input impedance of VHF antenna for configuration B

Since the driving point impedance is now dominated by antenna's self-impedance, the resonance frequency has shifted closer to that of free-space setup along with significant improvements in return loss as shown in Figure 3-23**.**

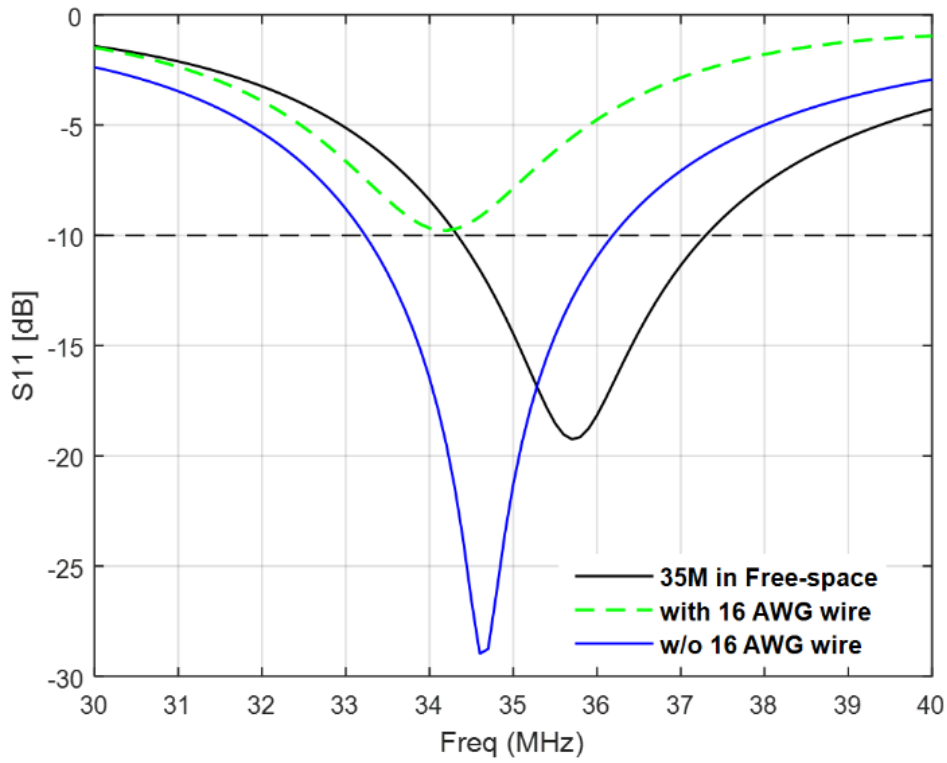

Figure 3-23: S11 of VHF antenna for configuration B

Implementation of antenna configuration B has not only enhanced the antenna performance but it also turned out to be a highly desirable configuration from practicality standpoint, as it gave us the flexibility to remove the 16 AWG wire when operating the radar in VHF band.

3.3.2 Populated UAS: Effects of Avionics on Antenna System

The interference from tightly packed antennas and avionics on a limited real estate leads to further challenges integrating these antennas on the UAS platform. The integrating process for such a complex system requires both engineering disciplines to work closely in order to evaluate system trade-offs and come up with an optimal solution.

3.3.2.1 Populated UAS Configuration 1

The fitness of aircraft is critical for the success of this project, therefore in regards to avionics layout precedence was given to recommendations made by the UAS team. The suggested

avionics configuration, shown in Figure 3-24, was set as a starting point to further evaluate the performance of antennas on a fully populated platform.

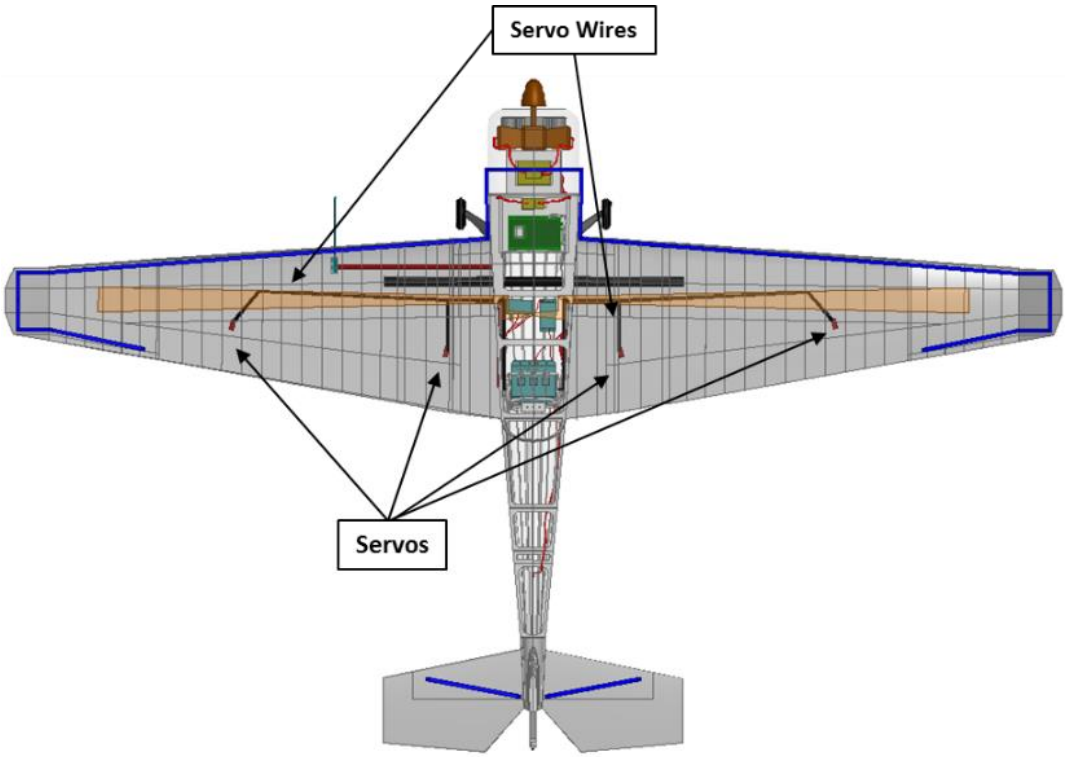

Figure 3-24: Populated UAS configuration 1

The basic layout is such that all avionics modules are enclosed in metal casings and mounted mostly inside the fuselage except for the actuators that are mounted close to the control surfaces. As a result, the effects of mutual coupling inside the fuselage are negligible as relatively small portions of antennas are exposed to the avionics' metallic casings. However, degradation in return loss as shown in Figure 3-25 suggest that the wiring harnesses for aileron actuators interact significantly with 35 MHz antenna.

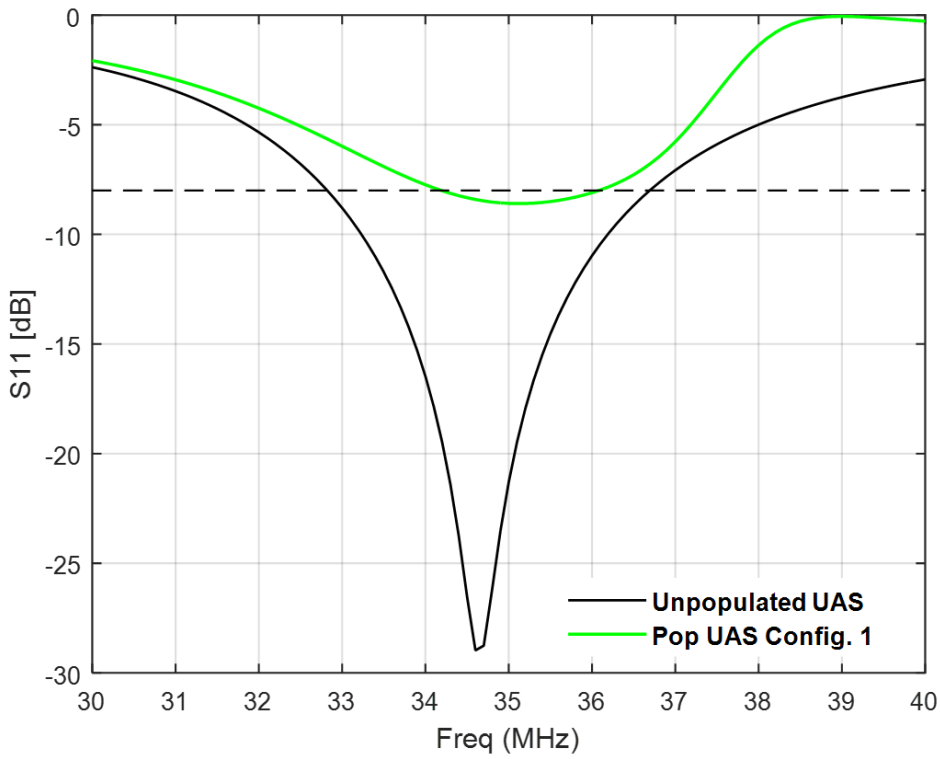

Figure 3-25: S11 comparison between unpopulated and populated UAS

The current induced on servo wires due to capacitive coupling effectively modifies antenna's input impedance and consequently alters the return loss. Such a behavior pertains to the electrical length and close proximity of servo wires to the bow-tie structure, as discussed in section 2.1.3.

3.3.2.2 Populated UAS Configuration 2

A new configuration was proposed without compromising the weight restrictions or the structural integrity of the UAS. According to which, the length of servo wires were shortened and re-routed to increase the distance between the antenna and the wiring harness from 0.5% of the wavelength to 1.5%, as shown in Figure 3-26,

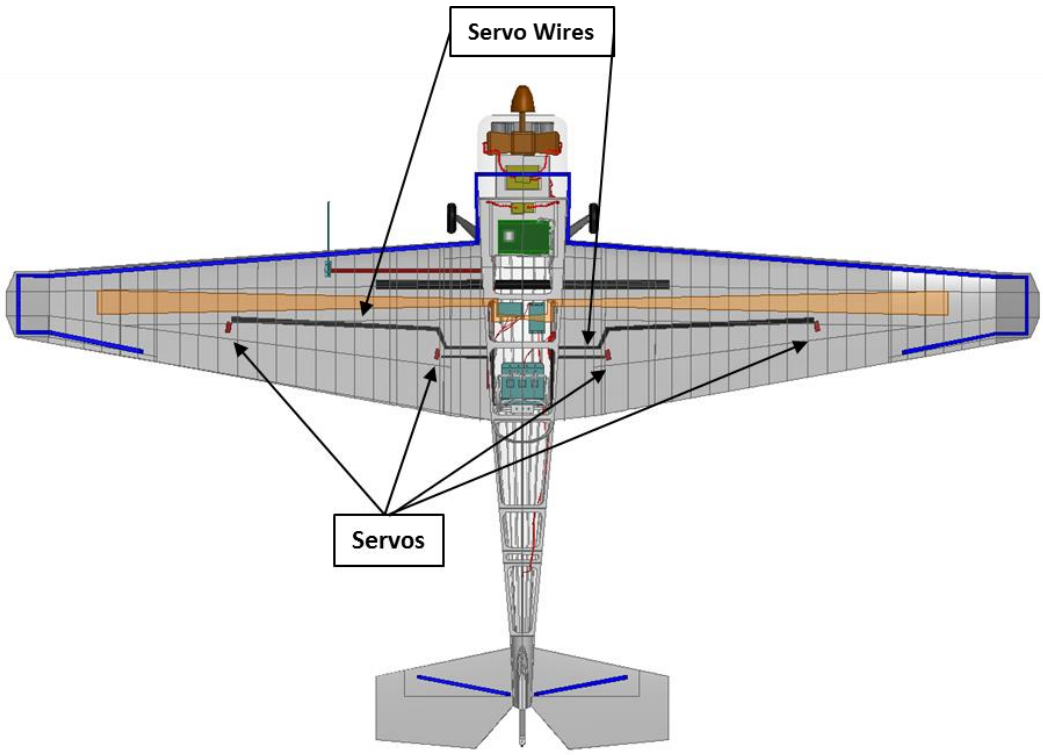

Figure 3-26: Populated UAS configuration 2

The new configuration shows significant reduction in coupling as indicated by simulation results in Figure 3-27.

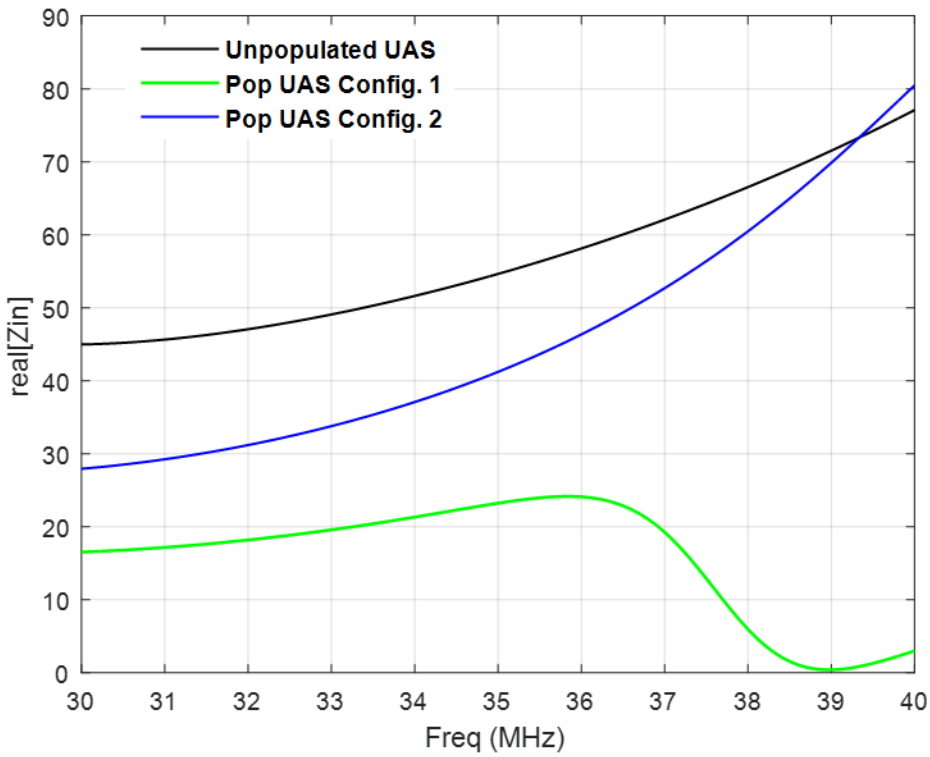

Figure 3-27: Real input impedance comparison between populated UAS configuration 1 and 2

According to Figure 3-27, shift in resistive impedance closer to 50Ω improved the impedance match that led to decrease in reflections from antenna feed, as noted in Figure 3-28.

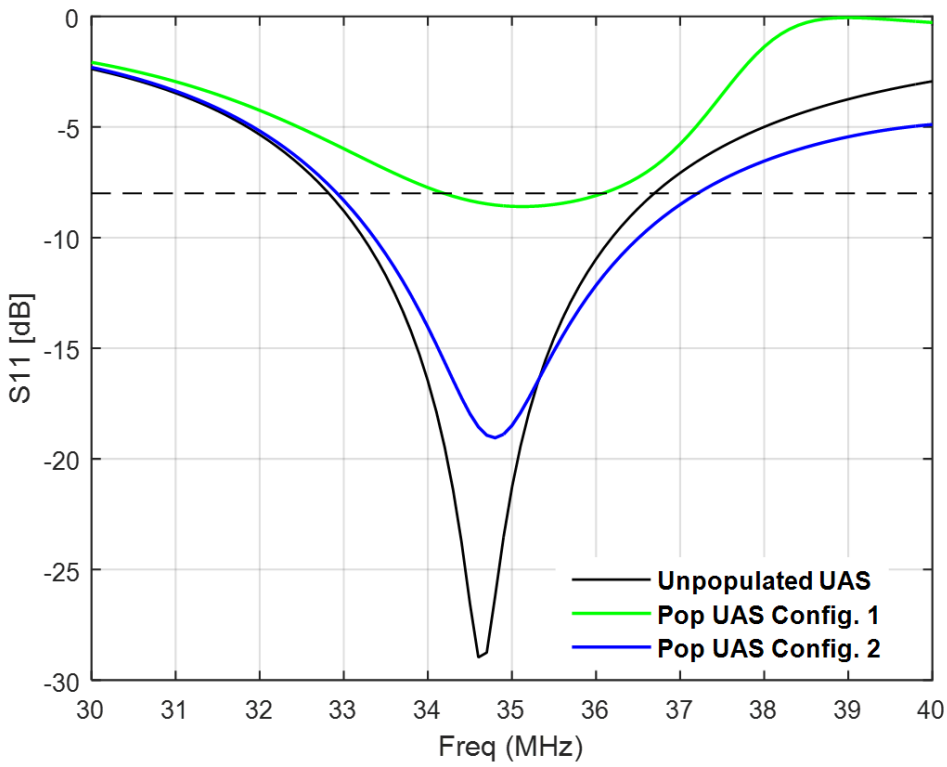

Figure 3-28: S11 comparison between populated UAS configuration 1 and 2

The increase in bandwidth of 35 MHz antenna by 0.5% as compared to that of an unpopulated UAS, shows how bandwidth can be controlled by manipulating the mutual impedance between two elements. The gain at nadir remains close to around 2.1 dB, as shown in Figure 3-29.

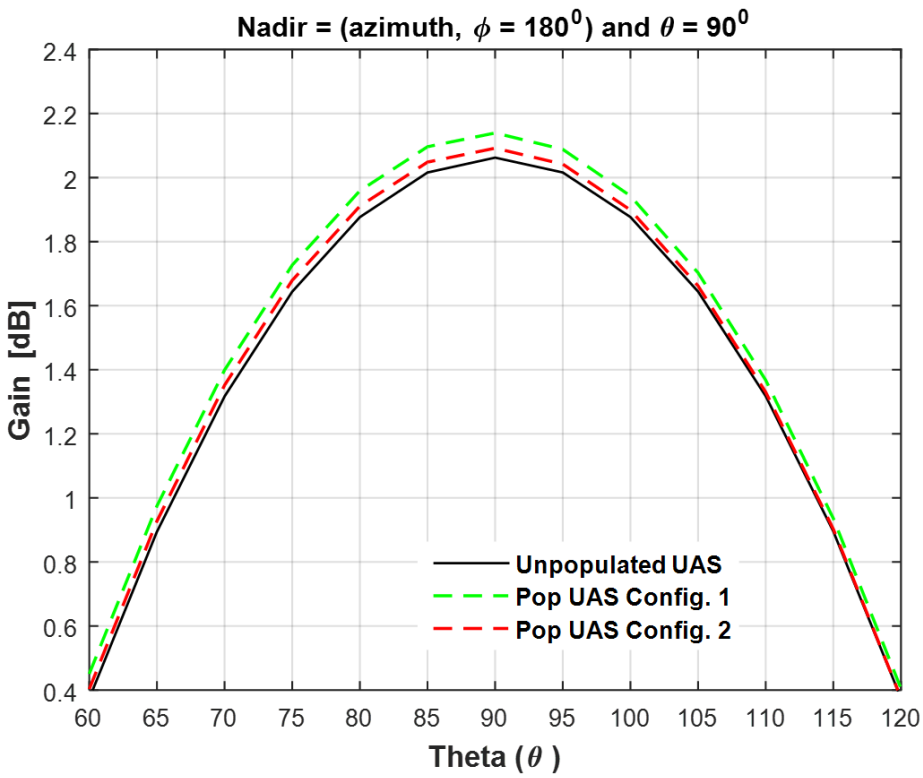

Figure 3-29: Gain at nadir for 35 MHz antenna

The input impedance of HF antenna remains unaffected by its surrounding metallic structures, as it is demonstrated by S11 plots in Figure 3-30.

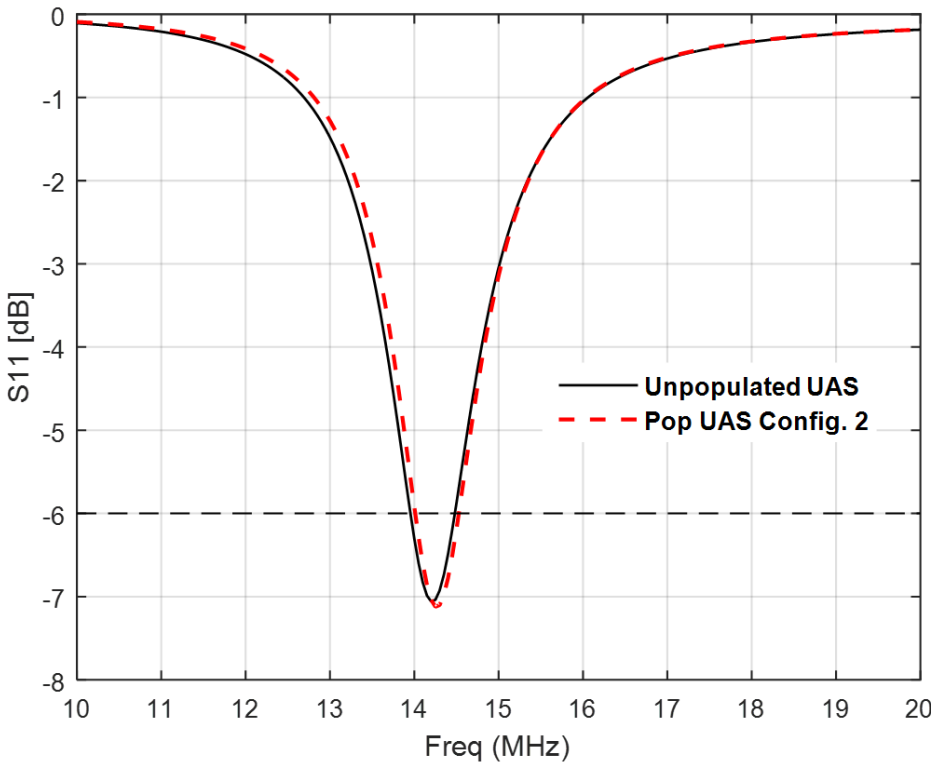

Figure 3-30: S11 of 14 MHz antenna

As shown in Figure 3-31, the gain in nadir has reduced by only 0.15 dB, which is negligible.

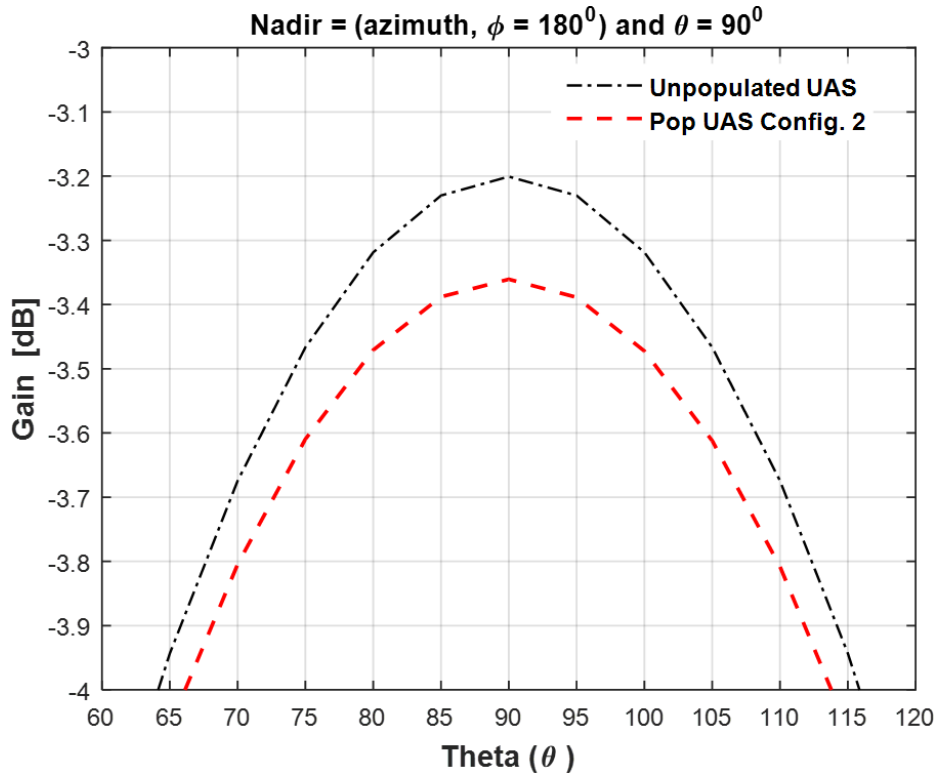

Figure 3-31: Gain at Nadir for 14 MHz antenna

Throughout the integration process the changes incurred in the overall performance of 14 MHz are nominal. This was expected as the electrical length of parasitic metals in near-field are relatively short enough to have any major impact on the HF antenna.

Based on the performance of antennas and from a physical integration standpoint, the populated UAS configuration 2 meet all basic requirements for both the radar as well as the UAS. Therefore, this configuration was locked down as a final integration solution. Photos in Figure 3-32 and Figure 3-33 shows fully integrated antennas on the UAS.

Figure 3-32: Integrated VHF antenna before Monokoting the wings

Figure 3-33: Integrated HF antenna's 16 AWG wires exposed during flight

Finally the bow-tie antenna was measured inside the chamber, whereas 14 MHz antenna was measured using the radar as a VNA during inflight test. Comparison between the measured and simulated antennas are shown in Figure 3-34 and Figure 3-35.

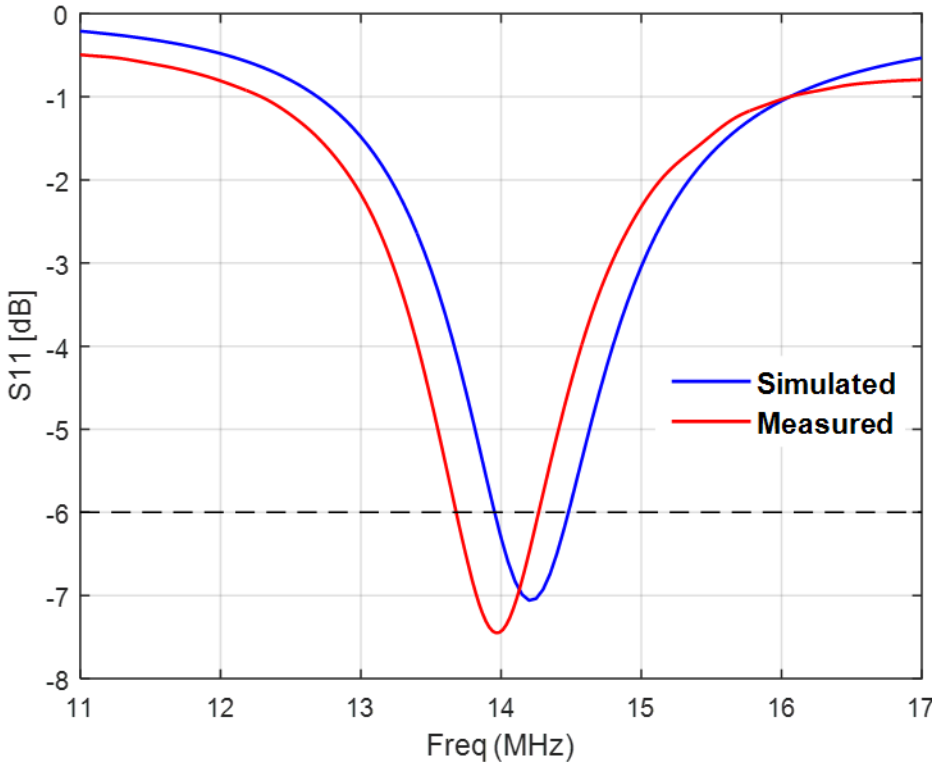

Figure 3-34: Measured vs Simulated S11 of 14 MHz antenna after integration

A slight shift in resonance frequencies from 14.2 MHz to 13.96 MHz and from 34.8 MHz to 34.51 MHz was due to the phase shift incurred by baluns, which were not accounted for in HFSS simulations.

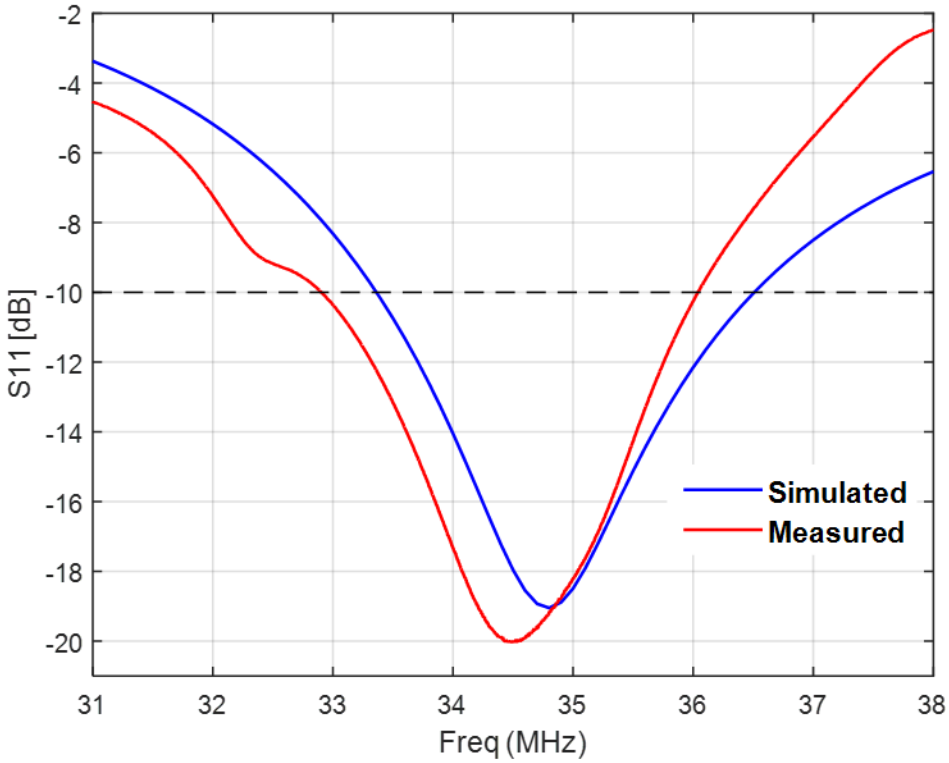

Figure 3-35: Measured vs Simulated S11 of 35 MHz antenna after integration

The measured S11 results are comparable to that of simulated results. This validates the reliability of simulations in regards to other antenna parameters such as gain and radiation pattern.

The purpose of systematically analyzing the performance of antenna system at each integration stage was to evaluate and apply viable trade-offs necessary to meet radar requirements. For this application the performance attributes are defined by antenna bandwidth and realized gain that determines radar's range resolution and SNR, respectively. Figure 3-36 represents the performance of bow-tie antenna at each integration stage as a function of bandwidth and realized gain at nadir. Since the 14 MHz antenna was unaffected throughout the integration process therefore analyzing the performance in such a matter is limited to 35 MHz antenna.

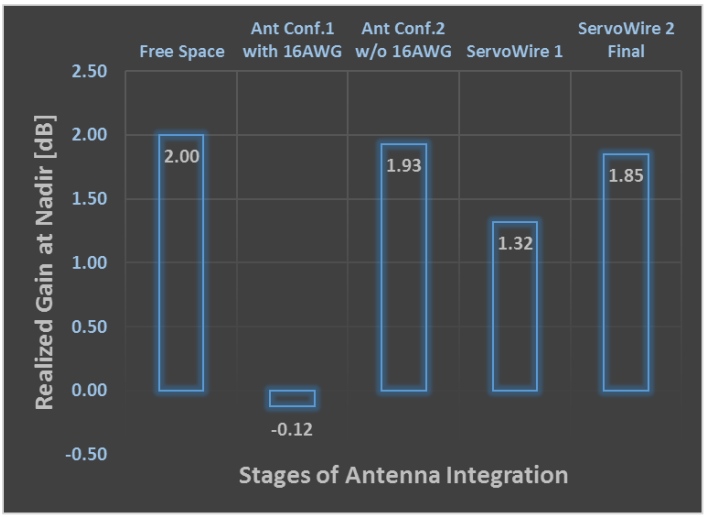

(a)

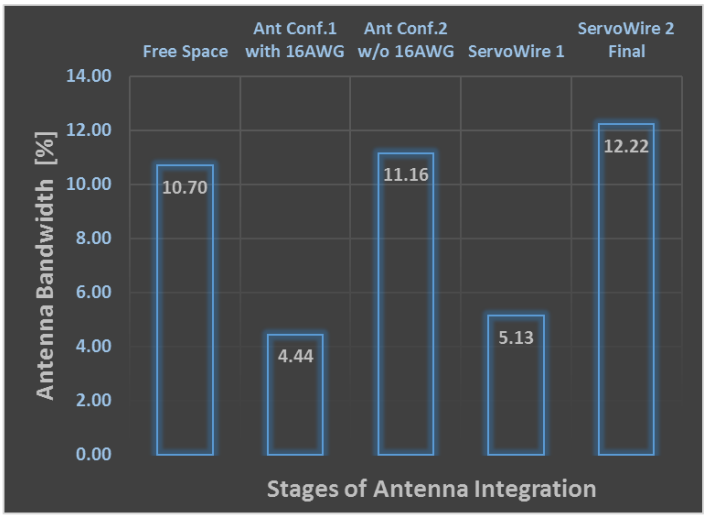

(b)

Figure 3-36: 35 MHz antenna performance at each integration stage

(a) Realized gain at Nadir (b) Bandwidth at 8 dB return loss

Figure 3-36 shows a minor loss of 0.15 dB in realized gain and 1.52 % more bandwidth in the final stage as compared to ideal free-space antenna. These results suggest that the proposed integration solution qualifies as the optimal configuration for a fully populated UAS that not only mitigates drag and weight penalties but also satisfies the minimum requirements necessary for the radar operation.

4 IMPEDANCE MATCHING NETWORK and EMI MANAGEMENT

4.1 IMPEDANCE MATCHING NETWORK

As discussed in section 3.1, the radar's range resolution depends on its operational bandwidth; the greater the bandwidth, the finer the resolution. There are many different ways to define antenna's bandwidth but the most relevant definition explains it as a range of frequencies over which the power delivered to the antenna exceeds a pre-defined threshold. For the widest possible bandwidth the power delivered to the antenna can be maximized if the antenna's impedance is equal to the complex conjugate of the transmitter's impedance. It can be implemented by employing a network of reactive components in between the transmitter and antenna known as impedance matching network.

4.1.1 Co-simulation of 35 MHz Impedance Matching Network

The best design approach for an impedance matching network is based on measured antenna impedance. For that matter an ideal 3rd order lumped LC network using measured driving point impedance of 35 MHz antenna was synthesized in Keysight Genesys. The topology was than mapped on to micro-strip line layout in ADS and simulated with ideal inductor and capacitor values.

Capacitors tend to be more reactive and exhibit lower resistive effects than inductors. Due to high quality factor Q and lower coupling with other components capacitors were treated as ideal components. Inductors on the other hand are more complex. The parasitics of a non-ideal inductor are associated with its physical construction and its placement on the trace [21]. Intrinsic parasitics, such as series resistance and parallel capacitance due to inter-turn winding, varies its inductance and capacitance as a function of frequency that is why inductor's measured s-parameters are

usually provided by the manufacturer. Unfortunately the provided s-parameters did not cover our frequencies of interest so ideal inductor values had to be used for initial ADS simulations.

Method of Moment (MoM) used by ADS is more appropriate for most planar geometries, whereas HFSS's Finite Element Method (FEM) based on volume meshing is more suitable for 3D structures. Therefore to make up for the lack of s-parameter data and to account for mutual inductance between the inductors, HFSS was used as a co-simulator in conjunction with ADS. A step by step procedure for implementing co-simulation is explained in Figure 4-1.

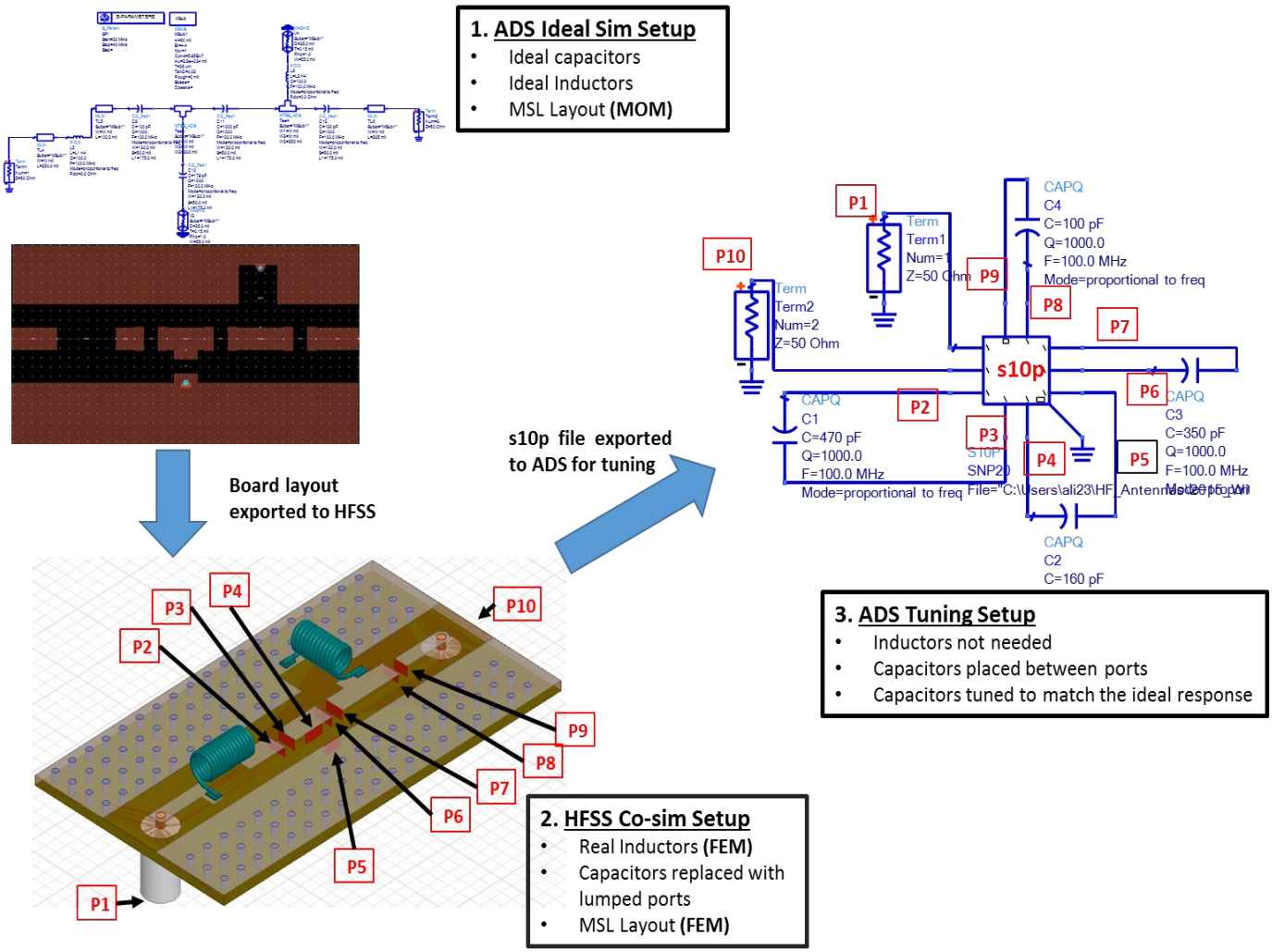

Figure 4-1: Co-simulation Setup

First, ADS board layout files were exported as a DXF/DWG design file and imported into HFSS along with 3D inductor models downloaded from manufacturer's website. In HFSS, material characteristics and simulation ports were added to realize full 3D EM coupling with parasitic effects and inductance associated with each trace in between the capacitors, as shown in co-simulation setup # 2 in Figure 4-1. After the completion of the simulation the s-parameter (.SnP) file was ported into ADS and capacitors were tuned to match the ideal response of the matching network followed by board fabrication and measurements. After populating the board, shown in Figure 4-2, further tuning was carried out to factor in the extrinsic parasitics which arise from solder pads and the way components were placed onto the board.

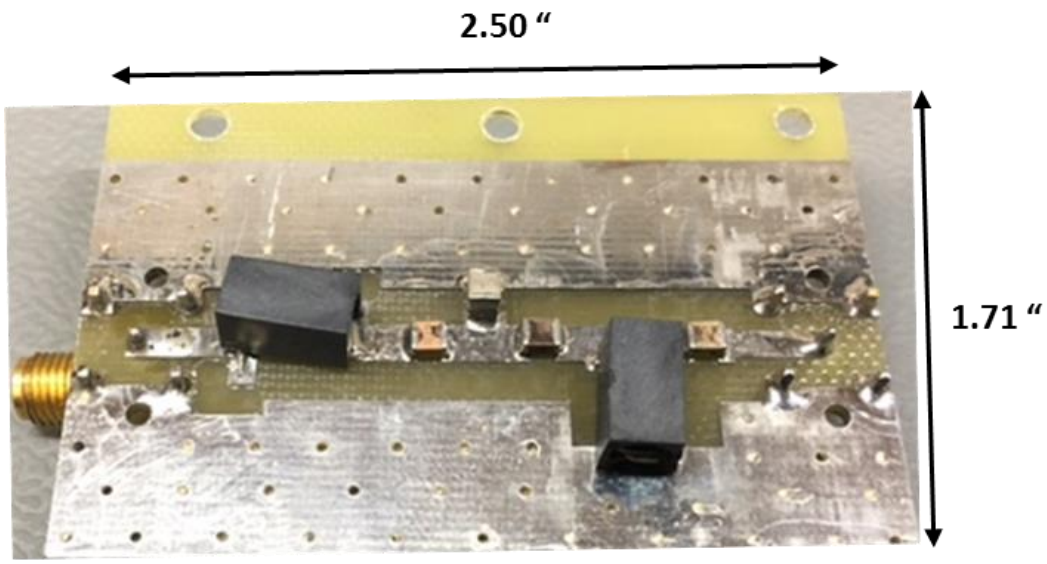

Figure 4-2: Matching network board for VHF antenna

Figure 4-3 reports a significant improvement in the antenna's bandwidth from 3.25 MHz to 5.55 MHz by using the impedance matching network. In addition to that the comparison between the ideal, realized and measured results demonstrates the effectiveness and reliability of co-simulation technique. This technique was used to fabricate filters at other frequencies. For

example, a high rejection high-pass filter used to eliminate interference in the UWB-AWI-Ice system.

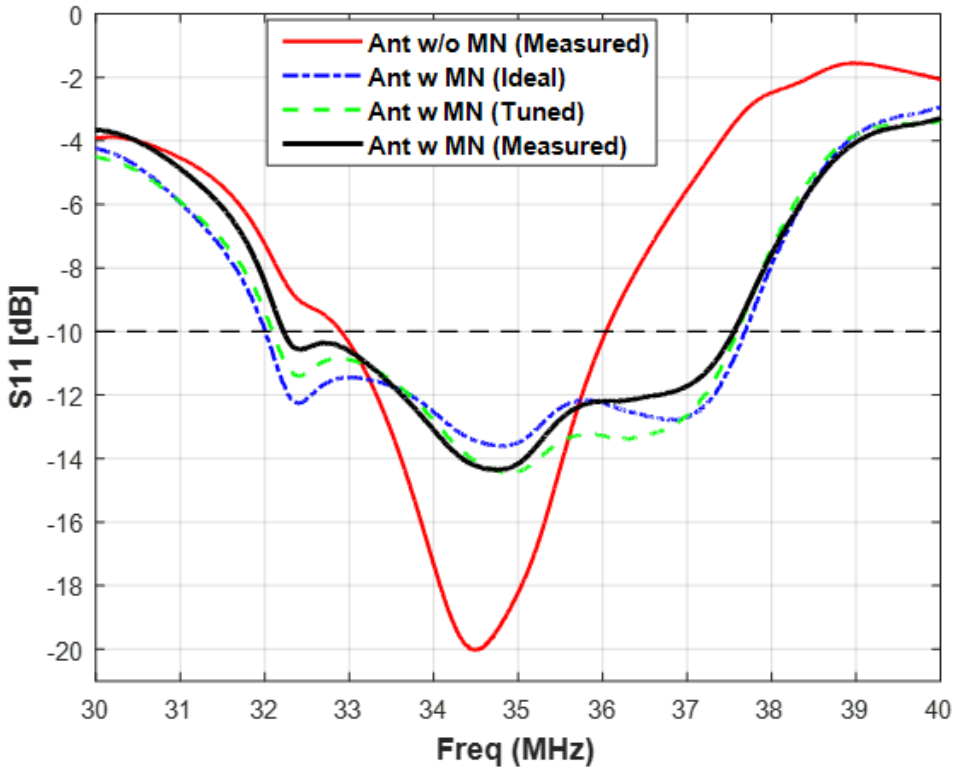

Figure 4-3: Comparison Ideal VS Realized response after co-simulation VS Measured

Since, the input impedance of the matching network is matched to, 50 Ω, characteristic impedance of the transmitter and the output impedance is matched to the input impedance of the antenna. Therefore, in order to determine the insertion loss of the matching network board the output had to be terminated with antenna's impedance at its respective frequencies. Figure 4-4 shows an average insertion loss of about -0.5 dB that corresponds to -10 dB bandwidth in Figure 4-3.

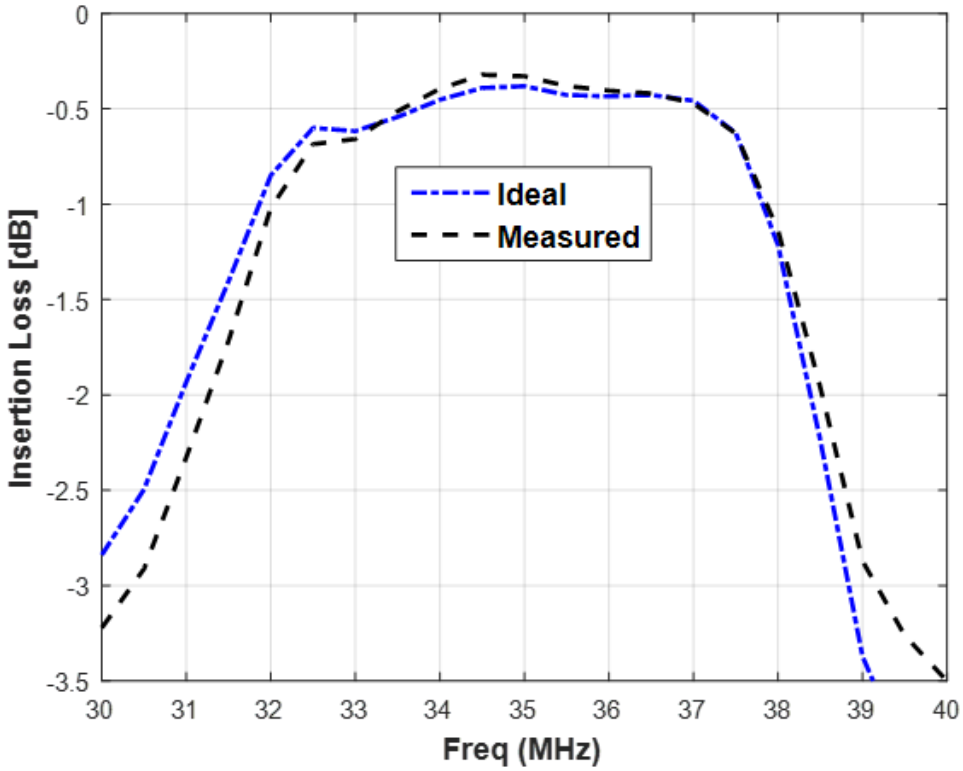

Figure 4-4: VHF Matching Network's Insertion Loss Comparison

Slight difference in the measured and ideal response could be due to the variation in dielectric constant of FR-4 substrate in addition to minor extrinsic parasitics.

4.1.2 Impedance Matching Network for 14 MHz antenna

HF antenna's impedance data, which is necessary to design the matching network, had to be acquired during inflight antenna measurements. The first flight test took place a few days before the system was shipped to Greenland leaving too little time to run co-simulations and board optimization. However, a quick prototype of the matching network board, shown in Figure 4-5, was produced based on MoM simulations in ADS.

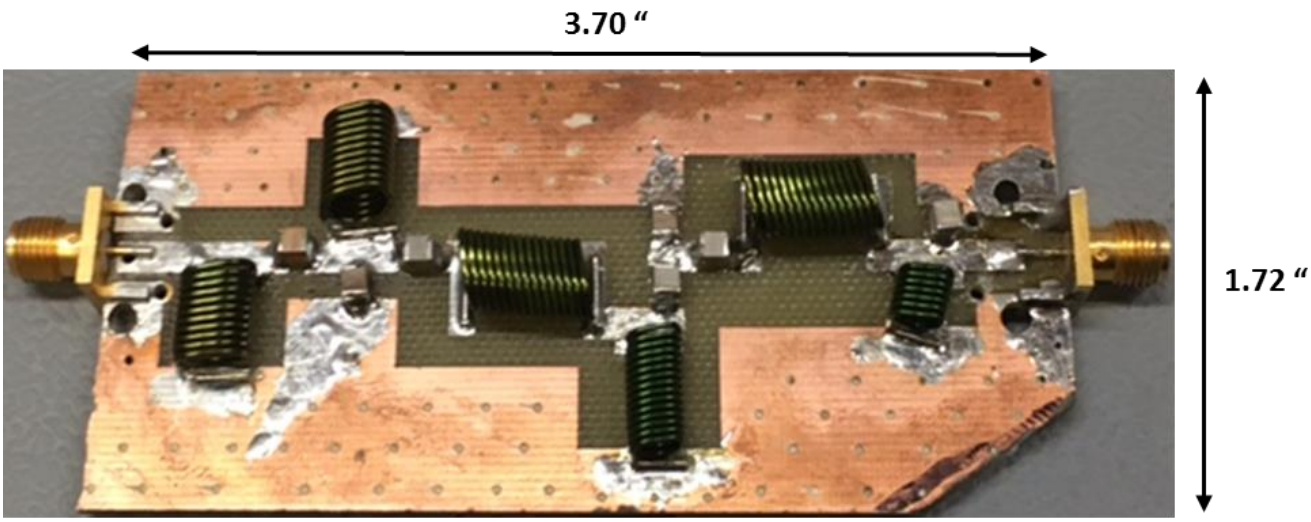

Figure 4-5: Matching network board for HF antenna

The antenna with an attached matching network board was characterized again during the second flight test in Greenland. The measured return loss compared against the simulated results are shown in Figure 4-6**.**

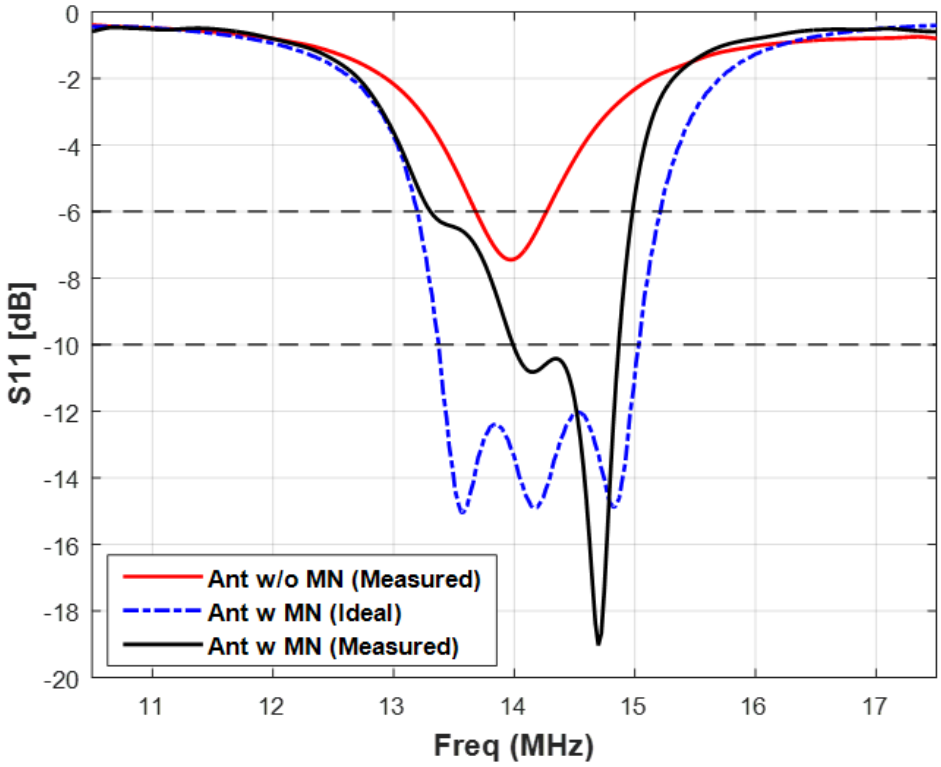

Figure 4-6: S11 of HF antenna with and without matching network

Insertion loss was determined in a similar fashion as it was done for VHF matching network board.

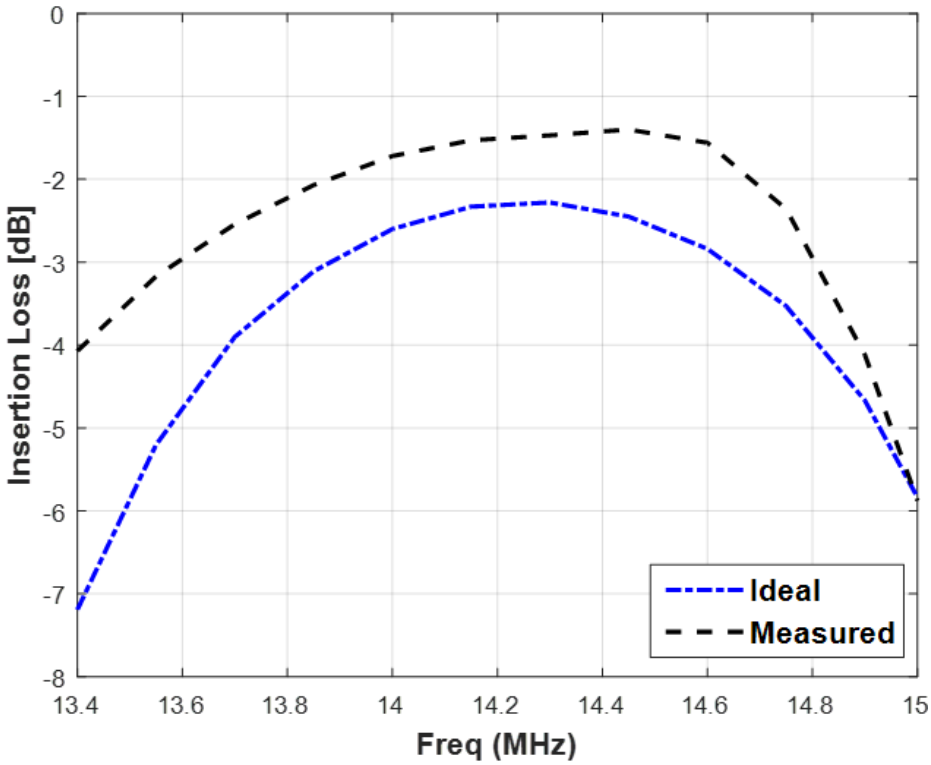

Figure 4-7: HF Matching Network's Insertion Loss Comparison

Results in Figure 4-7 show that the measured response incurred about -1.85 dB of loss, which is 1.75 dB better than of simulated response.

The main reason for the discrepancy between the measured and ideal response with matching network is changes in the antenna impedance between flights. These changes were caused by modifications in cable routing during field operation. It is noteworthy mentioning that the overall response is very sensitive to small shifts in the real and imaginary part of the actual antenna impedance. Therefore the matching network only works as designed provided that the antenna impedance does not change. The measured bandwidth of 0.9 MHz at 10 dB was considered to be within acceptable range. An additional tuning step was thus required to achieve the desired

response. Figure 4-8 shows the results of a simulation where the matching network was detuned to match the measured response. Detuning was done by only modifying the capacitor values in Keysight ADS. The response matches relatively well across the band, which indicates the ability to tune the existing response to increase the bandwidth. The agreement below 14 MHz is not as good as in the upper part of the band and is attributed to effects of board parasitics and more pronounced mutual coupling between the inductors. For best results it is therefore recommended to incorporate 3D EM simulations in the board development cycle, leading up to the final optimization of fabricated matching network.

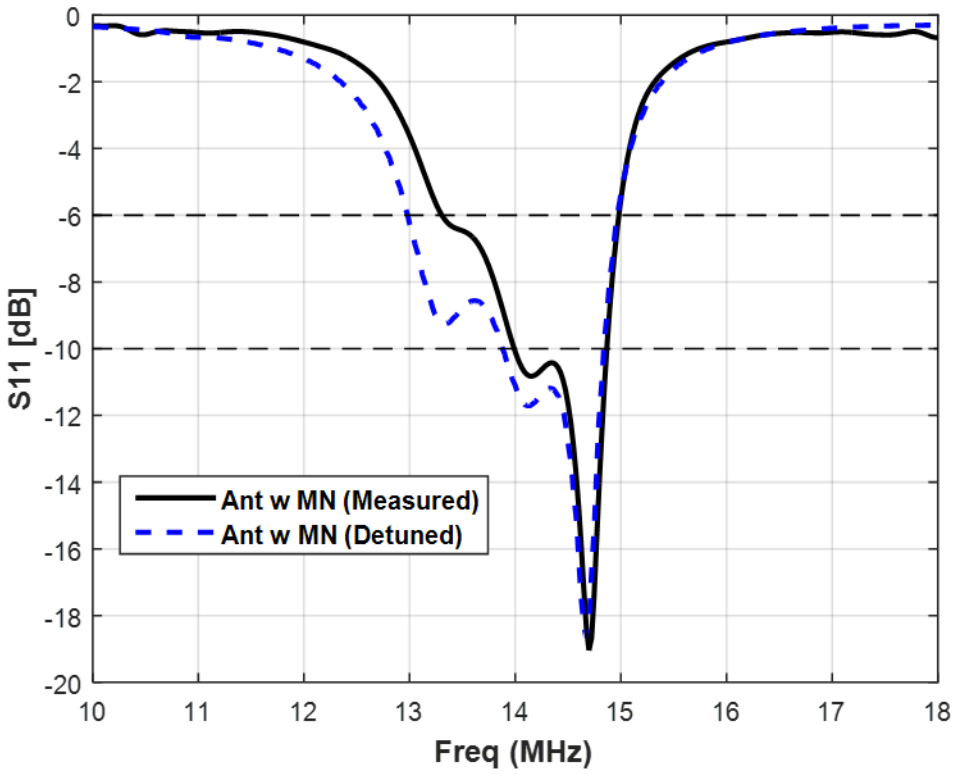

Figure 4-8: HF Matching Network detuned to match the measured response

4.2 ELECTROMAGNETIC INTERFERENCE (EMI) MANAGEMENT

A noise free operational frequency band is necessary to avoid any artifacts in the depth sounder's echogram. Although radio frequency interference (RFI) from UAS's on-board avionics and engine is inevitable, it can certainly be suppressed to an acceptable level. EMI measurements play a crucial role in identifying and mitigating unwanted system noise in radar's band. Most EM compatibility (EMC) issues are decomposed in to three main segments [22]:

1. Emitter: Noise Source
2. Coupling Path: Conducted or Radiated
3. Receptor: Radar system

For such a complex system an extensive EMI characterization test matrix was developed, as shown in Table 4-1.

Device Under Test (DUT)	Configuration and test setup	Power Source		Motivation/Expected outcome
Entire System	All systems powered up and running.	External Battery With avionics box	G1X's Power supply with avionics box	❑ Noise characterization of the entire system, as is. It can be used later for comparison purposes.
Avionics Box	All servos and avionics replaced by equivalent passive loads	External Battery With avionics box	G1X's Power supply with avionics box	❑ Determine how much noise suppression is possible ❑ If needed integrate EMI considerations in to avionics box's design.
Servos with Power-safe RX module	PWM signal bypassing We-pilot and controlled directly through power-safe Rx module. 1. Servos <u>not</u> actuating 2. All servos actuating	External Battery w/o avionics box	G1X's Power supply with avionics box	❑ Ensure proper shielding of servo wires and determine its susceptibility ❑ Check if servo wires are of appropriate lengths to avoid any self-resonance in radar's frequency. bands.
We-pilot	All avionics OFF than turn on each associated system one by one.	External Battery. w/o avionics box	G1X's Power supply with avionics box	❑ Noise characterization. ❑ Test again after applying RFI suppression techniques.
AFF	By itself (UAV not required)	External Battery. w/o avionics box	G1X's Power supply with avionics box	❑ Noise characterization. ❑ Test again after applying RFI suppression techniques.
Pitot-tube	By itself (UAV not required)	External Battery. w/o avionics box	G1X's Power supply with avionics box	❑ Noise characterization. ❑ Test again after applying RFI suppression techniques.
Alternator test	By itself **Test fixture needed.*			Feasibility of using alternator when: ❑ Radar is ON and alternator is <u>NOT</u> used as primary power source. ❑ Radar is OFF and alternator is used as primary power source

Table 4-1: G1X's RFI Characterization Test Matrix

Based on platform availability and time the above test matrix was confined to only two major noise sources: the main power supply for avionics and servo wires.

4.2.1 EMI Characterization and Mitigation of UAS's Power Supply

The UAS was equipped with an off the shelf DC power supply specifically designed to utilize the AC voltage from on-board engine alternate. Switching power supplies are efficient but noisy due to the harmonics of high switching frequency and under-damped oscillations in the switching circuit. Inherently switching power supplies are major sources of broadband noise Therefore, it constituted a good starting point for EMI measurements with the test setup shown in Error! Reference source not found..

Figure 4-9: Test setup for EMI measurements

4.2.1.1 Tests Setup for RFI Measurements

The receiver is a cascade of two low noise amplifiers (LNA) with a total gain of 37dB. A band-pass filter (10-40MHz) and a low pass filter (LPF) outside the chamber connects to a bi-conical cage antenna inside the chamber and within a near-field range to DUT.

Device under test (DUT) is SREG500U power supply that has a build in switching mode power regulator to convert AC coming in from engine alternator of G1X to DC. The measurement

setup includes a 60 Hz Variac used as an AC input to DUT. In order to characterize the noise only from the power supply, a passive resistive load was fabricated that draw about the same amount of current as that of HF sounder radar from the power supply's 28Volts output.

The intent of the test procedure was to start with a baseline measurement that represents the highest obtainable sensitivity of the receiver. The first step was to measure the thermal noise of the receiver by replacing the measurement antenna with a 50Ω termination at the input of the LPF. Then the antenna was connected back to measure the background noise of inside the chamber with everything turned off. Finally to check for any noise contribution from Variac it was turned on with DUT remained off. Once the baseline measurements were taken the power supply was turned on with the passive load connected at its output.

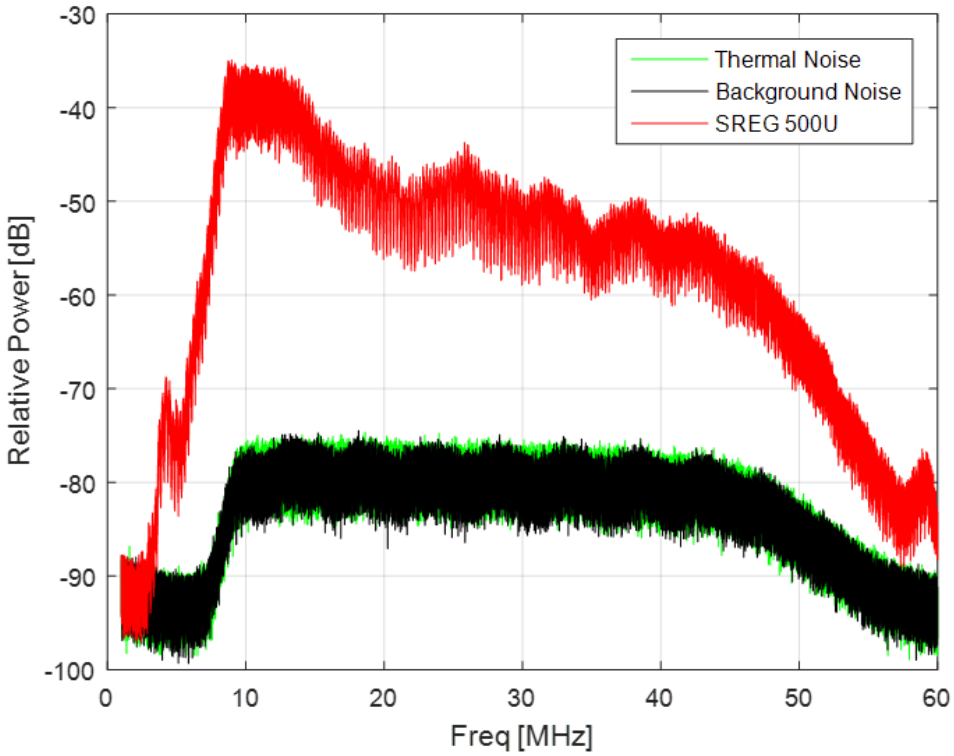

Figure 4-10: SREG 500U power supply EMI measurement results

Baseline measurements in Figure 4-10 show no contributions from any external EMI source and sets the receiver sensitivity to about -80 dB. The noise radiated by the power supply is about 40 dB relative to the baseline measurement in HF band and 25 dB in VHF band.

Implementation of various EMI suppression techniques such as shielding the power supply and wrapping the power cables around ferrite beads did not show much improvement. Therefore, a new power supply was developed to allow us to implement EMC considerations in to the design phase. The proposed design was simply a bridge rectifier for AC to DC conversion and after some passive filtering the output is fed in to SynQor's® InQor90 DC to DC converter to filter out any remain ripples, resulting in to a "cleaner" DC output. SynQor® power converters were chosen because of their low noise and high efficiency. The fixed frequency switching feature in SynQor® DC-DC converters provides predictable EMI and can also be locked in to a desired frequency via external clock from radar's digital section. A very basic layout was quickly put together to test the EMC performance of SynQor® converters before moving forward with a fully integrated design.

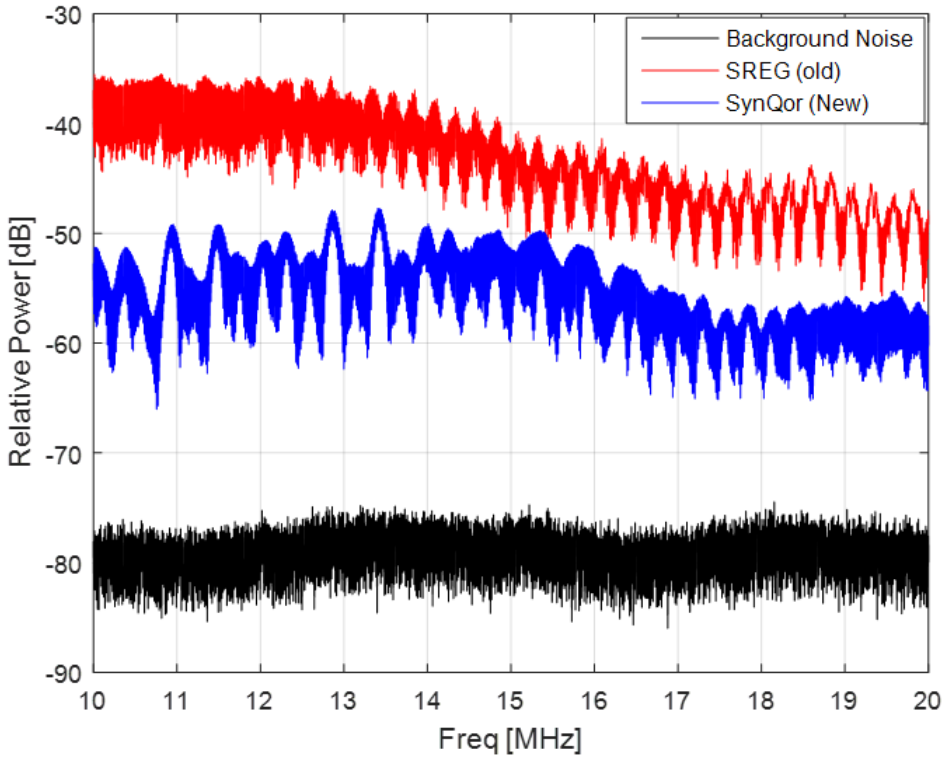

Figure 4-11: SREG 550U vs SynQor based power supply in HF band

The test equipment setup was kept constant to ensure that the measured outcomes were representative of experimental parameters and not setup variance. The measurement results in Figure 4-11 points out more than 10 dB improvement around 14MHz.

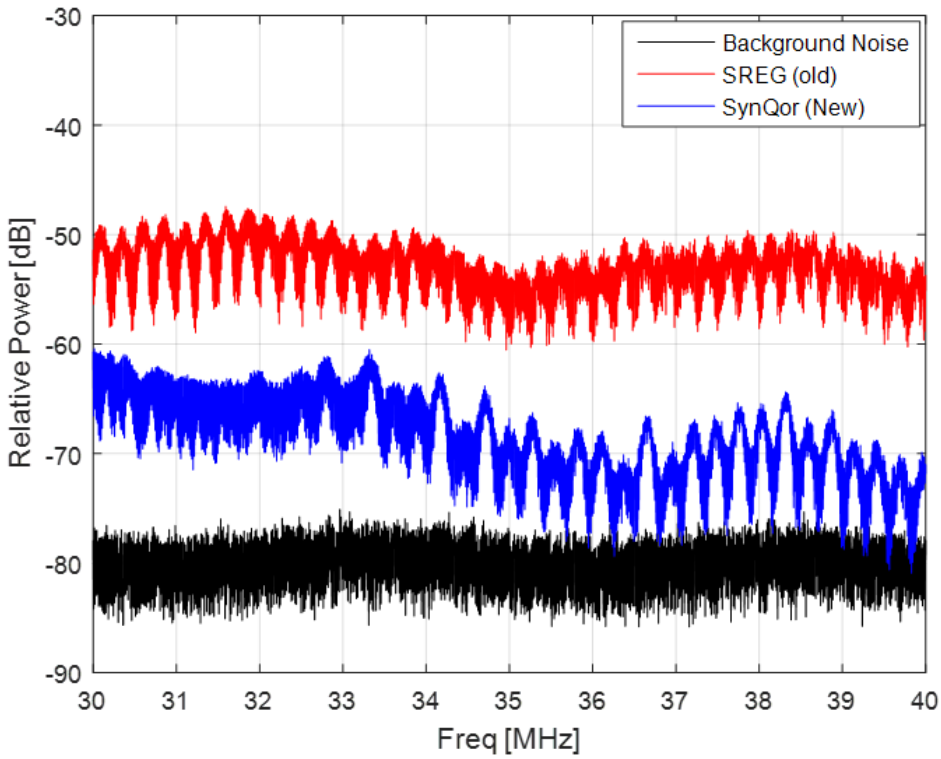

Figure 4-12: SREG 550U vs SynQor based power supply in VHF band

A 20 dB attenuation in the VHF band is noted in Figure 4-12. Significant improvement in both frequency bands demonstrated the viability of low noise SynQor® modules for this application. Further improvement could easily be achieved by implementing EMC design considerations in PCB board layout along with proper shielding and effectively employing Faraday's cage approach.

It is noted that the plots presented above were produced from spectrum analyzer measurements. This was an adequate technique to quantify relative noise power changes. For future work, the noise signals should be captured with the radar and verify the effectiveness of 0-pi inter-pulse modulation to reduce undesired coherent signals.

4.2.2 EMI Measurements and Mitigation of Servo Wires

EM interference depends not only on the source but also on the coupling path. Hence, making the coupling path as ineffective as possible can significantly reduce noise. Radiated coupling paths mostly involve cables as they have the potential for emitting or picking up electromagnetic energy. The mechanism responsible for radiated electromagnetic fields are attributed to the presence of time-varying current on wires, PCB lands, or any other conductor in the system [22].

Actuators on UAS's control surfaces are controlled by pulse width modulated (PWM) signals that are generated from a radio controlled driver circuit commonly known as power-safe receiver module. Given the location of most actuators the wires are electrically long enough, i.e. greater than $\lambda/20$, to radiate the control signals if not shielded properly. This poses a big problem as time varying PWM signals produce random noise that is picked up by the antennas and clutter the radar as well as increase the radiated susceptibility of other on-board systems. A set of RFI measurements were taken to serve two purposes:

1. Investigate the most effective shielding techniques for servo wires.
2. Conduct a feasible study of two different servo brands, HiTec and Volz**,** in regards to better EM compatibility.

For comparison purposes, the shield of the cable under test were terminated in three different configurations as illustrated in Figure 4-13, Figure 4-15, and Figure 4-17. The test setup used was same as in the previous experiment but the baseline measurement was taken again. Once the baseline measurement was established, degradation measurements were taken systematically. DUT in the first experiment included two approximately 7.5 feet long servo wires connected to

battery powered power-safe module (PWM driver circuit) on one end and to HiTec HS-7940th servos on the other end. The shielding configuration for DUT 1, shown in Figure 4-13, was the standard setup routinely followed by the UAV team.

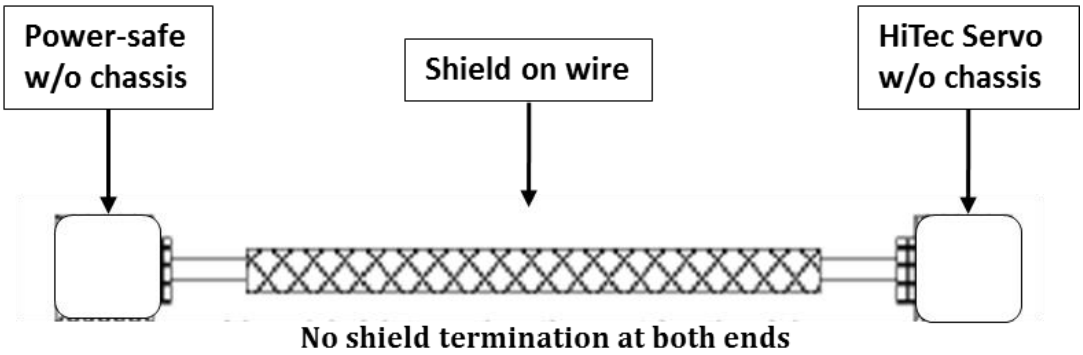

Figure 4-13: Cable shielding configuration for DUT 1

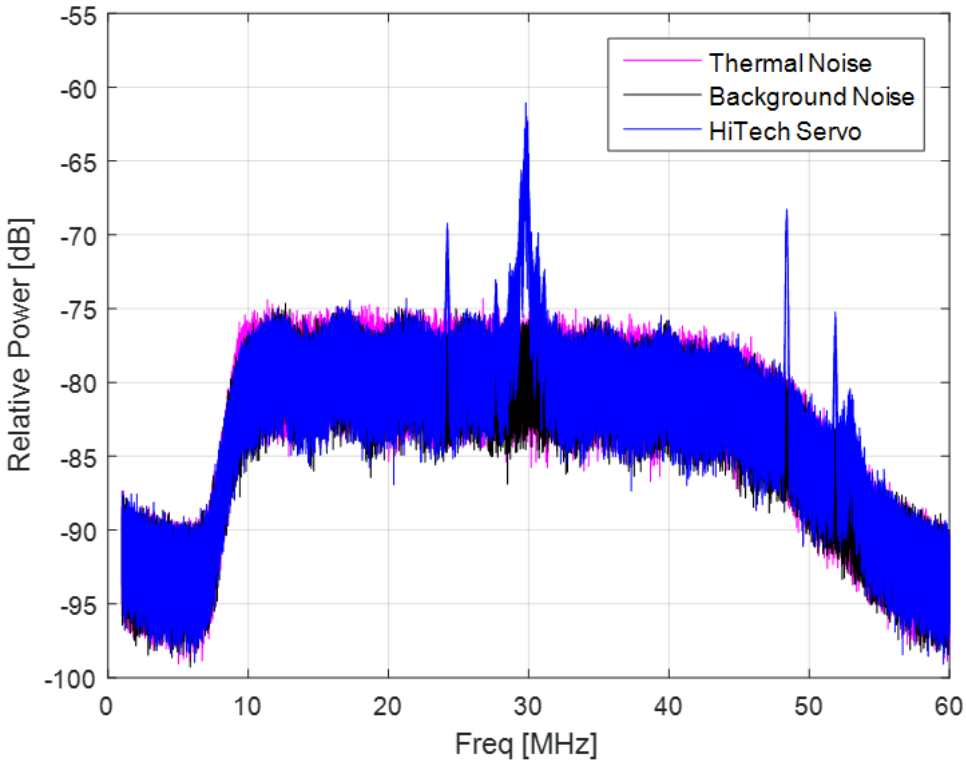

Figure 4-14: Measured RFI for HiTec HS-7940th servos based on DUT 1

Results in Figure 4-14 shows a 13 dB peak above the noise floor at around 30 MHz. The location of the peak in the frequency spectrum depends on the width of the PWM signal but more importantly the electrical length of the shield. This leads us to investigate the noise performance of high end Volz DA 22-06-2605 servos. The added advantage of using Volz servos is that they are designed by taking EMC considerations in to account and comes standard with metallic chassis and connectors to provide better EMI/RFI shielding. The standard shielding configuration of Volz servo is shown in Figure 4-15.

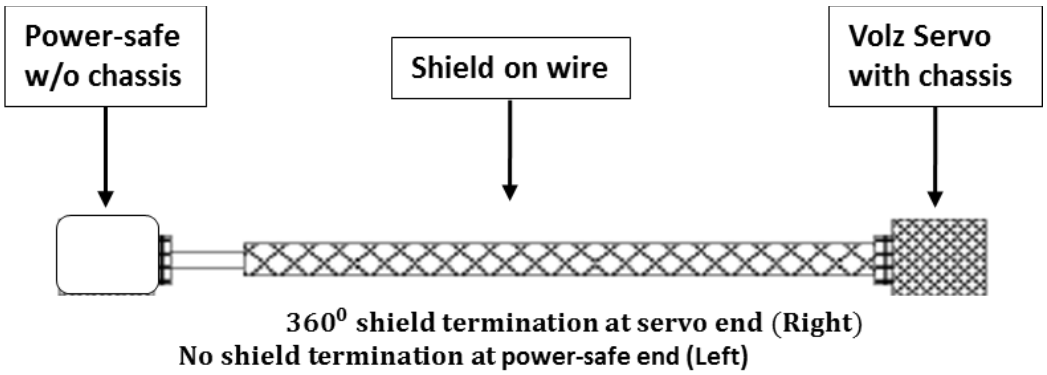

Figure 4-15: Cable shielding configuration for DUT 2

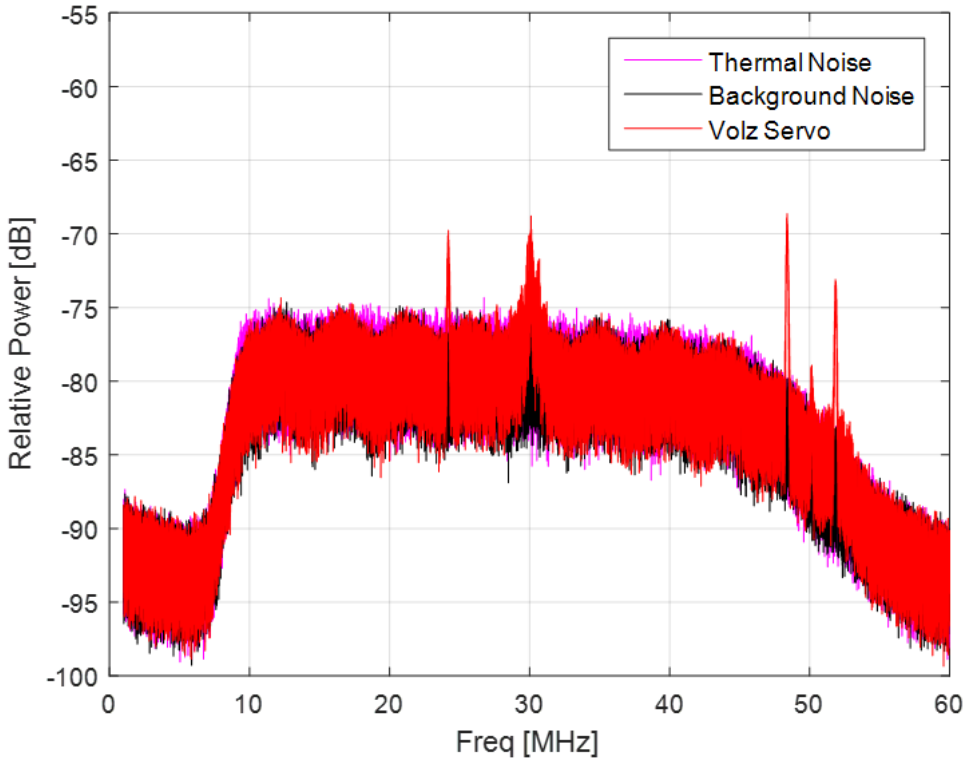

Figure 4-16: Measured RFI for Volz DA 22-06-2605 servos based on DUT 2

As expected the peak in Figure 4-16 is reduced by 7 dB at around 6 dB above the noise floor but not completely eliminated. It pertains to the unterminated end of the shield on the power safe side, which acts as an unintentional antenna. At ¼ λ, the shield becomes an effective monopole antenna [22]; in this case, the 7.5 feet long cables are about ¼ λ at 30MHz.

In an effort to reduce radiated emissions it is essential to produce "antennas" having poor emission properties. A simple solution to this problem is to place the power safe module inside a metallic enclosure box/chassis and terminate the cable's shield to the conductor's chassis, as shown in Figure 4-17. The entire shield turns into a Faraday's cage. In principle, the incident electrical field rearranges the charges on the metallic surface, which than generates opposite electric field and as a result cancels out the incident E-filed. Similarly the incident magnetic field

induces eddy's current, which in turn create magnetic fields that oppose the oncoming magnetic fields.

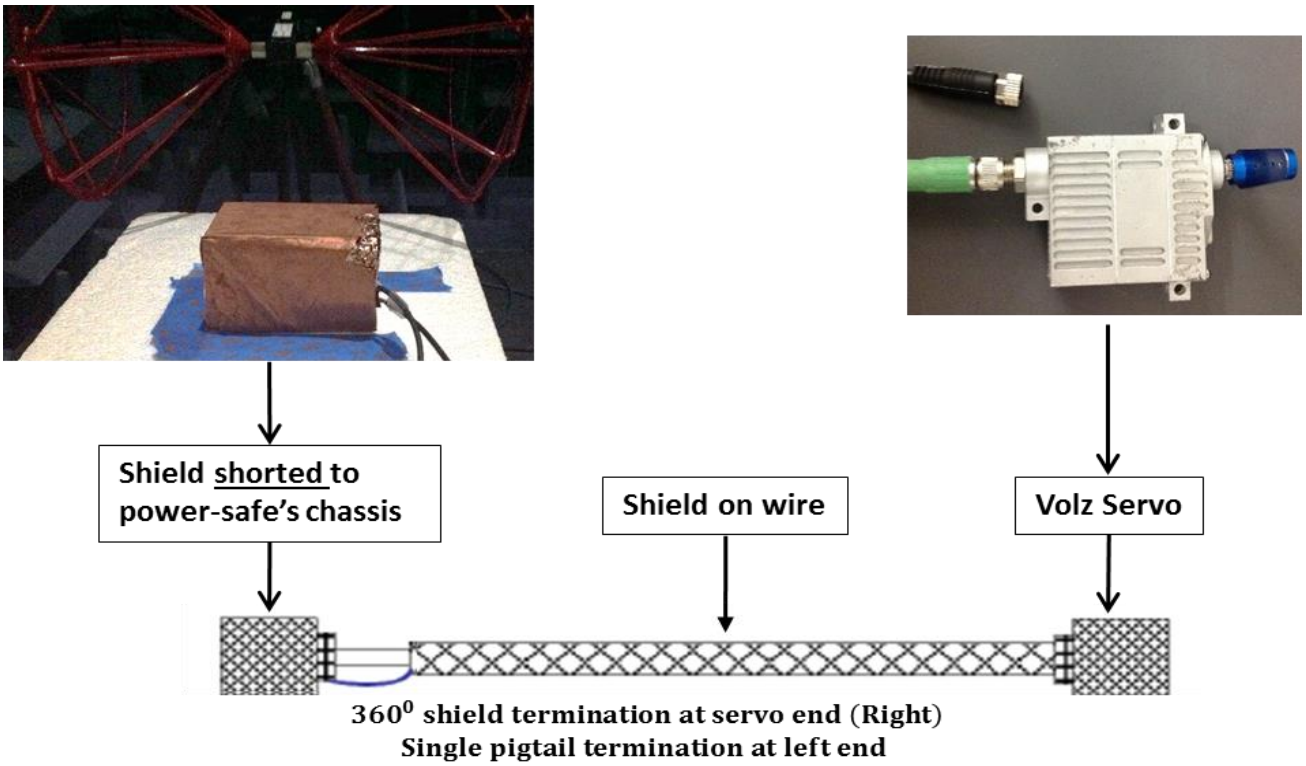

Figure 4-17: Cable shielding configuration for DUT 3

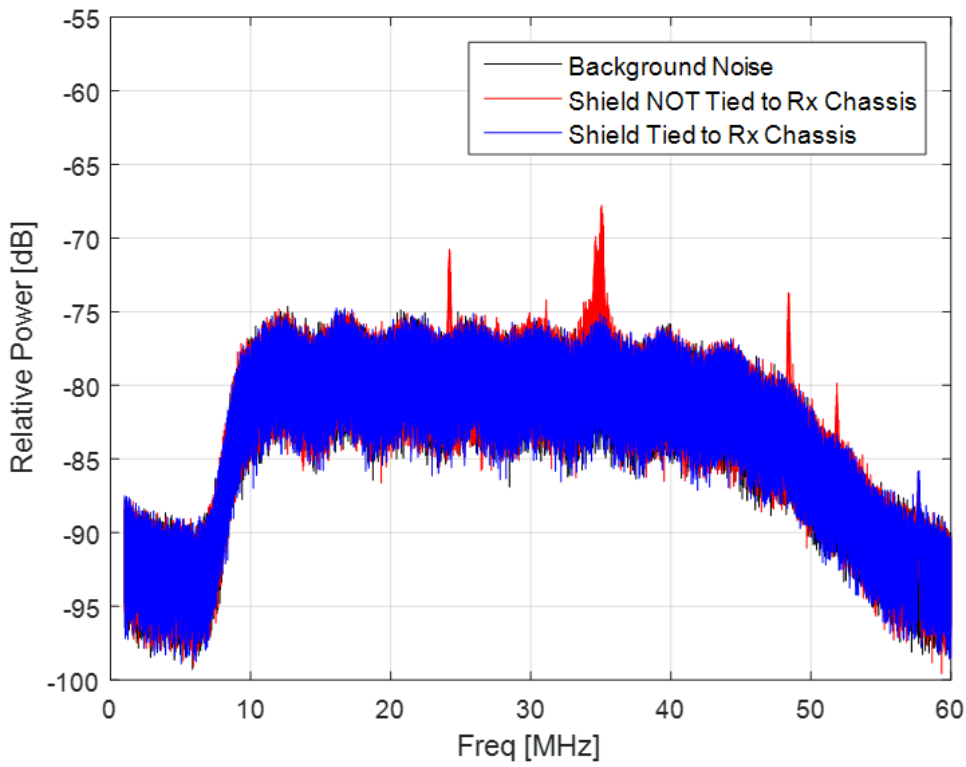

Figure 4-18: Measured RFI for DUT3

Figure 4-18 shows two plots besides background noise. The red is when the power-safe was inside a metallic box but not shorted to the cable shield and the blue represents the configuration in Figure 4-17. It was done in such a manner to demonstrate the effectiveness of proper shielding to the UAS team. The results show that the Faraday's cage approach not only completely suppress the radiated interference but also make the servo system less susceptible to external noise. However, it is important to note that the effectiveness of metallic shielding depends on the skin depth of the shield [22]. Skin depth is a phenomenon in which as the frequency increases, the current over the conductor tends to crowd and eventually confine closer to the outer edge of the conductor.

$$Skin\ Depth = \ \delta = \frac{1}{\sqrt{\pi f \mu \sigma}} \tag{4-1}$$

Where, μ is the permeability and σ is the conductivity of the shield. According to Eq. 4-1 skin depth decreases at a rate of the square root of the frequency. On the other hand conductivity is a function cross-sectional area of the conductor. Which means that if the conductor's thickness $t << \delta$ than the current on the exterior of the shield would completely diffuses through the shield wall. For $t >> \delta$ the frequency of the incident wave would be greatly attenuated.

As for the comparison between the two servos in terms of EM noise reduction in our frequency band of interest, Volz servos are inherently less noisy than HiTec servos because EMI considerations are accounted for in the design. Moreover, standard features such as shielded chassis and integrated shielded connector makes it easy to implement and ensure effective shielding. Additional features are compared in the in Table 4-2.

Features	Volz Servo	HiTec Servo	Units
Stall/Max. Current	4000	4800	mA @ 6 Volts
Max. Torque	284	181	oz./in @ 6 Volts
Operating Voltage	6 - 30	6 - 7.5	Volts
Min. operating Temperature	-60 (-76)	20 (-4)	^{0}C (^{0}F)
Weight	105 (3.70)	70 (2.47)	gram (oz.)
Price	$750	$180	

Table 4-2: Comparison between Volz and HiTec servos

Most aerospace grade power systems use 28 V is standard output voltage; therefore, the wide range of operating voltages of Volz servos eliminates the need for additional hardware such as high power voltage regulators to convert from 28V to 6V. From practicality standpoint the capability to operate at lower temperatures is a much desirable feature when it comes to field operations. The professional grade Volz servos are well documented and product support is easily available which is not the case for our hobby grade HiTec servos. All these advantages come with a price tag of $750, $570 more than Hitec servos, and a weight penalty of 35g (1.3 oz.) for each servo. For all eleven servos the price is $8250 and additional weight is13.6 oz.

Cable shielding plays a crucial role in protection against unintentional radiation and reception of EM interference. It is well understood from this experimental data that proper shield termination significantly affects EM susceptibility.

5 FIELD EXPERIMENT

The first version of the HF sounder was deployed to Antarctica during the 2013 - 2014 field season to verify the functionality of the depth sounder at both frequencies [23]. The success of the Antarctica expedition led to more challenging echo sounding of temperate ice in Greenland. Therefore, the second version of HF sounder radar system with slightly different antenna system and platform was deployed to Kangerlussuaq, Greenland in late winter of 2016 to collect data over Russell Glacier located 25 Kilometers east of town past the tundra highland. Other incremental improvements, such as an upgrade of the onboard GPS system, were also incorporated into the system.

A frozen lake about 3 km west of the glacier was chosen as a runway next to our camp site. An aerial photograph of the campsite and runway is shown in Figure 5-1. Geographic information displayed using Google image in Figure 5-2 gives a spatial sense of the location of the runway and features that were surveyed by HF sounder.

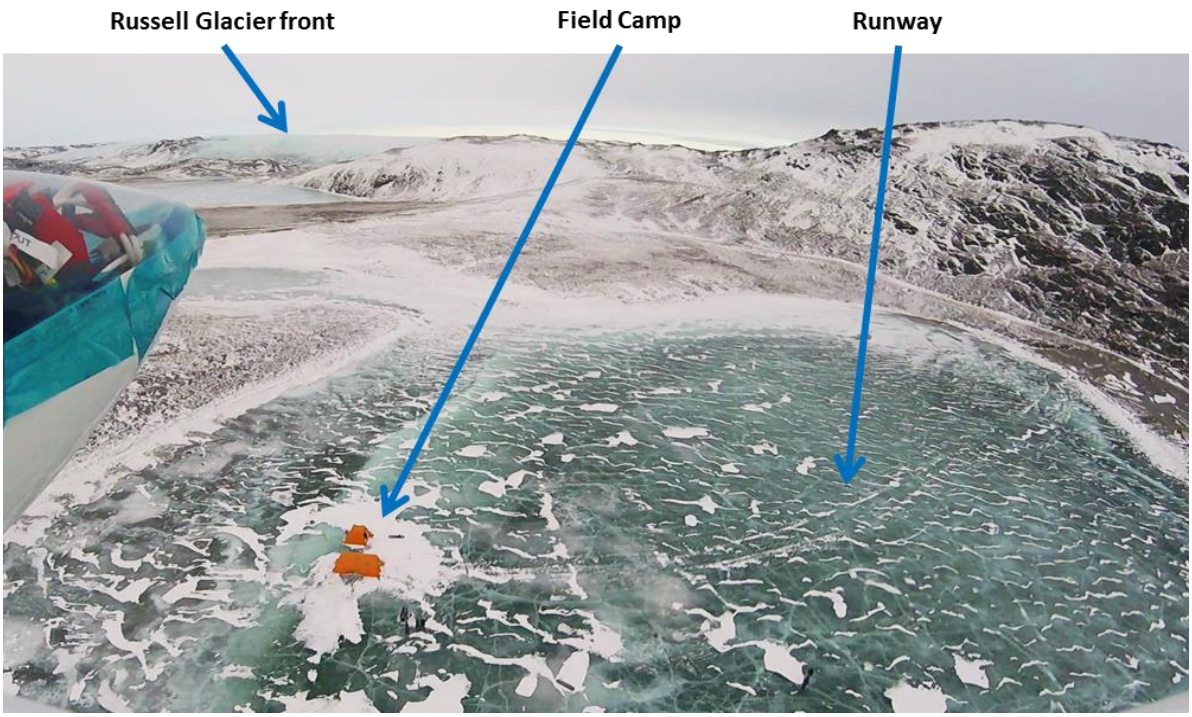

Figure 5-1: Ariel photo of Campsite and Runway

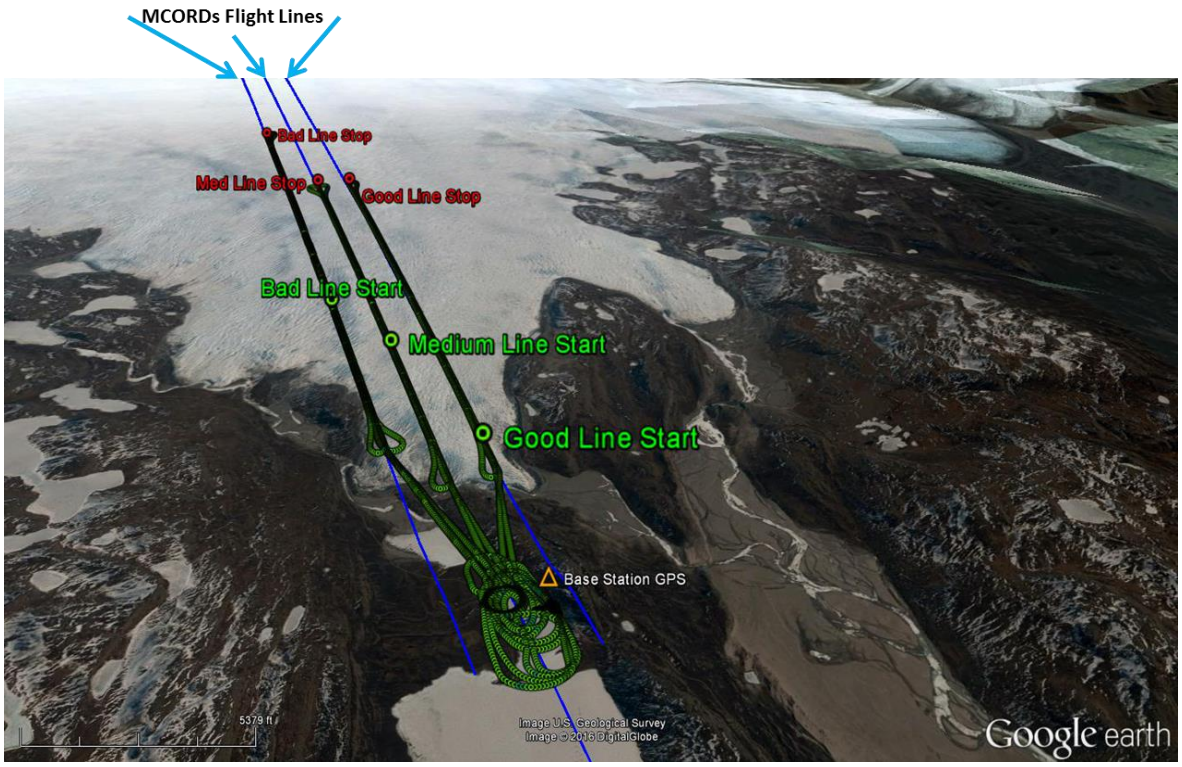

Figure 5-2: Geographic Information of flight lines

The first few weeks of deployment were mainly focused on getting the runway ready followed by flight tests for optimizing the auto pilot system and antenna system characterization. Center frequency and pulse width settings for the radar were adjusted based on in-flight antenna return loss measurements.

The platform was ready to conduct science missions towards the end of deployment. Limited time and additional restrictions imposed by the air traffic control due to inclement weather jeopardized any opportunity to operate the depth sounder at 14 MHz. Therefore the data was collected only at VHF band.

5.1 FLIGHT LINES and SAMPLE RESULTS

A fully integrated UAS equipped with radar was flown over the horizon in full autonomous mode to carry out six science missions over three sets of lines. The lines were characterized as good, medium and bad (based on the data collected by MCORDs) with the good line having the strongest and the bad line having the weakest bed return.

In Figure 5-3(a) the MCORDs data over the good line shows a strong bed return from 2 to 3 and between 4 and 8 along track markers. The effects of the volume scatter is more dominant from 3 to 4 and from 0 to 1. On the other hand the HF sounder data over the same lines in Figure 5-3(b) show a strong return all the way across.

In case of medium lines the return signal is absorbed and the echo is blurry and scattered as noted in MCORDs echogram in Figure 5-4(a). Radiating at 35 MHz significantly lowered the volume scatter due to which areas with en-glacial meltwater (such as range lines between 0 and 1.5 and between 5.5 and 6) were filled by HF sounder as shown in Figure 5-4(b).

High water inclusions in the ice profile attenuated the MCORDs' return signal to a point that it is hard to make sense of much of the structural features of bedrock over bad lines, as shown in Figure 5-5(a). Compared with the echogram from HF sounder's data in Figure 5-5(b), it is easy to see variation in ice thickness from 250 meters to 600 meters from range line 1 to 8. The missing portion of the bed between 0 and 1 could have been filled by radiating at 14 MHz.

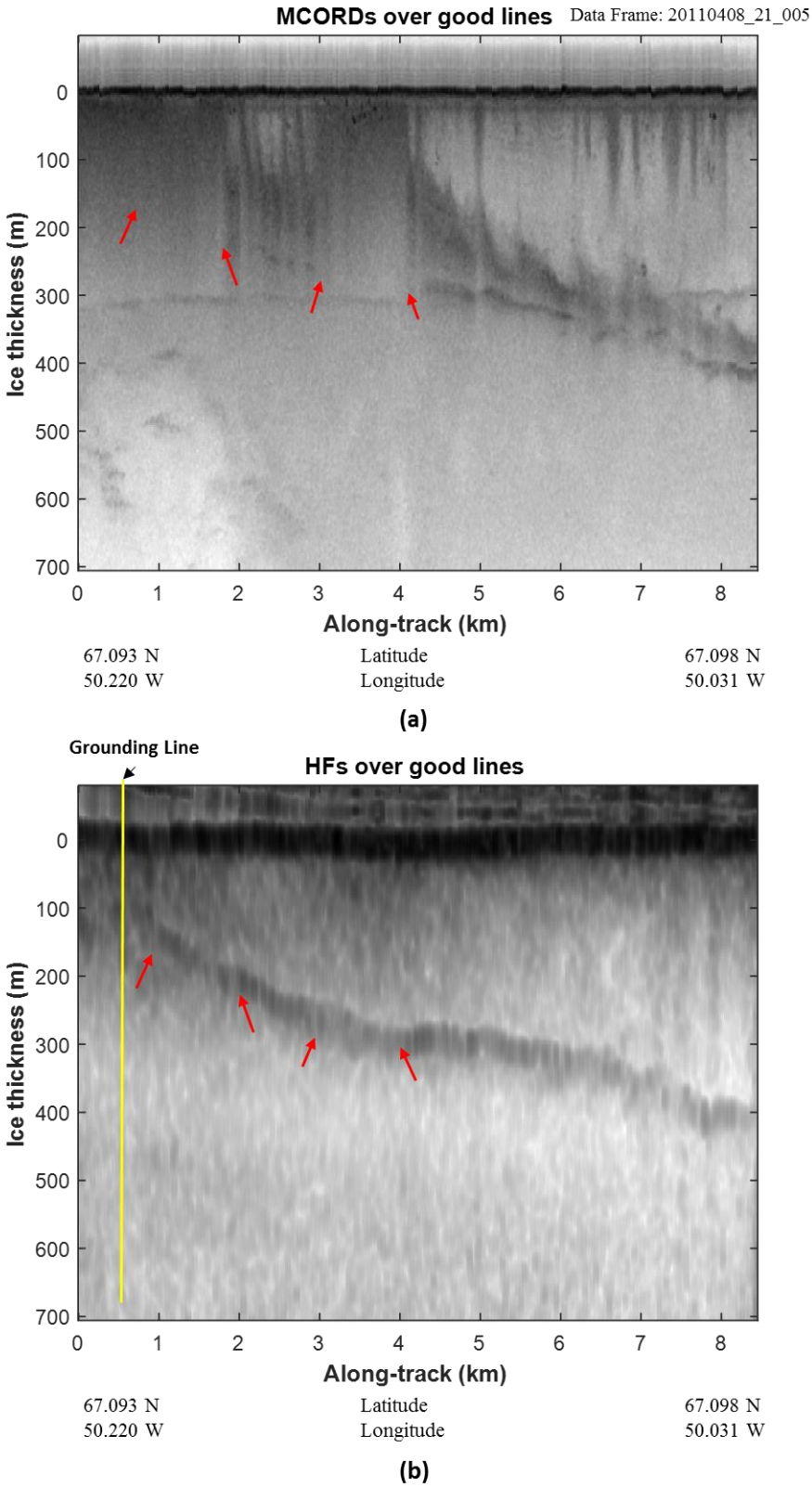

Figure 5-3: Comparison between MCORDs and HF sounder data over "good lines"

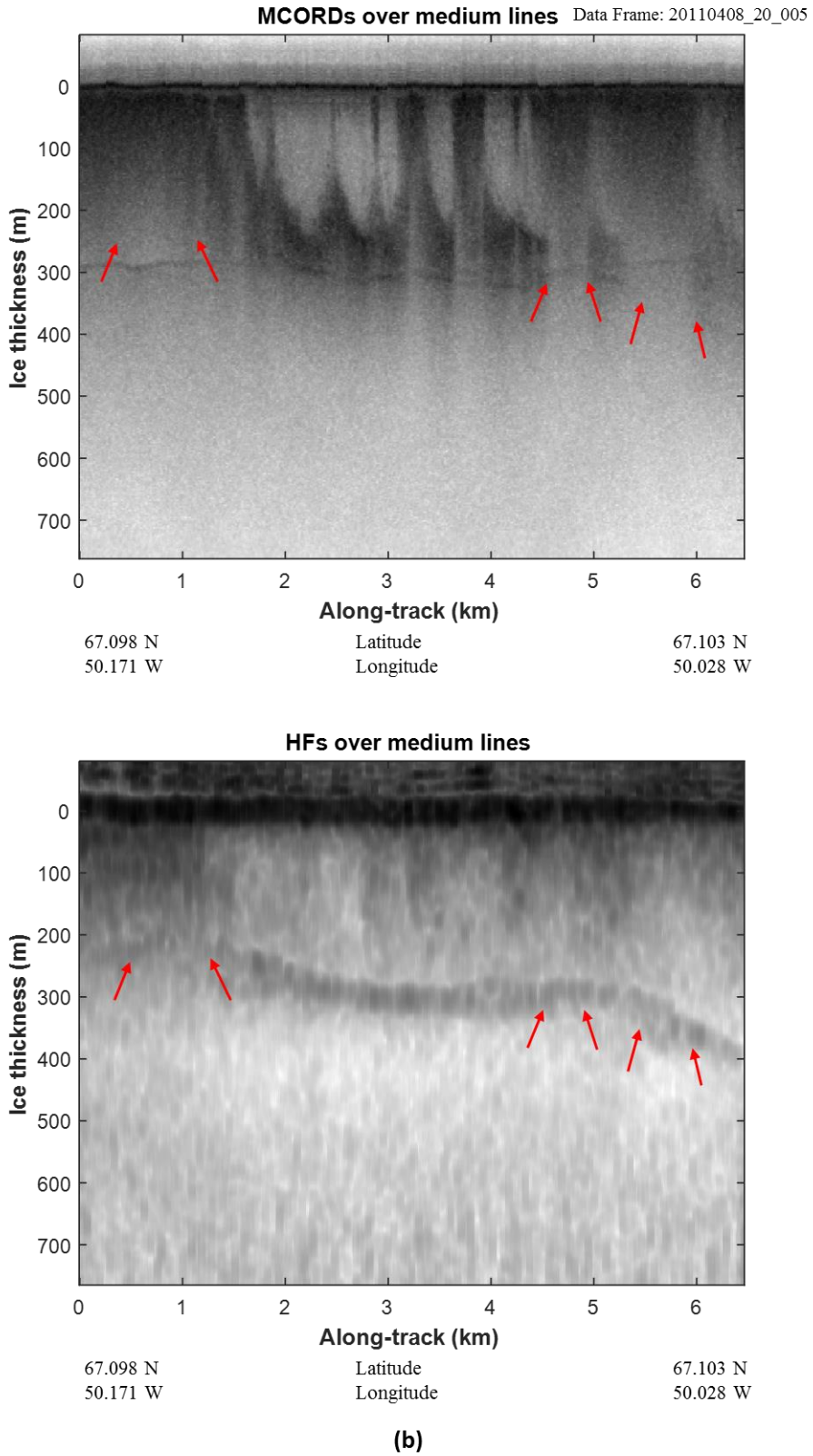

Figure 5-4: Comparison between MCORDs and HF sounder data over "medium lines"

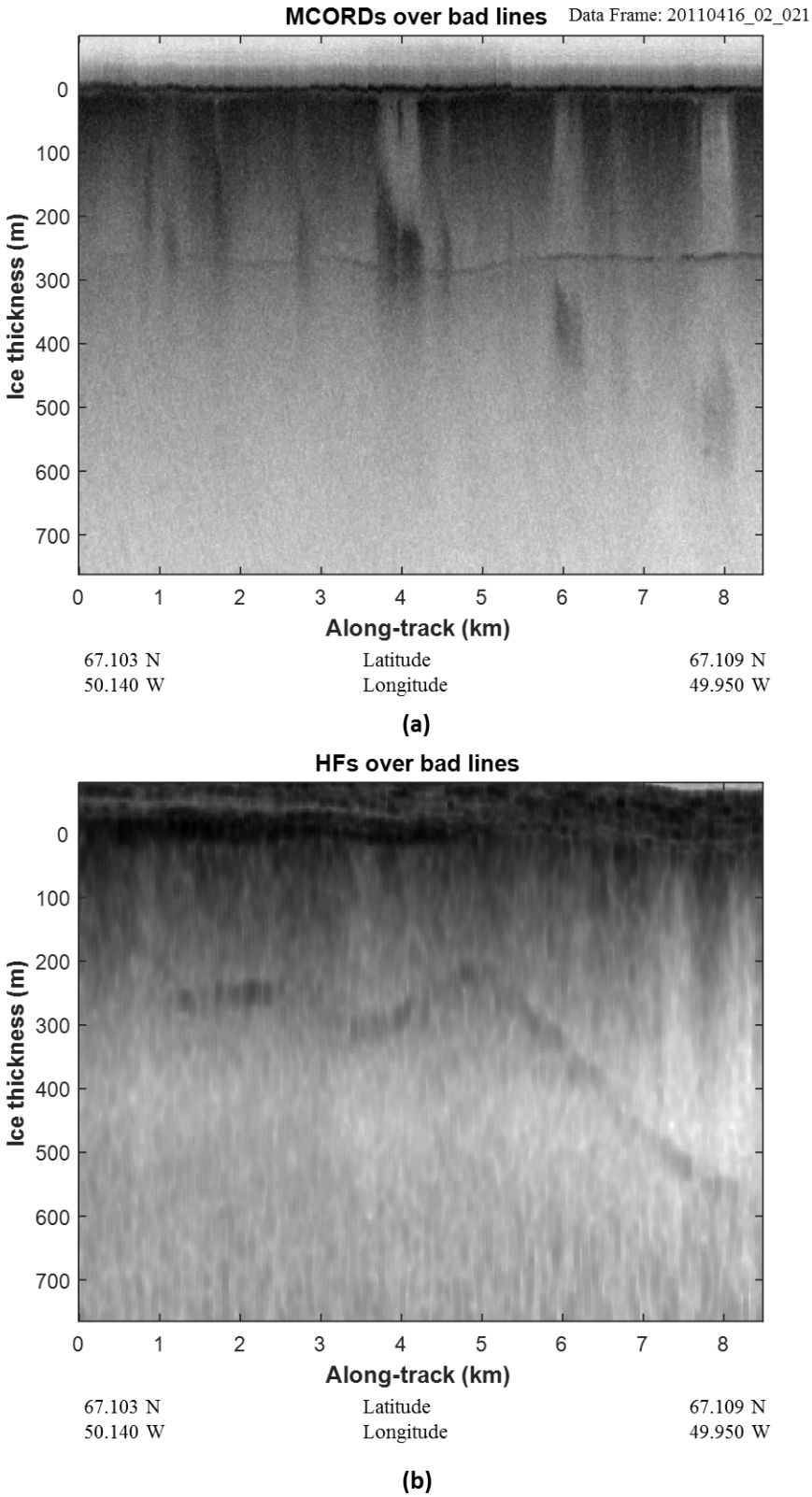

Figure 5-5: Comparison between MCORDs and HF sounder data over "bad lines"

Parameters	MCORDS/I	HF Sounder
Center Frequency	195 MHz	14 MHz and 35 MHz
Bandwidth	30 MHz	0.7 – 1.1 MHz @ 14 MHz 3.3 – 5.5 MHz @ 35 MHz
Peak Transmit Power	1200 W	100 W
Pulse Duration	1 to 30 us	1 us (adjustable)
Pulse Repetition Frequency	<12 kHz	10 - 20 kHz
Vertical Resolution	20 m in ice (NASA DC-8)	99 m @ 14 MHz 34 m @ 35 MHz

Table 5-1: Operating Parameters for MCORDS and HF Sounder [24]

The high transmit power and finer resolution of MCORDs makes it an ideal system for sounding most outlet glaciers in Greenland and Antarctica [24]. However, the greater penetration power and inexpensive deployment cost of HF sounder can complement the capabilities of MCORDs system in sounding key areas with high water inclusions.

6 FUTURE WORK

This work sets the basis for future work in which the high maneuverability of unmanned platforms is coupled with high-performance radar and antennas to achieve two-dimensional spatial sampling. By allowing the radar to fly closely spaced parallel grid lines as proposed by Gogineni et al., it would be possible to control the illuminating beam in both the along-track and cross-track directions through advanced beamforming capabilities and thereby increasing the radar's sensitivity and achieving finer spatial resolution. However, improvements in the current system can be made as described below.

6.1 UAS AUTOPILOT

A more precise autopilot system that can fly parallel lines with $\lambda/4$ spacing at frequency of interest is crucial to achieving a planer two dimensional sampling grid necessary for 2D SAR processing. It will also help in the implementation of a bi-static HF radar system in a UAS swarm, which will essentially constitute a pure hardware based remote sensing solution. It would be a huge step forward in better understanding the basal conditions of ice sheets.

6.2 WEIGHT REDUCTION

UAS endurance is a function of payload, which can be increased by reducing weight. For example, in the case of the radar system, aggressive weight reduction can be achieved by replacing the aluminum chassis with lighter and highly durable carbon composite material. The EM shielding offered by aluminum can be uncompromised, if not enhanced, by wrapping the carbon composite chassis with EM shieling cloth. This approach alone can significantly reduce the overall weight of the radar box as well as provide better shielding solution.

6.3 ELECTROMAGNETIC COMPATIBILITY

EMC issues can be tackled by taking a more proactive approach that involves EMI characterization and mitigation at the sub-system level, as suggested in the EMI test matrix in Table 4-1. Moreover, implementing the clean power supply solution discussed in section 4.2 will help reduce EMI as well as offer power redundancy in conjunction with the batteries.

6.4 MUTUAL COUPLING

The length of the servo wires are a major contributor of mutual coupling due to the location of actuators it is hard to decrease their length. Their length can be made greater than 1λ, but that has its own limitations. Besides adding more weight to the payload, it would be more difficult to route them by cutting through the ribs of the fuselage. A viable solution would be to replace servo wires with fiber optic cables. The effects of mutual coupling would reduce significantly making the self-impedance of the antenna dominate its driving-point impedance, which would make it easier to match its impedance to that of the transmitter over a wider range of frequencies.

6.5 ANTENNA SYSTEM

The capability of the antenna system can be enhanced by resolving to one antenna per platform solution. For instance, more real estate can be made available for the bow-tie antenna by removing the HF antenna. That way, either the length of the antenna or its volume can be increased. A longer dipole would resonate at a lower frequency that would offer greater penetration power. On the other hand greater volume means wider bandwidth. By pushing the radar bandwidth to 7.5 MHz at 35 MHz and operating it in chirped mode, it would correspond to a range resolution of about 20 m in free-space. Similarly, dedicating the entire platform to the HF antenna would expand the possibilities of exploring and implementing more efficient design options.

It is also recommended to use the co-simulation approach to implement the HF antenna's impedance matching network, as it offers high precision and saves time due to the easy transfer of DXF files between design, layout, and fabrication software tools.

Moving forward with this project, the future is to radiate at the lower spectrum of HF band, which would require an entirely different platform with longer wingspan. Finally, in order to dedicate more time to science experiments in the field, all flight tests, antenna characterizations, and integrated system level testing must be conducted in Kansas before deployment.

7 BIBLIOGRAPHY

[1] H.D. Pritchard, R. J. Arthern, D. G. Vaughan and L. A. Edwards, "Extensive dynamic thinning on the margins of the Greenland and Antarctic ice sheets," *Nature*, vol. 461, no. 7266, pp. 971-975, October 2009.

[2] "Understanding Sea-level Rise and Variability," World Climate Research Program Workshop, Paris, 2006.

[3] S. Solomon, D. Qin, M. Manning, Z. Chen, M. Marquis, K. B. Averyt, M. Tignor, and H. L. Miller, *Climate Change 2007: The Physical Science Basis: Contribution of Working Group I to the Fourth Assessment Report of the Intergovernmental Panel on Climate Change (IPCC)*. Cambridge, U.K.: Cambridge Univ. Press, 2007.

[4] A. Shepherd, "A Reconciled Estimate of Ice-Sheet Mass Balance," *Science*, vol. 338, no. 6111, pp. 1183-1189, 30 Nov 2012.

[5] B. M. E. Smith and S. Evans, "Radio Echo Sounding: Absorption and Scattering by Water Inclusion and Ice Lenses," *Journal of Glaciology*, vol. 11, no. 61, pp. 133-146, 1972.

[6] A. Ishimaru, *Wave propagation and scattering in random media*, New York: Wiley-IEEE Press, 1999.

[7] J. Mouginot, E. Rignot, Y. Gim and E. L. Meur, "Low-frequency radar sounding of ice in East Antarctica and southern Greenland," *Annals of Glaciology*, vol. 55, no. 67, pp. 138-146, 2014.

[8] N. Blindow, S. Salat and G. Casassa, "Airborne GPR sounding of deep temperate glaciers — Examples from the Northern Patagonian Icefield," in *14th International Conference on Ground Penetrating Radar (GPR)*, Shanghai, China, 2012.

[9] J. L. Bamber, J. A. Griggs, "A new bed elevation data for Greenland," The Cryosphere, 7 (2), pp. 499-510, 22 March 2013.

[10] W. L. Stutzman and G. A. Thiele, *Antenna Theory and Design*, 2nd Ed. Canada: John Wiley and Sons, Inc., 1998.

[11] C. A. Balanis, *Antenna Theory: Analysis and Design*. Hoboken, NJ: Wiley- Interscience, 2005.

[12] J.J. Carr, *Pracical Antenna Hand Book*, 4th Ed. New York, McGraw Hill.

[13] H. Yagi, "*Beam transmission of ultra short waves*," *Proc. IRE*, vol. 16, pp. 715–741, June 1928.

[14] D. M. Pozar, "Beam Transmission of Ultra Short Waves: An Introduction to the Classic Paper by H. Yagi," Proc. IEEE, Vol. 85, No. 11, pp. 1857–1863, November 1997.

[15] Radio Noise, International Telecommunication Union (ITU-R), P series Radiowave Propagation. 2010

[16] C. Allen, *Radar Measurments II* [PowerPoint Slides]. Retrieved from http://people.eecs.ku.edu/~callen/725/EECS725.htm

[17] Armin W. Doerry, *Anatomy of a SAR Impulse Response*, Sandia National Laboratories, August 2007

[18] M. Skolnik, *Introduction to Radar Systems*, 3rd Ed. New York, NY: McGraw-Hill, Inc., 2001.

[19] D. Rialet, A. Sharaiha, A. Tarot, C. Delaveaud, "Characterization of Antennas on Dielectric and Magnetic Substrates Effective Medium Approximation". In *2009 3rd European Conference on Antennas and Propagation*, pp 3163–3166, March 2009

[20] D. Lamensdorf, “An Experimental Investigation of Dielectric-Coated Antennas.” In *IEEE Transactions On Antennas And Propagation*, vol. ap-15, no. 6, November 1967

[21] Inder Bahl, *Lumped Elements for RF and Microwave Circuits*, 2003 ARTECH HOUSE, INC. Norwood, MA

[22] C. R. Paul, *Introduction to Electromagnetic Compatibility*, 2nd Ed. Hoboken, New Jersey: John Wiley and Sons, Inc., 2006.

[23] Leuschen C., Hale R., Keshmiri S., Yan J.B., Morales F., Mahmood A., Gogineni S., *UAS based Radar Sounding of Polar Ice Sheets*. IEEE Geoscience and Remote Sensing Magazine. pp 8-17, March 2014.

[24] Morales F., Gogineni S., Leuschen C., “Advanced Multi-frequency Radar Instrumentation for Polar Research”, IEEE Transactions on Geoscience and Remote Sensing Vol. 52 No. 5, pp 2824-2842, May, 2014.

8 APPENDIX A: LOOP BACK TEST MATLAB SCRIPT

```
%*************************************************************
%File location :(projects) P:\HF_Sounder\LoopBack\LoopFun35
%MATLAB Script
%Usage: LoopFUNC_34_v1.m
%Description: This script is used to process the Radar data
%from loop back test
%Author: Ali Mahmood
%Email: ali23@ku.edu
%Date: April 15, 2017
%Platform: MATLAB R2015a
%*************************************************************
fs = 50e6;
%% LOOP BACK
[w, tw, nfw, fw, wfft]  = LBack_35(fs);
[w_lpf, w_dd, w_avg, wm] = DownCon_35(w, tw);

%% RETURN:RX from Loop Back
[RXlgw, RXwlgfft]        = RxLB_long_35(w, tw, nfw, fw);

%% Digital Down Conversion and Low Pass Filtering
[rxlg_lpf, rxlg_dd, rxlg_avg, rxm] = DownCon_35(RXlgw, tw);

figure(); plot(tw./1e-6, w); grid on
xlabel('Time [us]'); ylabel('Amplitude'); %title('LoopBack: w');
xlim([0 20]);

%% down conversion and LPF of Rx
rxlg_dB = db(rxlg_lpf);
rxlg_dB = (rxlg_dB)-max(rxlg_dB);

figure();
```

```
plot(tw./1e-6, rxlg_dB); grid on
xlim([5 20])
ylabel('Normalized Power [dB]'); xlabel('time [us]');

figure();
plot(tw./1e-6, rxlg_dB); grid on
ylabel('Normalized Power [dB]'); xlabel('time [us]');
xlim([11.89 12.2]); ylim([-3 0]);

%%%
```

```
win = -hanning(255)/128; win(128)=1+win(128);

wm    = conv2(wave, win, 'same');
w_avg = wm;
w_dd  = bsxfun(@times, w_avg, ffc);
w_lpf = conv2(w_dd, hanning(24)/12.5,'same');

%%%
```